Charged particle therapy, ion range verification, prompt radiation

Mauro Testa

THESE DE L'UNIVERSITE DE LYON

Délivrée par

L'UNIVERSITE CLAUDE BERNARD LYON 1

ECOLE DOCTORALE PHAST

DIPLOME DE DOCTORAT

Présentée à Lyon le 14 octobre 2010

par

Mauro TESTA

Physical measurements for ion range verification in charged particle therapy

Directeur de thèse : M. Chevallier

Jury :	M.	M. Chevallier	Directeur de thèse
	M.	R. Ferrand	
	M.	F. Haas	Rapporteur
	M.	C. Lacasta	
	M.	J-M. Moreau	Président du jury
	Mme	K. Parodi	
	M.	C. Ray	
	M.	D. Schardt	Rapporteur

Acknowledgements

My first acknowledgement goes to the CAS-Phabio group and its outstanding team of people which managed to create a sort of ideal environment where to do a PhD.

I thank the two referees of this thesis, Dr. Florent Haas and Dr. Dieter Schardt for their careful proof reading of my PhD manuscript. I also thank all the members of the jury who have accepted to examine the work presented in this thesis: Prof. Jean-Michel Moreau, Dr. Carlos Lacasta, Dr. Katia Parodi and Mr. Régis Ferrand.

I thank my supervisor, Dr. Michel Chevallier, for his enthusiastic scientific guide and all the precious teachings about radiation detection and measurement along with the constant freedom he gave me in developing my work. I am particularly thankful to Dr. Denis Dauvergne to have accepted and warmly welcomed me in the group. His constant, rigorous scientific support and his kindness in dealing with all human relations were invaluable during these three years. I thank my co-supervisor Dr. Cédric Ray for all the scientific and technical support and his prompt answers to my several questions. Many thanks to Dr. Etienne Testa from whom I learned a lot. All the simulations presented in this thesis along with the major part of the experimental data analysis are based on some of his previous works. I am happy to thank my colleague Fabrice Le Foulher, sharing the office with you during these three years, has always been very pleasant. I thank Pierre Henriquet who always kindly answered my several questions about C++ and physics in general. It was a pleasure to collaborate with Dr. Nicolas Freud and Dr. Jean-Michel Létang. I am particularly thankful for all the scientific discussions and your constant interest and suggestions which helped me to progress in my work. I thank as well Dr. Sonia Karkar for the development of part of the simulation program used in this work.

I acknowledge ETOILE and in particular Prof. Jacques Balosso, Joel Rochat, Prof. Jean-Michel Moreau and Marianne Tierry to have funded my PhD. I am indebted to Prof. Joseph Remillieux. Probably without his interest in diffusing my CV between ETOILE researchers, my PhD would have not been possible.

I finally thank the other students from CAS-Phabio and CNDRI with whom I had enjoyable and fruitful beam-times: Laurie Chollier, Julie Constanzo, Marie-Hélène Richard, Frauke Roellinghoff. At last a kind acknowledgement to all the other members of CAS-Phabio which contribute to create the good and productive atmosphere of the group: Dr. Marcel Bajard, Prof. Michaël Beuve, Dr. Mireille Fallavier and Prof. Jean-Claude Poizat.

Contents

1 Overview

1.1 Particle radiation therapy

The increase of human lifespan is the main cause of the growing incidence of cancer between all the other lethal diseases. According to estimates by the World Health Organization (WHO), the number of new cancer patients, worldwide currently at 10 million, will increase of 50% by the year 2020. Cancer will then be the leading cause of death. Despite extensive research, today only one out of every two patients is successfully cured. Nowadays each year, about 1.1 million new cancer cases are diagnosed in the Europe and about 1.3 million in U.S.

Although surgery remains the most successful cancer cure, approximately 50% of all patients diagnosed with cancer receive curative or palliative radiation treatments, most of the time performed with photon or electron beams (Durante & Loeffler 2009). Nevertheless, in the last decade particle radiation therapy, mainly performed with protons and carbon ions, has gained great interest in the medical community because of its excellent clinical results. The bases of this success are the physical advantages of ions that overcome the limitations of conventional electromagnetic radiation due to their more selective energy deposition in depth, and in the case of carbon beams, also the increased radiobiological effectiveness (RBE) which increases with the penetration depth and reaches its maximum in the distal region of the tumour in correspondence with the Bragg-peak (G. Kraft 2000).

If about 60.000 patients treated with protons since 1957 could lead to consider that proton therapy is nowadays an established technique in regular use at medical centers around the world, on the other hand, C-ion therapy is still at a much more experimental stage. Nevertheless, the interest in carbon ions is not only justified by the good clinical results already obtained on about 5000 patients, but also on the growing attention that this technique is reaching especially in Europe (Amaldi & G. Kraft 2007), Japan (Tsujii et al. 2007) and China (Li et al. 2007). Only in Europe, after a ten year pilot project at Gesellschaft für Schwerionenforschung (GSI) Darmstadt (Germany) in which more than 400 patients have been successfully treated with C-ions (Brower 2009), the first dual proton and carbon facility entered in clinical operation in November 2009 at the Heavy Ion Therapy Center (HIT) in Heidelberg (Germany). Three new facilities are in advanced phase of construction in Marburg (Germany), Kiel (Germany) and Pavia (Italy) while some others are planned in Austria and Sweden. In France, the first national hadrontherapy centre ETOILE, is currently enrolled on the last phase of the call for bids and is foreseen to start the operation in 2015.

Although heavy-ion therapy has reached a high degree of perfection in clinical use there is still large possible progress to improve this novel technique (G. Kraft & S. D. Kraft 2009). Besides basic biological studies to extend particle therapy to more tumor entities and to assess whether the neighboring ions to

carbon could also have a clinical application, on the technical side, many improvements of the equipment seem to be possible. Two major topics are the extension of particle therapy to moving organs and the transition to more compact and therefore cheaper particle accelerators. Finally, what also makes the object of this thesis, to fully take benefit from the favorable ion depth-dose profiles a precise estimation of the ion range is required to accurately determine the position of the dose peak. Therefore the setting up of future techniques allowing *real-time* control of the dose distribution is highly desirable and several diversified R&D programs which include a variety of systems like collimated prompt-gamma camera, Compton camera and Interaction Vertex Imaging are currently being undertaken by our group (Dauvergne et al. 2009).

1.2 Prompt γ-camera for dose verification and ion range monitoring in particle therapy

As already mentioned, the higher physical selectivity of C-ion therapy requires higher precision in the monitoring of the applied treatment, especially in delicate clinical situations (Parodi 2004). Positron emission tomography (PET) is currently the only clinical method for *in vivo* and *in situ* monitoring in charged particle therapy (Enghardt et al. 1992). During the irradiation, positron emitters like ^{15}O and ^{11}C are formed in nuclear reactions between ions and tissues. The detection of this transient radioactivity via PET and the successive comparison with Monte Carlo simulations based on the prescribed beam application is used as a non invasive validation method of the whole treatment planning and delivery chain (Parodi et al. 2008).

Nevertheless PET monitoring systems provide essentially *a posteriori* verifications of the delivered treatment plan since the time required to acquire enough counting statistics and the time for image reconstruction compel the PET images to be obtained only after each irradiation fraction.

Therefore the main and ultimate objective of the prompt photon detection technique for ion range monitoring which is presented in this thesis, is to provide a *real-time* verification of the correctness of the treatment plan in the meanwhile of the irradiation itself. This would hence allow interrupting the irradiation in case a mismatch between the planned and actual ion range or integral dose occurs. The *real-time* feature of our technique is conferred by the fact that within much less than a nano-second following the ion beam impact on the target, photons and neutrons are emitted by excited nuclei formed each time a nuclear fragmentation process occurs. With PET, on the other hand, due to the very low induced activity and to the radioisotopes half-lives, which are much longer than the characteristic time (of the order of a second) in which an iso-energy slice of tumour is treated, any *real-time* monitoring would be very unlikely to be done.

A first experiment demonstrated that the measurement of prompt γ-rays could be directly correlated with the proton range (Min et al. 2006) with an accuracy of 1-2 mm. The extension of the work by Min et al to C-ion beams was firstly performed by our group at the GANIL facility (Caen, France) in 2007 with 73

MeV/u $^{13}C^{6+}$ ions impinging on a PMMA target. The correlation between prompt photons and the Bragg-peak was obtained even for C-ions in which both target atoms and primary ions undergo nuclear fragmentation (E. Testa et al. 2008). As in the case of PET systems, it is assumed that the nuclear fragmentation of both primary beam and target nuclei is correlated with the particle range. Indeed fragmentation occurs almost all along the ion path till 2-3 mm before the Bragg-peak where nuclear reaction cross sections start dropping when the available energy in the projectile-target nuclei center of mass approaches the Coulomb barrier. This implies that, in principle, the measurement of the emitted prompt photons, raised from primary and secondary ion nuclear interaction, could bring valuable information both on the dose distribution and on the Bragg-peak position.

Moreover, the discrimination between prompt photons and background radiation made with time of flight (TOF) measurements represents the main characteristic of our experimental set-up and it avoids the use of bulky neutron shielding like in the case of the work presented by Min et al. This feature is of particular importance since it permits to significantly reduce the size of the shielding material (E. Testa et al. 2009) allowing a stacked multi-detector set-up that, in principle, can be employed clinically for *real-time in-situ* ion range monitoring.

This thesis reports on two new series of experiments which have been performed at the GANIL and GSI facilities with 95 MeV/u and 305 MeV/u $^{12}C^{6+}$ ion beams stopped in PMMA and water phantoms. A major issue of these measurements is the discrimination between the prompt photon signal (which is correlated with the ion path) and a vast neutron background uncorrelated with the Bragg-Peak position. Two techniques are employed to allow for this photon-neutron discrimination: the time-of-flight (TOF) measurement and the pulse-shape-discrimination (PSD). Both techniques are discussed and described in detail with particular considerations on the beam time-structures of cyclotrons and synchrotron accelerators (TOF) and the interaction mechanisms along with the detector characteristics for the assessment of the PSD performances. Additionally, an extensive study has been performed to investigate whether a prompt neutron component may be correlated with the carbon ion range. Finally, some preliminary results from a recent multi-detector and multi-collimator experiment performed at GANIL with 75 MeV/u $^{13}C^{6+}$ are also briefly described.

In the last part of the thesis is presented a simulation study performed with Geant4 Monte Carlo code to assess the influence of the main design parameters on the efficiency and spatial resolution achievable with a multi-detector and multi-collimated Prompt Gamma Camera. Several geometrical configurations for both collimators and stack of detectors have been systematically studied and the considerations on the main design constraints are analyzed.

1.3 Outline of the thesis

The thesis is organized as follows. The second chapter gives a general introduction on particle radiation therapy with some special emphasis on the physical and biological rationale for the use of ions compared to conventional electromagnetic radiation along with a brief discussion on the costs of both techniques. A review of the state of the art systems for external radiation therapy is also presented and the former and current particle therapy centers are described together with an analysis of some clinical results. In the third chapter are reviewed the main physics phenomena of the interaction of photons, neutrons and ions with matter which are at the base both of particle therapy and the prompt photon monitoring technique we are developing. Chapter four summarizes the current and proposed methods for dose and ion-range verification in particle therapy. The literature results from PET are listed and the new techniques based on prompt radiation detection (collimated prompt γ-camera, Compton camera and Interaction Vertex Imaging) are presented. Chapter five shows the experiments on the physical measurements of the prompt radiation originated from C-ion fragmentation that we performed at GANIL and GSI facility together with the detector tests performed in our laboratory. The principles of the collimated prompt gamma camera are described and analyzed in details and some considerations are provided about the future clinical applicability of our technique. In chapter six a preliminary Geant4 Monte Carlo simulation study is performed in order to assess the influence of the main design parameters on the efficiency and spatial resolution achievable with a multi-detector and multi-collimated Prompt Gamma Camera. The general conclusions and outlook are presented in the summary.

2 Radiation therapy: introduction

Radiation therapy plays a major role in cancer treatment. Approximately 50% of all patients diagnosed with cancer receive curative or palliative radiation treatments, sometimes in combination with surgery which remains the most successful cancer cure. The high majority of patients undergo conventional radiation therapy which is performed with photon or electron beams. The potential of treating cancers with X-rays was recognized soon after their discovery in 1895 by Roentgen and since then, the application of ionising radiation in oncology has constantly grown, becoming a routine tool in present hospitals. The final aim of all kinds of radiotherapy is to deliver the prescribed dose to the tumour sparing as much as possible the surrounding healthy tissues. Indeed, at least in principle, any tumour can be controlled if a tumouricidal dose is applied, but the tolerance of the healthy tissues limits the maximum dose that can be used. Over the last fifty years great enhancements in the conformity of the dose to the tumour-volume has been achieved through several technological improvements. The replacement of low energy X-rays tubes (energy < 250 keV) with high-energy γ-rays (up to 20 MeV) produced by modern electron linear accelerators partially overcame the limitations of the exponential decreasing depth dose distribution of photons and allowed to treat deep-seated tumours. Moreover, new irradiation techniques like in Intensity Modulated Radiation Therapy (IMRT) still increased the dose conformity by delivering spatially non-uniform photons beams from different irradiation portals (Webb 2003).

Some attempts of using ionising radiation different from X-rays have also been done. In the 1970s negative pi mesons (pions) have been proposed for radiotherapy due to their high-LET component in the tumour region and the so called "star formation" at the end of their path (Kligerman et al. 1979). Indeed, since pions are negatively charged, when stopped they are absorbed by the positively charged nuclei of oxygen, nitrogen and carbon which become unstable. This leads to their disintegration producing neutrons, and charged particles from protons to heavy ions increasing the total dose in the pions stopping region. Nevertheless worldwide trials with pions were stopped altogether after the treatment of approximately 1100 patients due to the lack of the expected clinical requirements (G. Kraft 2000).

Fast neutrons (energy from 20 to 70 MeV) have the same exponential absorption as X-rays but a greater LET which makes them radiobiologically interesting for treating radioresistant tumours. Although high energy **neutrons** do not represent anymore a state of the art radiotherapy technique, they are still clinically employed for cancer treatment (Maughan & Burmeister 2007) while therapy with low energy neutrons has now mostly phased out (G. Kraft 2000).

In Boron Neutron Capture Therapy (BNCT) thermal or low energy neutrons (energy from 0.025 to 1 eV) are employed to irradiate solid-tumours which are uploaded with boron-rich compounds. This technique exploits the nuclear

reaction of ^{10}B absorbing the neutron and producing ^{10}He and ^{7}Li nuclei which constitute very high-LET radiation potentially lethal to any cells in which the reaction occurs (Barth et al. 1990). Several BNCT trials have been performed worldwide (Beddoe 1997) and although not all of them have been completely successful, some laboratories in the world are still carrying out research in this domain (I. Kato et al. 2004). Nevertheless, the most critical parameter still limiting BNCT is the boron uptake in the tumour that crucially affects the ratio between dose to cancer cells and healthy tissues.

2.1 Physical rationale for particle radiation therapy

In order to overcome the physical limitation of conventional radiation therapy, the use of charged particle like protons or heavier ions (from ^{4}He to ^{16}O) was proposed due to their more selective dose deposition as sketched in figure 2-1. Indeed by contrast with X-rays or γ-rays, which show an exponential decrease of the absorbed dose with increasing tissue depth, charged particles deposit little energy at the body's surface where their velocity is high -and therefore their LET is low- and instead they deposit a maximum of energy just before coming at rest in a region commonly called the Bragg-peak (Bragg & Kleeman 1905).

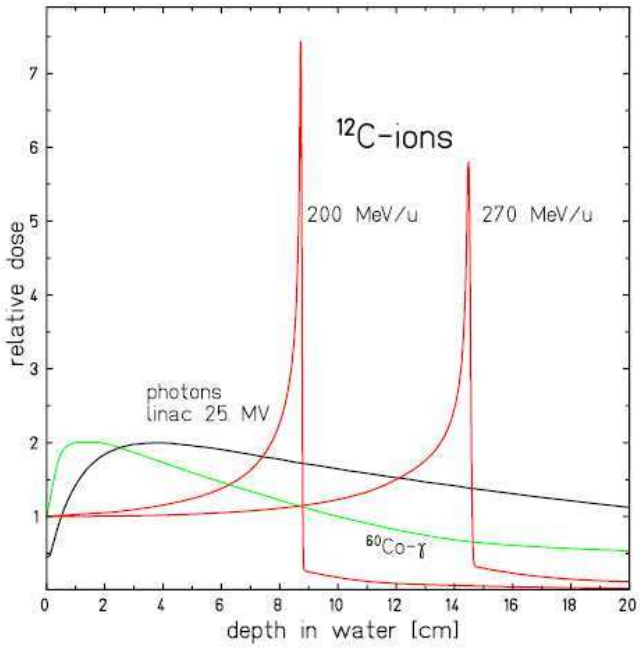

figure 2-1: Comparison of depth-dose profiles for carbon ions and photons from (Schardt et al. 2010). The inverse depth dose profile of carbon ions compared to photons is favorable to treat deep-seated tumours.

Since the Bragg-peak for a particle of a given energy is too narrow to cover the entire tumour volume, several Bragg-peak curves from particle of different energies, have to be superimposed to create a so called Spread-Out Bragg-Peak (SOBP) as sketched in figure 2-2. The number of particles for each voxel of the SOBP and therefore the relative weight for each individual Bragg-peak curve, provides the absorbed physical dose and it is calculated by the Treatment Planning Systems (TPS) (M. Krämer et al. 2000).

There are typically two ways of producing a SOBP: a beam of particles with a fixed energy is attenuated through fast insertion of absorbers with different thicknesses that produce Bragg curves which peak at defined tumor depths (passive modulation), or alternatively, the energy of the particle beam is directly adjusted in the accelerator, ideally without any material in the beam path (active modulation). Indeed, the insertion of range shifters into the beam as typically used in passive systems has the main drawback of reducing the beam quality and producing secondary neutrons.

Even for the lateral scanning of the tumor volume two techniques are usually employed. In passive beam shaping, the initial narrow beam provided by the accelerator, is first broadened in a scattering device and then collimated to the largest target contour as seen in beam's eye view. In active spot scanning systems a pencil beam is moved in the horizontal and vertical directions by fast magnetic scanning units (Haberer et al. 1993). Several other solutions in between full "active" and full "passive" ion delivery systems are discussed for instance in (W. T. Chu et al. 1993). It is nevertheless commonly assumed that active spot scanning provides more conformal and homogeneous dose profiles than passive beam modulation (Kooy et al. 2010). Indeed, with pure passive systems, a significant volume outside the target volume is covered with the same dose as the tumor. This effect can be partially mitigated introducing an additional compensator that takes into account the geometrical profile of the distal edge of tumor along with the complex tissue composition (Schardt et al. 2010). Additionally, by means of dynamic collimators a better shaping of the proximal part of the target volume can be achieved. However, also with these sophisticated techniques, the strictly-tumor conform treatment using passive beam shaping is not feasible (G. Kraft 2000). On the other hand, one of the main problems using active beam delivery systems is the treatment of moving organs in which classic motion compensation techniques such as multiple painting (rescanning) or gating, cause field inhomogeneities and can substantially increase the scan time (Bert et al. 2008). A more promising approach is target motion tracking in which lateral motions are directly compensated with the beam scanning system and degraders are used for range corrections (Rietzel & Bert 2010). Nevertheless, the problem of detection of the inner motion of the organs around the tumor and of the target volume itself remains to be solved.

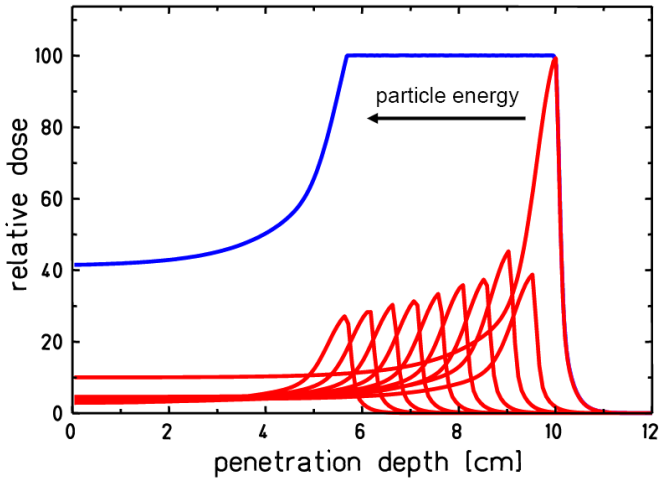

figure 2-2: Superposition of several C-ions Bragg-curves with different energies (red lines) to produce a Spread-Off-Bragg-Peak SOBP (blue line) from (www.gsi.de/forschung/bio/).

2.2 Radiobiological rationale for particle radiation therapy

The main advantage of heavier ions over protons and photons is their radiobiological effects on tissues. The Relative Biological Effectiveness (RBE) is defined in equation 2-1 as the ratio of X-ray and ion dose producing the same biological effect.

$$RBE = \left.\frac{D_{X-rays}}{D_{ion}}\right|_{isoeffect} \qquad \textbf{2-1}$$

Carbon ions used in particle therapy have an RBE of about 1 in the entrance channel and as high as 3-4 in the Bragg-peak region as it can be seen in the bottom part of figure 2-3. The RBE depends on several parameters. First, RBE depends on dose level: it is usually higher for lower doses and lower for larger doses giving rise to the typical shoulder shape of the cell photon response curves (K. Weyrather 1999). Second, it depends on the energy or LET of the penetrating particle: RBE increases with LET up to an ion-dependent maximum value and then decreases for still higher LET (Furusawa et al. 2000). Third the RBE depends on the particle type, for heavier particle the maximum RBE is typically shifted to higher LETs (Weyrather & G. Kraft 2004). Last, RBE depends on the radiosensitivity of the irradiated cell line, the higher the radiosensitivity the lower the RBE (K. Weyrather 1999).

To take into account all RBE dependencies a biophysical model has to be implemented. This represents the main difference between therapy with heavy-ions and protons since protons are commonly considered having a fixed RBE=1.1 (Paganetti et al. 2002) and therefore a mere physical dose optimization is adequate. By contrast, with heavy-ions, the RBE is the most important quantity in biological treatment planning since it determines the photon-equivalent dose by multiplication of the absorbed physical dose as represented in the upper part of figure 2-3. RBE estimations represent as well the source of higher uncertainty of the whole hadrontherapy treatment (Elsässer et al. 2008). Several biophysical models have been proposed for ion beam therapy (Scholz &

Elsässer 2007) although only three have been clinically implemented in the ion therapy centers which have treated patients up to present. At the Lawrence Berkeley Laboratory (LBL) Berkeley (USA) a rather simple linear quadratic model (Dale 1986) was used. It is based on numerous cell survivals measurements for different particles and LET (Blakely et al. 1979) and knowledge about the composition of the particle field. At the Heavy Ion Medical Accelerator in (HIMAC) Chiba (Japan) the actual biophysical model is based on measurements of human salivary gland cell lines and their survival to C-ion is inferred from prior experience with fast neutrons of equivalent effectiveness (Kanai et al. 1999). At the Gesellschaft für Schwerionenforschung (GSI) Darmstadt (Germany) a so called Local Effect Model based on track structure calculations and cell response to X-rays was applied to calculate complex 3D volumes homogeneous photon-equivalent dose (Scholz & G. Kraft 1994). Research in the field of biophysical models is pretty active and recently the effects of cluster effects on DNA single and double strand breaks has been investigated (Elsässer & Scholz 2007) while other authors proposed to include the stochastic nature of ionizing radiation into the models to get better consistency with the observed statistical properties of dose deposition (Beuve et al. 2009).

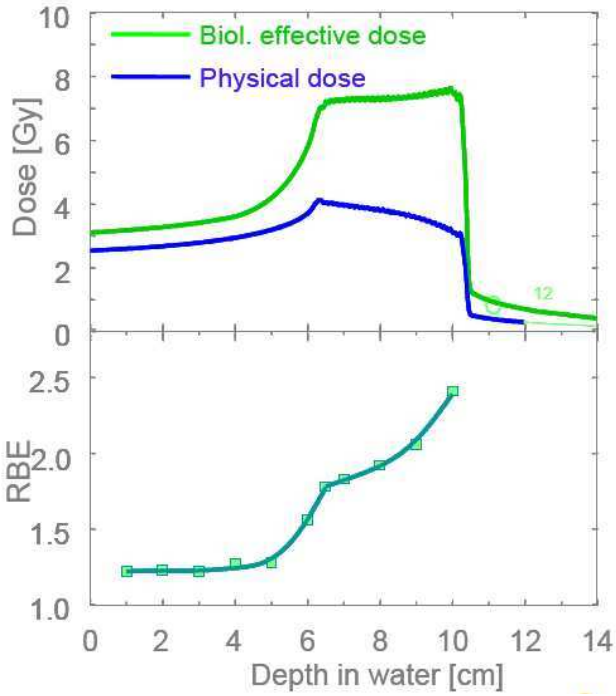

figure 2-3: Up: homogenous biological effective dose distribution (green line) and inhomogeneous physical dose distribution (blue line) obtain by superposition of different C-ion Bragg-peak curves. Down: C-ion RBE as function of the penetration depth in water. The flat biological effective dose distribution is obtained by multiplying the physical dose by the RBE; from (www.gsi.de/forschung/bio/).

Independently from the biophysical model that is adopted, the biological dose has to be calculated by a TPS ideally not only in the target but also in the entire irradiated volume (M. Krämer & Scholz 2000). This is a non trivial task especially when multiple irradiation fields are applied since the RBE

dependencies are complex and therefore the physical dose distribution may result to be quite inhomogeneous in order to provide a homogenous biological dose in all the tumour volume and sparing as much as possible the critical organs (see the upper part of figure 2-3).

2.3 Particle vs conventional radiation therapy: clinical results and cost analysis

An ideal radiotherapy treatment would deliver 100 % of the dose to the tumour volume to kill all the cancer cells while zero dose would be given to the surrounding normal tissues. This is in practical not achievable due to the unavoidable dose deposited in the entrance channels of the irradiation ports. Nevertheless in the last fifty years a lot of progress has been done to better conform the dose to the target while sparing as much as possible the neighboring critical structures.

The basic idea to better spare the tumour surrounding healthy tissues is to multiply the number of beam directions from where the irradiation is delivered. In this way the dose in the entrance channels is diluted over larger volumes while the contribution of each irradiation field sums up in the target. Current state of the art Intensity-Modulated Radiation Therapy (IMRT) can sculpt high-dose volume around the site of disease with millimetric precision, and this technique has become the dominant approach in the majority of oncology wards using conventional radiation (Webb 2003). In modern IMRT not only the geometrical shape of each irradiation field is spatially modulated via multi-leaf collimators (MLC) but even the radiation fluence is varied for each beam direction. In commercial systems like Tomotherapy a very high (>50) number of beams are used and a linear accelerator is directly attached to a conventional C-arm gantry rotating 360° around the patient (Mackie et al. 1999). More recently, another rotational IMRT approach, 'Single-arc' has been developed (Wang et al. 2008) and has found a lot of interest as a commercial product (RapidArc, VMAT). In the Single-arc approach there is no intensity modulation for any one beam angle, but the radiation field shape is varied dynamically and rapidly by MLC as the gantry rotates around the patients. Therefore in the rotational approaches the selection of beam angles is not anymore a problem, but the distribution of dose over large healthy tissues has been a concern (Bortfeld & Webb 2009). Intuitively one would expect that using more beams will always help to shape radiation dose distribution to match the tumour volume, even though it is clear that there is a point of diminishing return. Indeed, a recent theoretical investigation showed that, in realistic cases, nothing will be gained by using more than 10-20 beams (Bortfeld 2009). Another commercial product which in the last decade obtained a considerable success, and is now installed in more than 150 hospitals is called Cyberknife (Adler Jr et al. 1997). The two main technological elements of the Cyberknife system are represented by i) the LINAC accelerator mounted on a robotic arm that allows more degrees of freedom than an isocentric gantry in choosing the direction of the incoming beam, and ii) a real-time image verification before each beam irradiation which

eliminated the need to use skeletal fixation for either positioning or rigidly immobilizing the target.

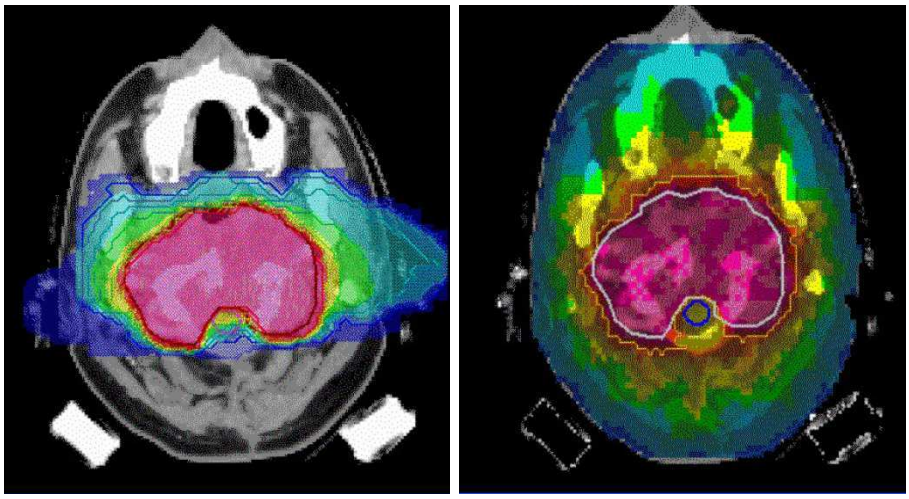

figure 2-4: Comparison of treatment plans for large tumour volumes in the base of the skull. Left: plan for carbon ions, two fields of irradiation. Right: plan for IMRT nine fields of irradiation. The irradiation with C-ions results in a substantial reduction of the integral dose to normal tissue and better spare of critical structures. Picture from (Durante & Loeffler 2009).

Which is the most tumour-conformal therapy between photon and particles is still an open question although both modalities have shown very high accuracy. In figure 2-4 it is presented the comparison between two treatment plans for a large tumour of the skull for C-ions and IMRT. It can be noticed that only two irradiation fields for C-ions produce the same dose homogeneity in the target as nine IMRT irradiation fields due to the superior inverted depth dose profile of ions compared to photons as already shown in figure 2-1. It is also clear that, at least in this example, the use of carbon ions results in a substantial reduction in the integral dose to the normal tissues and the sparing of critical structures (Durante & Loeffler 2009). Moreover, for a fair comparison of the conformality between photons and ions, the technically available beam direction must be the same. If this is partly true for protons, since a high number of proton facilities are equipped with gantries, it is not the case for C-ions since, so far, all the treatments have been performed with fixed beams. The world-first heavy-ion gantry, although already built, is not yet operational at the Heidelberg Ion Therapy Center (Fuchs et al. 2008).

2.3.1 Clinical results

As already mentioned, more than 60000 patients have been treated with protons whose main rationale had been the poor local disease control with conventional radiotherapy and the proximity of critical dose-limiting normal tissue. Protons are a particular treatment option for pediatric tumours, where an elevated risk of radiation-induced normal-tissue complications is expected, owing to the increased inherent tissue sensitivity of very young patients (Durante & Loeffler 2009). Moreover the reduction of the integral dose to normal tissue can confer a significant lower risk of developing second cancer after receiving proton irradiation compared to convention photon therapy (Newhauser et al. 2009).

Most of the patients treated with C-ions so far (approximately 5400) have been included in prospective clinical phase I-II trials. One of the main rationales for choosing C-ions is the high radioresistance, and sometimes low oxygenation of some types of tumours which are very unresponsive to conventional radiation, and in some cases even to proton therapy. Table 2-1 shows a comparison of clinical results for conventional radiation therapy with photons and C-ion treatments performed at NIRS and GSI.

Indication	End point	Results Photons	Results Ions NIRS	Results Ions GSI
Nasopharynx carcinoma (advanced state)	5 year survival	40 - 50 %	63 %	
Chordoma	Local control rate	30 - 50 %	65 %	70 %
Chondrosarcoma	Local control rate	33 %	88 %	89 %
Glioblastoma	Average survival time	12 month	16 month	
Choroid melanoma	5 year survival	95 %	96 % preservation of eyesight	
Paranasal sinuses Tumours	Local control rate	21 %	63 %	
Pancreatic carcinoma	Average survival time	6.5 month	7.8 month	
Liver tumours	5 year survival	23 %	100 %	
Salivary gland tumours	Local control rate	24 - 28 %	61 %	77.5 %
Soft-tissue carcinoma	5 year survival	31 - 75 %	52 - 83 %	

Table 2-1 Comparison of clinical results for conventional radiation therapy with photons and C-ion treatments performed at NIRS and GSI. C-ions are superior to photons for all the end points under consideration; from (www.gsi.de/forschung/bio/).

The NIRS data indicate that C-ions are particularly effective against tumours of the head and neck, skull base, lung, liver, prostate, bone, soft tissues and pelvic metastases of rectal cancer especially for histological types against which conventional radiation has reduced efficacy (Tsujii et al. 2007). The results of clinical trials at GSI have shown that C-ion therapy is very effective for low-grade and intermediate-grade chondrosarcomas, skull base chordomas and adenocystic carcinomas (Schulz-Ertner & Tsujii 2007). Recently the French Haute Autorité de la Santé recognized the relevance of carbon ion therapy to cure cancers. However, the indications by the HAS are less optimistic about the advantages of carbon therapy against proton and photon therapy than those given in table 1, except for adenoid carcinoma were a clear benefit in using C-ions was identified.

More generally we can conclude that, although scarce data are available comparing proton and C-ions with modern stereotactic radiation therapy, particle therapy is superior to IMRT for the most favorable tumour types, in particular ocular melanoma, adenoid carcinoma, and chondrosarcomas of the base of the skull (Durante & Loeffler 2009). Nevertheless, the promising results obtained especially with C-ions need confirmation with larger number of patients, and they should possibly be compared, in randomized clinical trials, with photon IMRT and proton therapy although this may cause ethical issues due to the allocation to patients of potential suboptimal conformal radiation delivery.

2.3.2 Cost analysis

The debate on the cost-benefit ratio of particle therapy is still ongoing. No ultimate answer is given on whether the high costs of accelerator and beam delivery techniques are justified by a clear clinical advantage (Durante & Loeffler 2009). The current literature of cost effectiveness of particle therapy is scarce, non-comparable and largely not performed according to standard health technology assessment criteria (Pijls-Johannesma et al. 2008). Besides, the current use of different models for cost evaluation makes difficult to compare and to determine the relative impact in terms of cost for this new treatment modality. In figure 2-5 comparative average costs for different cancer treatments are shown. We may observe that proton and carbon ion therapy are slightly more expensive than the average cost of cancer treatment in France but nevertheless cheaper than regularly employed chemotherapy treatments. Similar results have been obtained for a dedicated study on the cost-effectiveness of carbon ion therapy for skull base chordoma (Jäkel et al. 2007). In this particular case the conclusion was that carbon ion therapy, although more expensive, is at-least as cost effective as advanced photon therapy. However, C-ions offered substantial benefits for patients, such as improved control rate and less severe side effects. It is nevertheless not possible to generalize this conclusion to all tumour types since the evidence on the cost effectiveness of particle therapy is still scarce and therefore adequate reimbursement is necessary to support such innovative but yet costly technique (Pijls-Johannesma et al. 2008). It is in any case foreseen that the still high costs of a current particle therapy center (approximately 100 millions euro) will decrease in the future mainly as a result of the interest of large commercial companies. Moreover, these costs have to be weighted against the global expenses for cancer therapy that, only in France, correspond to 11 billions euro per year (330.000 new cases/year) of which only 730 millions euro are spent for radiotherapy (160.000 patients/year) (www.etoile.org).

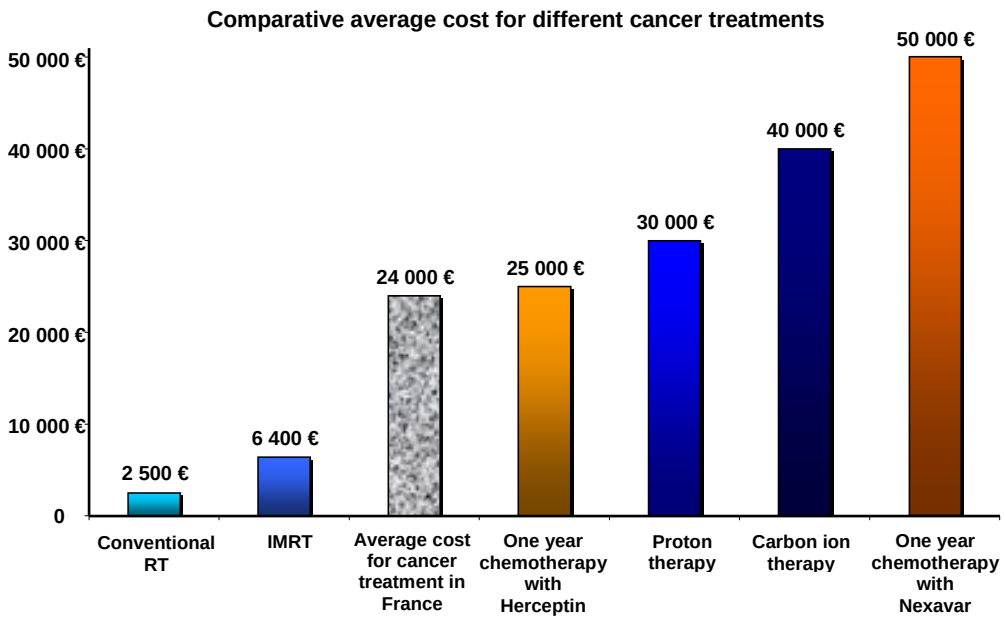

figure 2-5: Comparative average costs for different cancer treatments. Proton and carbon ion therapies are slightly more expensive than the average cost of cancer treatment in France but nevertheless cheaper than regularly employed chemotherapy treatments; adapted from (www.etoile.org).

2.4 Current and future ion therapy centers

The first proposal of using protons and potentially heavier ions, in therapy for their superior depth dose distribution dates back to 1946 (Wilson & others 1946). A decade later the first patients with metastatic breast cancers were treated with protons from the 184-inch synchrocyclotron at Lawrence Berkeley Laboratory LBL (USA) (Tobias et al. 1958). At the end of the 1950s the first cancer treatments in Europe were performed with protons from the synchrocyclotron at the Gustaf Werner Institute in Uppsala (Sweden) (W. T. Chu et al. 1993) while in the early 1960s the Harvard Cyclotron Laboratory (USA) became the first clinical-based center to use proton for cancer therapy (Sisterson 2005). At LBL from 1957 to 1992 about 2000 patients were treated with He-ions and from 1975 to 1992, 403 patients underwent trials with C, Ar, Si and Ne ions (ptcog.web.psi.ch). In 1991 one of the still biggest proton therapy facilities in the world, the Loma Linda University Medical Center (LLUMC), opened in USA and since then more than 14000 patients have been treated in what is considered the first hospital-based center for particle therapy. In the same year, in France, the Medycic cyclotron was installed at the Centre Antoine Lacassagne in Nice, to produce 63 MeV protons for ocular tumour treatment while the same year in Paris, the Orsay 200 MeV proton synchro-cyclotron was converted for exclusively medical use at the Centre de Protonthérapie d'Orsay (CPO) (W. T. Chu et al. 1993). Many of the units for ion beam therapy are still based on nuclear physics accelerator like the Heavy Ion Medical Accelerator (HIMAC) in Chiba (Japan) where in 1994 the first patient was treated with C-ions. At the Gesellschaft für Schwerionenforschung (GSI) Darmstadt (Germany) the first European patient was treated with C-ions in 1997. On the base of the

excellent clinical results obtained on about 4500 patients in Chiba and on 400 patients at GSI, several hospital-based ion therapy centres have been proposed worldwide. The tendency of these new facilities is to combine carbon and proton treatments. The first one opened in Hyogo (Japan) where since 2001 more than 2400 patients have been treated with protons and 600 with C-ions. In Europe, the Heavy Ion Therapy Center (HIT) in Heidelberg (Germany) started the C-ion treatments in November 2009.

The Particle Therapy Cooperative Group (PTCOG) constantly monitors the number of patients that are being treated worldwide and the evolution of the operative and proposed particle therapy centers. According to their most recent report (ptcog.web.psi.ch) 30 proton therapy centers and 3 C-ion facilities are currently operational in the world. Keeping a record of the proposed proton therapy centers is getting harder and harder because of their fast growing number since several companies are now able to sell full scale proton facilities as turn key products. It is on the other hand noticeable, that only in Europe, three dual proton and carbon ion centers are in advance phase of construction in Marburg (Germany), Kiel (Germany) and Pavia (Italy) (Amaldi & G. Kraft 2007). Moreover in France, the national centre for hadrontherapy ETOILE is currently enrolled on the last phase of the call for bids and is foreseen to start the operation in Lyon by the year 2015. Furthermore a dedicated research center called ARCHADE is currently in advance phase of design in Caen.

Since the origin of the particle therapy in 1957 around 61000 patients have been treated with protons and around 9000 patients received therapy with other charged particles. However at present all the running ion-therapy centres perform therapy with proton or carbon ions. Indeed carbon ions seem to offer the optimal compromise between physical selectivity and enhanced biological effectiveness while for still heavier ions like neon, the irreparable cell and tissue damage becomes more important already in the entrance channel (G. Kraft 2000). Nevertheless the discussion about which is the best suited ion for therapy is still on going (Brahme et al. 2001) and at the Heidelberg Ion Therapy Facility (HIT) some trials are planned to investigate the application of He and O-ions to some dedicated tumours (Haberer et al. 2004).

3 Radiation therapy with ion beams

3.1 The physics of interaction of ions with matter

3.1.1 Inverse depth dose profile: stopping of ions in matter

Ions of therapeutic interest to treat deep-seated tumours require ranges in tissues up to 30 cm. This corresponds to specific energies up to 220 MeV for protons *($\beta \equiv v/c \approx 0.6$)*, 430 MeV/u for ^{12}C *($\beta \approx 0.7$)* and 600 MeV/u for ^{20}Ne *($\beta \approx 0.7$)*. In these energy intervals, ions lose and transfer to the traversed medium most of their energy through inelastic collisions with the target electrons. The rate of average energy-loss per unit path length of a given target medium is usually called electronic stopping power of the medium and is represented in figure 3-1 (full lines) for ions from protons to Ne in water. The electronic stopping power can be well described for high velocity ions by the Bethe-Bloch formula (Bethe 1930), (Bloch 1933) reported in equation 3-1 as formulated by (Fano 1963).

$$-\frac{dE}{dx} = \frac{4\pi e^4 Z_t Z_p^2}{m_e v^2}\left[\ln\frac{2m_e v^2}{\langle I\rangle} - \ln\left(1-\beta^2\right) - \beta^2 - \frac{C}{Z_t} - \frac{\delta}{2}\right] \qquad \textbf{3-1}$$

In equation 3-1, Z_p denotes the electric charge of the projectile, Z_t is the atomic number of the target atoms, m_e and e are respectively the mass and the charge of the electron, $\langle I \rangle$ is called the mean ionization energy of the medium, C/Z_t and δ are respectively the shell and density correction terms. Equation 3-1 is valid for the considered light projectile ions energies larger than 10 MeV/u, which represents velocities larger than the mean velocity of the target electrons, and electrons in bound states of the projectile. This implies that the projectile ions are fully stripped of their electrons, and that all target electrons can be ionized. However, equation 3-1 can be extended to lower energies by replacing Z_p by a projectile effective charge Z_{eff} which takes into account the decrease of the mean projectile charge due to the interplay of ionization and recombination processes with the target electrons when ion velocities decrease to values comparable to electron orbital velocities *($\approx 0.008c$)*. The dependence of Z_{eff} on the projectile velocity is described by the empirical formula reported in equation **3-2** (Barkas & D. A. Evans 1963)

$$Z_{eff} = Z_p\left(1 - e^{-125\beta Z_p^{-2/3}}\right) \qquad \textbf{3-2}$$

From the $1/v^2$ term in equation 3-1, it follows that the energy-loss increases with decreasing particle energy. At the end of the track, however, the electronic stopping power drops due to the rapid reduction of the ion effective charge Z_{eff} as described in equation **3-2**, and also to the fact that the energy transferable during ion-electron collisions becomes comparable – or smaller than – the

electron binding energy. This second property is contained in the first logarithmic factor in equation 3-1.

The maximum energy-loss rate, corresponding to the Bragg-peak (Bragg & Kleeman 1905), is reached at a projectile velocity of

$$v_p \approx Z_p^{2/3} v_0 \qquad \textbf{3-3}$$

where $v_0=e^2/\hbar$ is the Bohr velocity. This value of the projectile velocity corresponds typically to the average velocity of the bound electrons of the neutral atom in the Thomas-Fermi model. From equation 3-3 it can be noted that the ion velocity at which the maximum energy-loss is produced depends only on the projectile charge and it increases with increasing charge as shown in figure 3-1.

For ion energies below 10 keV/u elastic collisions with target screened-nuclei begin to contribute significantly to the energy-loss and dominate the stopping process at the very end of the particle path (last few µm). This second mechanism of energy-loss is commonly called nuclear stopping power. Its values are reported as dashed lines in figure 3-1 for ions of therapeutic interest (values for protons are not shown because too small to fit in the ordinate scale).

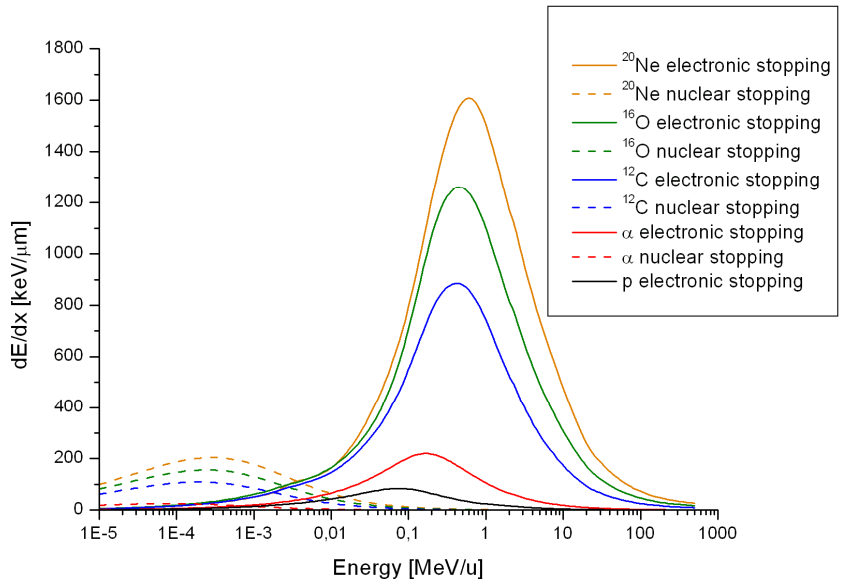

figure 3-1: Electronic (full lines) and nuclear (dashed lines) energy-loss per unit path length dE/dx for ions of therapeutic interest in water. dE/dx values are calculated with SRIM code (Ziegler 2004).

The total energy-loss, defined as the sum of electronic and nuclear stopping power, can be directly linked to the physical dose, defined as the mean energy deposited by the ionizing radiation in a defined mass element of tissue. For a parallel beam of ions with a particle fluence F, the dose deposited in a thin slice of an absorber material with mass density ρ can be calculated with the formula reported in equation 3-4.

$$D[Gy] = 1.6\times10^{-9} \times \frac{dE}{dx}\left[\frac{keV}{\mu m}\right] \times F\left[cm^{-2}\right] \times \frac{1}{\rho}\left[\frac{cm^3}{g}\right] \qquad \textbf{3-4}$$

In equation 3-4, the absorbed dose is calculated in Gray [1Gy=1J/kg] and *dE/dx* represents the total energy loss of particles.

The total path length travelled in a medium by an ion with initial energy E_0 can be calculated by integrating the total energy-loss as reported in equation 3-5.

$$R(E) = \int_{E_0}^{0} \left(\frac{dE}{dx}\right)^{-1} dE \qquad \textbf{3-5}$$

For heavy charged ions, the integral shown in equation 3-5 represents a very close approximation of the mean projected range *(R)* of the particles since ions are very little scattered and travel almost in a straight line. In figure 3-2 we show a comparison between the projected ranges in water for ions of therapeutic interest. It can be noted that the range of ions with the same specific energy scales with a factor of A/Z^2 (where A denotes the mass number and Z the atomic number of the particle) and therefore protons and α particles show the same path in water when plotted as a function of their specific energy.

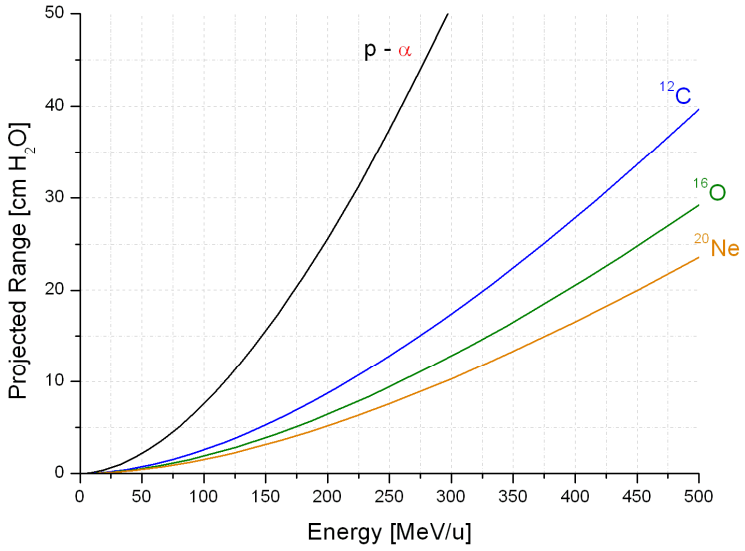

figure 3-2: Projected mean range for ions of therapeutic interest calculated in water with SRIM code (Ziegler 2004).

3.1.2 Range scattering

As it can be seen in figure 3-1, the ratio between the stopping power at the Bragg-peak and at energies of several hundreds MeV/u can rise to factor of hundreds. This is consistent with the energy-loss values which can be calculated with equation 3-1, but in reality, statistical fluctuations of the energy-

loss around its average value occur in the large number of collisions of the slowing-down process. This phenomenon is known as range or energy straggling and it is responsible for the larger Bragg-peak measured for an ion beam with respect to the calculation based on the average energy-loss of a single particle as represented in figure 3-3. The range straggling increases with the penetration depth in a given material, resulting in Bragg-peaks of larger width and smaller height for higher initial energy of the same ions as represented in figure 3-5.

Moreover, the range straggling depends also on the mass of the projectile. The proton Bragg-peak shown in figure 3-3, is larger than the carbon Bragg-peak that arises at the same depth in water, because for different ion species the range straggling approximately varies as the inverse of the square root of the particle mass (Schardt et al. 2010). Indeed the statistical fluctuations on violent binary interactions between the incoming particle and electrons from the medium are the main responsible for range straggling and they are proportional to the ratio between the electron and ion mass. Therefore, at the same penetration depth, heavier ions exhibit a narrower Bragg-peak with a steeper distal fall-off. To give an example, the relative range straggling in tissue amounts to about 1% of the mean range for protons and only to 0.3% for C-ions (Parodi 2004). In clinical practice, however, the profile of the Bragg-peak is broader mainly due to the density inhomogeneities of the penetrated tissues for neighbouring trajectories of the finite beam size (Schardt et al. 2010). Nuclear fragmentation, that will be discussed in the next paragraph, also has an important influence on the Bragg-peak profile whose peak to entrance ratio becomes gradually smaller with increasing particle energy due to their higher fragmentation rate. Finally it can be concluded that the effect of range straggling on therapy applications is always smaller than - or comparable with the unavoidable momentum dispersion of the beam from the accelerator delivery system (Parodi 2004). Moreover, for scanning beam delivery systems, using slice by slice irradiation of the target volume, it can be even advantageous to widen the sharp Bragg-peak to reduce the number of energy steps, leading to significant shorter overall irradiation times and a higher particle fluence per layer (U. Weber & G. Kraft 1999).

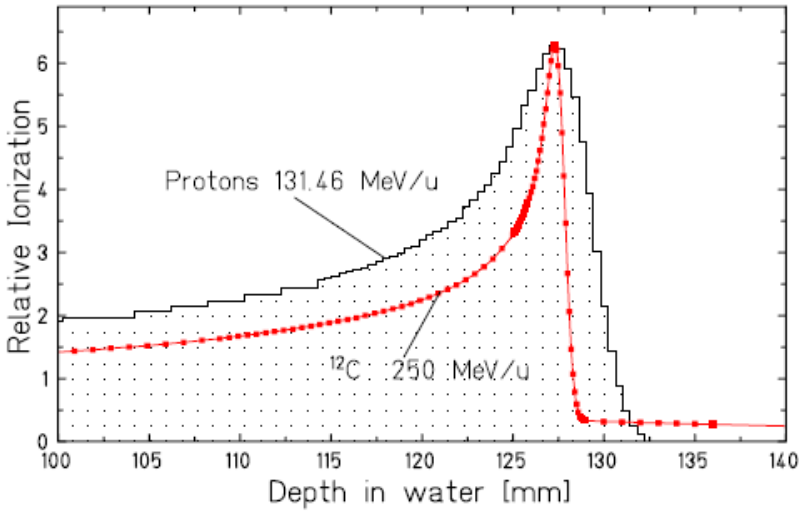

figure 3-3: Comparison of measured Bragg curves of proton and C-ions having the same mean range. The measurements are performed in water with an ionization chamber and are normalized to the same peak height, from (Schardt et al. 2007)

3.1.3 Lateral scattering

Charged particles passing through a medium experience not only interactions with target electrons but also multiple elastic collisions with target nuclei. The statistical repetition of these multiple interactions between ions and target nuclei results in a lateral spread of the ion beam commonly called lateral scattering. The net angular distribution of the outcoming particles after a thick absorber with respect to the incident direction, can be interpreted as the results from several highly probable deflections by small angles and it is well approximated with a Gaussian shape with a standard deviation σ_θ given by the empirical formula proposed by (Highland 1975) and reported in equation 3-6

$$\sigma_\theta = \frac{14.1MeV}{\beta pc} Z_p \sqrt{\frac{d}{L_{rad}}}\left(1+\frac{1}{9}\log_{10}\frac{x}{L_{rad}}\right) \qquad \textbf{3-6}$$

where p is the momentum of the particle, d the thickness of the absorber and L_{rad} the radiation length of the medium. It follows that the angular spread of ions increases as the particle energy decreases due to the βpc term at the denominator of equation 3-6. In figure 3-4 we present a comparison of lateral scattering for different ion species of therapeutic interest. Beams of carbon and heavier ions show little lateral scattering (< 1-2 mm) while the angular spread of protons is on average three times larger. The small lateral deflection of heavy ions penetrating through a thick absorber is a particular advantage of heavy ions in comparison to protons since they allow a safer approach to sensitive structures and a further improvement in the dose distribution in the target area (Schardt et al. 2010). The lateral beam scattering is also of clinical relevance for the treatment of tumours in close vicinity to organs at risk (OAR). Indeed, for the definition of the direction and position of the irradiating ports, the lateral spreading of the beam determines the minimum distance at which an OAR can be approached.

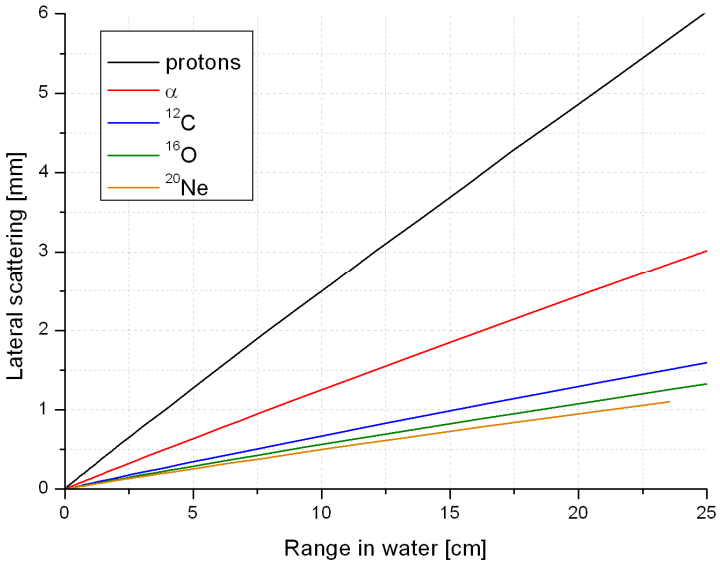

figure 3-4: Lateral scattering in water for ions of therapeutic interest calculated with SRIM code (Ziegler 2004). The small lateral deflection of carbon and heavier ions allow a closer approach to organs at risk (OAR) compared to proton beams.

3.1.4 Ion fragmentation: models and fragments

High energy ions penetrating a thick absorber, not only interact with the target nuclei *via* electromagnetic interactions as described in the previous paragraph, but they experience as well, strong nuclear force interactions resulting in projectile and/or target nuclei fragmentation. The total reaction cross section σ_R describes the probability for an ion of undergoing nuclear fragmentation and it is almost constant over a wide energy range down to about 100 MeV/u (Kox et al. 1987). Indeed, in this energy region, σ_R is mainly given by the geometrical cross sections of overlapping nuclei. On the other hand, at lower energies, σ_R rises due to the contribution of other reaction mechanisms like deep-inelastic collision or fusion reactions (Schardt et al. 2010). At several hundreds MeV/u violent spallation reactions may result in the complete disintegration of both projectile and target nuclei. In the proton case only target fragmentation is possible. For the sake of completeness we mention that nuclear reactions induced by electromagnetic interactions are also possible but always negligible in the energy range of ions used in particle therapy. Additionally, nucleonic reactions leading to pion productions are also possible at the highest ion energies used in hadrontherapy, but they're rare enough to be completely irrelevant for practical purposes.

Heavy-ion nuclear reactions may be classified according to the value of the impact parameter between the trajectories of the two colliding nuclei. We can therefore distinguish three main classes: central collisions, peripheral collisions and various Coulomb force induced processes also named distant or barrier processes (V. Crespo 2006). For geometrical reasons peripheral collisions, where the beam particle loses one or several nucleons, are the most frequent reactions and they can be well described by the abrasion-ablation model as a two step

process (Oliveira et al. 1979). In the first step nucleons are abrated in the overlapping reaction zone ("fireball"), prefragments are produced within ≈ 10^{-22} s, while the outer "spectator" nucleons are only slightly affected (Hüfner 1985). In a second step (~ 10^{-21} to 10^{-16} s) the excitation energy in the fireball and fragments is released by evaporation (ablation) of nucleons. The emission of prompt photons from giant dipole resonance (GDR) are also possible in this second step, but they are of several order of magnitude rarer than the de-excitation through nucleon evaporation (d'Enterria et al. 2001). Thereafter, when the energy of the excited products falls below the nucleon separation threshold, only emission of prompt γ-rays is allowed (Mollenauer 1962).

Dedicated fragmentation studies for application in particle therapy were performed over many years at LBL Berkeley for the characterisation of the 670 MeV/u beam of ^{20}Ne which was used for treatment (Llacer et al. 1990). Similar studies were performed at HIMAC facility (Schall et al. 1996), GANIL facility (Braunn et al. 2010) and SIS-18 synchrotron at GSI (Schardt et al. 1996) for C-ions among other species. Three main conclusions can be drawn for the effects of fragmentation relevant to radiotherapy with high-energy ion beams (Schardt et al. 2010):

i. Nuclear reactions cause a loss of primary beam particles and a buildup of lower-*Z* fragments which become more and more important with increasing penetration depth. Indeed, as clearly depicted in figure 3-5, with increasing penetration depth the peak to entrance dose ratio becomes gradually smaller mainly because of the diminishing flux of primary ions. Fragmentation rate can rise to 70% for C -ions at 400 MeV/u and, on average, 50 % of primary ions utilized in a typical tumour irradiation undergo nuclear fragmentation (Haettner et al. 2006). Additionally, as already described in the previous paragraph, the Bragg-peaks shown in figure 3-5 are increasingly broadened by the energy straggling.

ii. The secondary, or higher-order, projectile like fragments move with about the same velocity as the primary ions. Since they are lighter than the primary ions, they have in general longer ranges and produce a dose tail beyond the Bragg peak clearly visible in figure 3-5.

iii. The angular distributions of fragments are mainly determined by reaction kinematics and forward directed, but much broader than the lateral spread of the primary ions caused by multiple Coulomb scattering (Gunzert-Marx et al. 2008). Generally, the lower the mass fragment the broader the distribution (Haettner 2006).

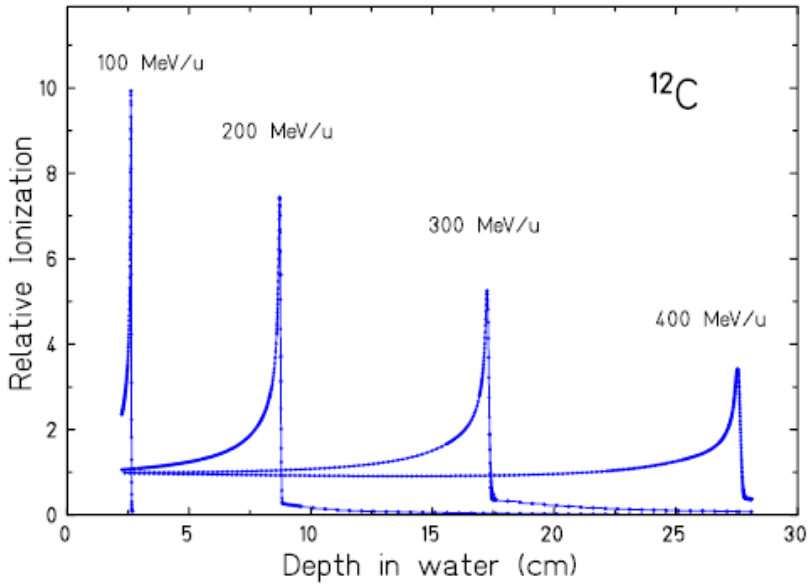

figure 3-5: Measured Bragg-curves for C-ions of different energies stopping in water. The measurements are performed with an ionization chamber in water; from (Schardt et al. 2010).

In general, heavy-ion nuclear fragmentations are responsible for the deterioration of the dose distribution both in the longitudinal and transversal dimensions especially in the Bragg-peak region. Nevertheless, for C-ions the fragmentation is still within an acceptable limit, especially when using active beam delivery systems to avoid projectile fragmentation before entering the patient (Parodi 2004). Furthermore, the positron emitting-fragments like ^{10}C and ^{11}C can be utilized for *in vivo* range monitoring with positron emission tomography (PET) as it will be described in more detail in the next chapter. Charged fragments escaping from the patient (mainly protons and He-ions) are currently proposed for *real-time in-vivo* range verification with the interaction vertex imaging (IVI) technique (see chapter 4) as well as prompt γ-rays emerging orthogonally to the beam direction have been proved to be correlated with the primary ion path both for proton beams (Min et al. 2006) and C-ion beams (E. Testa et al. 2008).

Finally, during a particle irradiation, a considerable amount of neutrons are produced with a very broad angular spectrum (E. Testa et al. 2009) and although they cannot be exploited for primary range verification since they are uncorrelated with the ion path (M. Testa et al. 2010) some discussions have been raised about the role of these neutrons for the risk of late effects and inducement of secondary cancer (Paganetti et al. 2006). Even though it was pointed out that the neutron dose depends on the beam delivery system (Gottschalk 2006), with scanned proton beams a negligible neutron dose of 2 mSv per treatment Gy was measured at PSI Switzerland (Schneider et al. 2002) and a still negligible 8 mGy of neutron dose per treatment Gy was estimated for C-ions irradiation at GSI Germany (Gunzert-Marx et al. 2008).

3.2 The physics of interaction of photons with matter

Although a large number of possible reaction mechanisms are known for γ-rays in matter, only three major types play an important role in radiation measurements: photoelectric absorption, Compton scattering and pair production (Knoll 1989). All these processes lead to the partial or complete transfer of γ-ray photon energy to electron energy. The behaviour of photons in matter is dramatically different from that of charged particles described in the previous paragraphs. In particular, the photons' lack of charge makes impossible the many inelastic collisions with atomic electrons characteristic of the gradually slow down of charged particles. This kind of reaction explains the two main qualitative features of γ-rays that are *i)* more penetrating in matter than charged particles due to the much smaller cross section of the three processes mentioned above relative to the inelastic electron collision cross section and *ii)* a beam of photon is not degraded in energy as it passes through a thickness of matter but only attenuated in intensity because photons either disappear entirely or are scattered through a significant angle out of the beam (Leo 1994).

3.2.1 Photoelectric effect, Compton scattering, Pair production

The **photoelectric effect** involves the absorption of a photon by an atomic electron with the subsequent ejection of the electron from the atom. The energy of the outgoing electron is then given by the following expression

$$E_e = h\nu - E_b \qquad \textbf{3-7}$$

where E_b is the atomic binding energy of the electron, $h\nu$ is the energy of the incoming photon and E_e the energy of the photoelectron. Since a free electron cannot absorb a photon and also conserve momentum, the photoelectric effect always occurs on bound electrons with the nucleus absorbing the recoil momentum (Jackson 1975). Therefore, tightly bound inner-shell electrons, located close to the nucleus, are more subject to be photo-ionized than outer-shell electrons. In addition to the photoelectron, the interaction also creates an ionized absorber atom with a vacancy in one of its bound shells. This vacancy is quickly filled through rearrangement of electrons from other shells of the atom (Auger cascades which lead to further ionizations, or radiative decay), and then capture of one or several free electrons from the medium. Therefore, one or more characteristic X-ray photons may also be generated, or in some cases, the emission of an Auger electron may substitute for the characteristic X-ray in carrying away the atomic excitation energy (Jackson 1975). In figure 3-6 we show the total photon cross section for tungsten and water as a function of the incident photon energy. In the case of tungsten it can be clearly seen that the photoelectric cross section (red curve) is maximum if the photon has just enough energy to knock the electron from its shell. These maxima are known as K-L-M-absorption edges. Just below these points, the cross section drops drastically since the K-L-M electrons are no longer available for the photoelectric effect. Below these energy-edges the cross section rises once again to dip when the next electron shell energy is reached. The photoelectron cross-

section varies with photon energy approximately as $1/(h\nu)^3$ while the dependence on the atomic number Z of the traversed medium, at MeV energies, goes as Z to the 4th and 5th power that implies that the higher Z materials are most favoured for photoelectric absorption. In all cases, even for heavy elements like tungsten, the photoelectric effect can be neglected at energies of 1 MeV or higher.

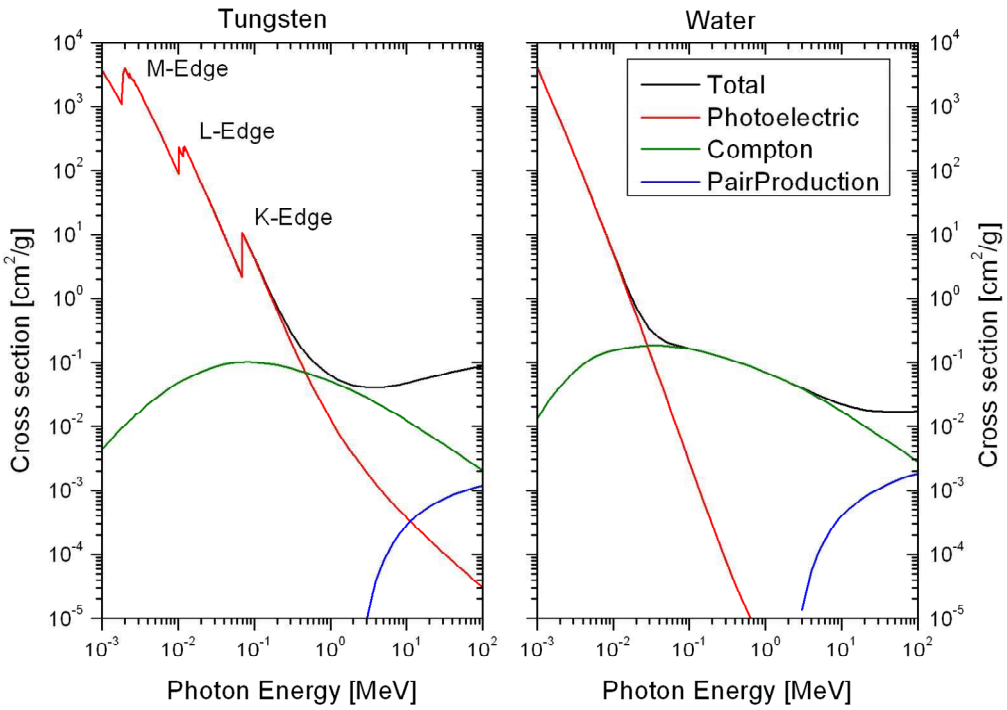

figure 3-6: Total, photoelectric, Compton and pair production cross section for photons interacting with tungsten (left) and water (right). Data from XCOM photon cross section (Berger et al. 1998)

Compton scattering, also called incoherent scattering, is most often the predominant interaction mechanism for γ-ray energies of several MeV. It is the most important interaction mechanism in tissue-like materials in the energy range form 100 keV to 20 MeV (H. E. Johns & Cunningham 1983) as it can be seen in figure 3-6, where in the case of water the Compton cross section (green line) represents the major contribution to the total photon cross section.

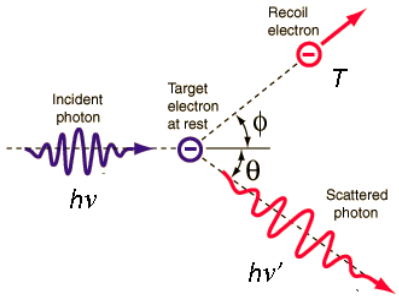

figure 3-7: Kinematics of Compton scattering

As depicted in figure 3-7, Compton scattering occurs on free electrons, in the sense that no recoil is transferred to a nucleus. In matter, of course, electrons are bound but if the photon energy is high with respect to the binding energy, this latter can be ignored and the electrons can be considered as essentially free. Applying energy and momentum conservation to the system formed by the incoming photon and the electron at rest, we can obtain the following relations describing the outgoing energy and scattering angle for both the electron and photon. Using the symbols defined in the sketch of figure 3-7, we obtain (Leo 1994):

$$h\nu' = \frac{h\nu}{1+\gamma(1-\cos\theta)} \qquad 3\text{-}8$$

$$T = h\nu - h\nu' = h\nu\frac{\gamma(1-\cos\theta)}{1+\gamma(1-\cos\theta)} \qquad 3\text{-}9$$

$$\cos\theta = 1 - \frac{2}{(1+\gamma)^2\tan^2\phi + 1} \qquad 3\text{-}10$$

$$\cot\phi = (1+\gamma)\tan\frac{\theta}{2} \qquad 3\text{-}11$$

where $\gamma = h\nu/m_e c^2$ and $m_e c^2$ is the mass-energy of the electron (0.511 MeV). In general Compton scattering cross section depends on the number of electrons available in the absorber and therefore increases linearly with Z, while it decreases with increase in photon energy (approximately like $1/h\nu$). In each collision some energy is scattered and some is transferred to an electron according to equation 3-8 and 3-9 the relative amount of these energies depends on the angle of emission of the scattered photon (equation 3-10) as can be seen from figure 3-8 and the energy of the photon itself. On average, the fraction of energy transferred into kinetic energy of the electron increases with increase in photon energy as well as the strong tendency for forward scattering at high values of γ-ray energy (Knoll 1989).

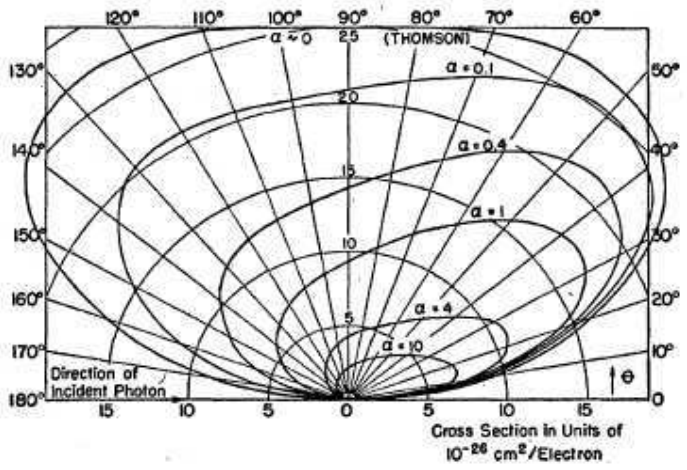

figure 3-8: Differential Compton cross-section per unit angle for the number of photons scattered in the direction θ. Figure from (Davisson & R. D. Evans 1952)

When the energy of the incident photon is greater than 1.022 MeV the photon may be absorbed through the mechanism of **pair production**. This is an

example of conversion of energy into mass that involves the transformation of a photon into an electron-positron pair. In this process, no net electric charge is created since the electron and positron carry opposite charges. If the photon has an energy that exceeds 1.022 MeV, this excess energy is shared between the kinetic energy of electron and positron. Because the positron will subsequently annihilate after slowing down in the absorbing medium, two annihilation photons are normally produced as secondary products. The pair production cross section (blue lines in figure 3-6) increases rapidly with increase in energy above the threshold of 1.022 MeV and since it occurs in the field of the nucleus, cross sections per unit mass are linearly dependant with the atomic number of the interacting medium. Well above the threshold, the pair creation cross section still increases with energy, like ln(E).

For the sake of completeness we will mention that three other processes exist for photons interacting with matter: Thomson scattering, Rayleigh scattering and triplet production. Their cross sections are always negligible when compared to photoelectric absorption, Compton scattering and pair production. Thomson scattering is the scattering of photon by free electrons in the classical limit, while Rayleigh scattering, also called coherent scattering, is the scattering of photons by atoms as a whole. In both processes, the scattering is characterized by the fact that no energy is transferred to the medium, the atoms are neither excited nor ionized and only the direction of photons is changed (Leo 1994). Triplet production is the same of pair production except that the interaction occurs in the field of the electrons instead of the nucleus. Thus three energetic particles appear: the positron, the created electron and the original electron recoiling. The threshold for tripled production may be shown to occur at twice the threshold for pair production thus 2.04 MeV (H. E. Johns & Cunningham 1983). As pair cross section scales as the square of the charge of the target particle well above threshold, the total pair production cross section scales as $Z(Z+1)$ for an atom of charge Z. The second term accounts for triplet production.

Finally, when a single photon interacts with matter, any of the three main interaction processes (photoelectric absorption, Compton scattering and pair production) may occur. In any one interaction only one process can take place, but in many interactions all of them may occur. The relative probability of each type of interaction is proportional to the cross section for that process. The probability of an interaction is proportional to the sum of the cross sections expressed by the total attenuation cross section (black lines in figure 3-6) and reported in equation 3-12

$$\mu_{tot} = \tau_{photoelctric} + \sigma_{Compton} + \kappa_{pair} \qquad \textbf{3-12}$$

To calculate the total photon cross section for compounds such as water, the absorption coefficients can be determined by simply adding the individual coefficients for the atoms involved according to the weight of each element in the compound.

3.3 The physics of interaction of neutrons with matter

Neutrons have no charge and therefore cannot undergo electromagnetic interaction with electrons and nuclei of the traversed matter which dominates the energy-loss mechanism for charged particles. Instead, their principal means of interaction is through the strong force with nuclei. These reactions are much rarer in comparison because of the short range of this force. Neutrons must come within ≈ 10^{-13} cm of the nucleus before any interaction process can happen, and since normal matter is mainly empty space, neutrons are observed to be very penetrating particles (Leo 1994). The relative probabilities of the various types of neutron interaction change dramatically with neutron energy. The main nuclear process a neutron may undergo can be listed in the following:

i. Elastic scattering from nuclei A(n,n)A: this is the principal mechanism of energy-loss for neutron in the MeV region. In this reaction, the secondary radiation is constituted by recoil nuclei, which have picked up detectable amount of energy from neutron collision. At each scattering site the neutron loses energy and is thereby moderated or slowed down to lower energy while its direction is changed. The most efficient moderator is hydrogen because the neutron can lose up to all its energy in a single collision. For heavier nuclei only a partial energy transfer is possible and the maximum possible recoil energy E_{Rmax} for a nucleus with atomic number A, knocked by a neutron with energy E_n is given by equation 3-13 (Knoll 1989)

$$E_{R\max} = \frac{4A}{(1+A)^2} E_n \qquad \textbf{3-13}$$

Especially at low neutron energy, elastic scattering tends to be very probable and often serves to bring the slow neutron to thermal equilibrium (0.025 eV at room temperature) with the absorber medium before a different type of reaction takes place.

ii. Inelastic scattering A(n,n')A*, A(n,2n')B: if the energy of the neutron is sufficiently high the nucleus can be left in an excited state which may later decay by γ-ray or some other form of non-radiative emission including evaporation of another neutron leading in this case to neutron multiplication. In order for inelastic reactions to occur, the neutron must have sufficient energy to excite the nucleus, usually on the order of 1 MeV or more. Finally, high energy hadron shower can take place for very high neutron energies (E>100 MeV).

iii. Radiative neutron capture n+(Z,A)→γ+(Z,A+1): in this reaction a neutron is captured by an absorbing nucleus that releases the neutron excess energy through radiative emission. In general, the cross section for neutron capture goes approximately as *1/v* where *v* is the velocity of the neutron. Therefore, neutron absorption is more probable at low energies and, depending on the element, there may also be resonant peaks superimposed upon the *1/v* dependency.

iv. Other nuclear reactions, such as (n,p), (n,d), (n,t), (n,α), (n,np), (n,nd), (n,nα), (n,fission): in these kinds of reactions a neutron is captured by an absorbing nucleus and charged particles are emitted. As for the radiative capture reactions, the cross section falls as 1/v. Therefore, because the incoming neutron energy is usually very low, all such reactions must have a positive Q-value (difference between internal energy of reactants and products) to be energetically possible (Knoll 1989).

The total probability for a neutron to interact in matter is then finally given by the sum of the individual cross sections as reported in equation 3-14

$$\sigma_{tot} = \sigma_{elastic} + \sigma_{inhelastic} + \sigma_{radiative} + \sigma_{capture} \quad \textbf{3-14}$$

where $\sigma_{elastic}$, $\sigma_{inhelastic}$, $\sigma_{radiative}$ and $\sigma_{capture}$ define the cross sections for the four neutron interaction processes described above.

4 Current and proposed methods for dose verification and monitoring in particle therapy

Dose monitoring and verification in particle therapy is a non trivial task since ions, contrary to photons, fully stop in the target. Therefore, to reveal a possible mismatch between the planned and actual ion range or integral dose, it is necessary to detect secondary radiation which is able to escape from the patient. This includes both prompt emission of photons or secondary particles like neutrons or protons and delayed radiative decay of instable nuclei. These instable nuclei can either be formed in the target by nuclear fragmentation of originally stable isotopes or directly being used as primary ions in therapy with Radioactive Ion Beams (RIB). The radioactive ions used in RIB therapy are positron emitters whose 511 keV annihilation photons are imaged by means of positron emission tomography (PET). At the HIMAC facility a dedicated beam line for radioactive beams (^{10}C and ^{11}C) including a raster scan system was set up but so far no patients have undergone a full RIB therapy mainly due to the limitation in the beam intensity that are still one or two orders of magnitude lower than the regular intensity used in therapy with stable ions (Kitagawa et al. 2006). An alternative use of RIB had been proposed at LBL, Berkeley, where the basic idea was to verify the correctness of treatment plans for stable ^{20}Ne by depositing positron emitters ^{19}Ne at low dose prior to treatment and measure their range in the patient (Chatterjee et al. 1981). The same proposal was followed at HIMAC where positron emitters ^{10}C and ^{11}C were used to verify the range accuracy of stable ^{12}C used in therapy (Iseki et al. 2004). However, since the amount of activity that can be deposited at low dose is quite small, a high-detection efficiency PET is essential.

4.1 PET and TOF-PET

Positron emission tomography (PET) is currently the only clinical method for *in vivo* and *in situ* monitoring in charged particle therapy (Enghardt et al. 1992). During the irradiation, positron emitters like ^{15}O and ^{11}C are formed in nuclear reactions between ions and tissues. The detection of this transient radioactivity via PET and the successive comparison with Monte Carlo simulations based on the prescribed beam application is used as a non invasive validation method of the whole treatment planning and delivery chain (Parodi et al. 2008). Two different technical implementations are usually employed.

For in-beam PET as realized at GSI Darmstadt, a customized, limited angle detector with data acquisition synchronized with the beam delivery, is directly installed in the treatment room and the PET acquisition is performed in between the spill extraction pauses and for approximately 40 seconds after each irradiation fraction (Enghardt et al. 2004).

Alternately, in off-line PET systems, the patient is moved, shortly after the irradiation, to a commercially PET scanner in close proximity to the treatment site. This second option is employed for example to patients undergoing proton

therapy at MGH Boston (Parodi et al. 2008) and it has been studied for C-ion dose verification at the HIMAC facility although it is not used in clinical routine (Schardt et al. 2010). In-beam solutions are technically very demanding but offer the appeal of monitoring individual fields in the treatment position, without losing the significant activity contribution from the short-lived ^{15}O emitter. Off-line full-ring tomographs are commercially available and typically offer better imaging performances with respect to in-beam limited angle detectors. The main drawbacks are patient re-positioning issues as well as the loss of signal from short-lived emitters and the larger influence of metabolic processes in the time elapsed between irradiation and imaging. Moreover, post-treatment imaging only detects the integral beam delivery, with a loss of range information in the case of multiple treatment fields (Parodi et al. 2008).

The most crucial difference between the application of PET imaging systems to proton and carbon beams is shown in figure 4-1. For C-ions irradiation (upper part of figure 4-1) a peak in the β^+-activity is formed in close proximity of the Bragg-peak (shown as a dashed line). This is due to the contribution of positron emitters ^{10}C and ^{11}C which have almost the same range as the primary ^{12}C-ions. On the contrary, the relation between the proton depth-dose curve and the β^+-activity profile (shown in the bottom part of figure 4-1) is poorer due to the lack of projectile fragmentation which implies that no maximum of positron radioactivity is formed at the end of the primary proton range (Parodi et al. 2002). Furthermore, the proton induced activation of the target nuclei vanishes in the last few millimeters of the primary particle path because of the larger intrinsic energy threshold of nuclear reactions. Nevertheless, this lack of peak structure in the activity profile, which is a drawback in comparison with C-ions, is balanced in some extend by the three times higher total induced activity per Gy for protons (Parodi et al. 2002) which is due to the about 40 times higher number of protons compared to C-ions necessary to deliver the same effective dose (G. Kraft 2000). In any case the main drawback of PET imaging applied to particle therapy is the low β^+ activity induced by fragmentation: about 200 Bq Gy^{-1} cm^{-3} for ^{12}C and about 600 Bq Gy^{-1} cm^{-3} for protons (Enghardt et al. 2004). In fact, these values are 2-3 orders of magnitude lower than radioactive tracer activity used in conventional PET imaging.

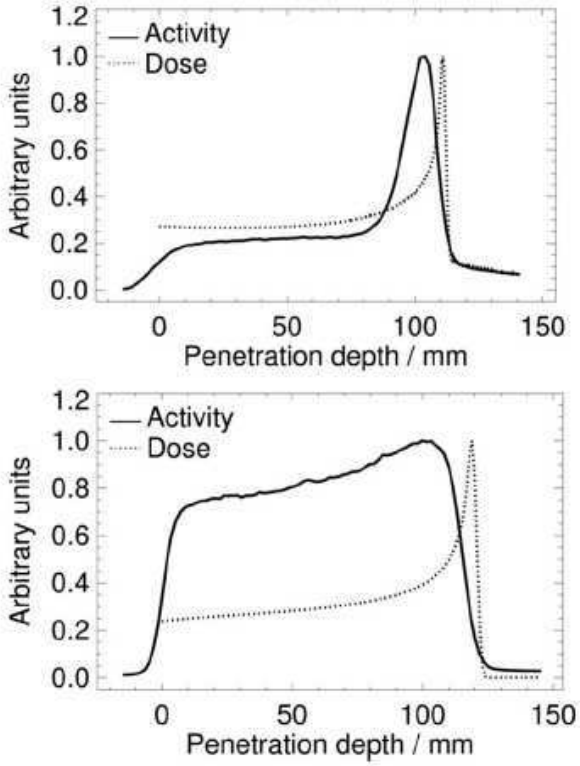

figure 4-1: Measured autoactivation of thick PMMA targets by means of 260 MeV/u carbon ions (top) and 140 MeV protons (bottom). The solid lines show the depth profiles of the measured β^+ activity. For comparison the depth-dose profile of the primary beam is shown as dotted line. Figure from (Parodi 2004).

An in-beam PET system for C-ion beams has been employed routinely for monitoring almost all the 440 patient treatments administered since 1997 at GSI and it has proven to be a valuable tool for quality assurance (Schardt et al. 2010). The positron activity is correlated but not directly proportional to the spatial pattern of the delivered dose. Hence, therapy control is achieved by visually comparing the measured β^+-activity distribution with a Monte Carlo prediction based on the treatment plan and the specific time course of the irradiation as depicted in figure 4-2. In case of observed discrepancies between the measured and expected PET images the radio-oncologist is provided with a quantitative estimation of the deviation between the planned and actually applied physical dose (Parodi 2004). Before the next irradiation fraction the radiotherapist can therefore expose the patient to a new X-ray CT for further investigation of possible anatomical changes and, in case of significant deviation between planned and applied dose, a new treatment plan can be elaborated. To summarize, the PET monitoring technique developed at GSI permitted i) monitoring the maximum ion range, ii) verifying the field position, and iii) detecting deviations in the patient positioning or local changes of the patient anatomy in the course of the treatment (Schardt et al. 2010).

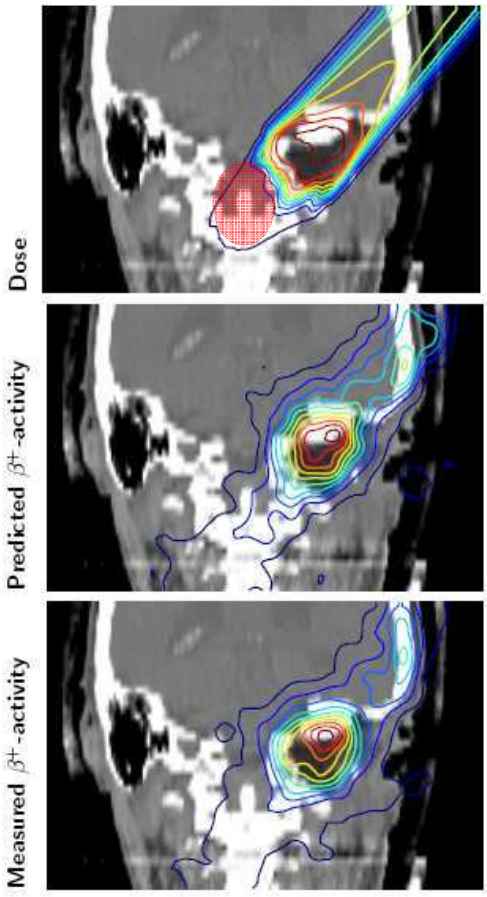

figure 4-2: Dose distribution (top) versus β^+ activity distribution predicted from the treatment plan (middle) and measured (bottom) after a skull base tumour irradiation at GSI. The planned dose distribution is superimposed onto the CT image where the brain stem as organ at risk is highlighted. By comparison with the prediction it is shown that the C-ions stop before the brain stem. Adapted from (P. Crespo et al. 2006).

An extrapolation study based on the impact of recent detector and scintillator developments, enabling sub-nanosecond coincidence timing resolution (τ), has been performed by (P. Crespo et al. 2007) in order to assess the feasibility of a time-of-flight (TOF) PET scanner allowing *real-time in-beam* quantitative verification of the applied dose in C-ion therapy. The authors claim that for $\tau \leq$ 200 ps full width at half maximum (FWHM) timing resolution, *in-beam* TOF-PET images could become available even during the course of therapeutic irradiations mainly due to the immense decrease in data processing time allowed by the use of TOF (mainly due to the increase of signal to noise ratio by reducing the volume of the region observed). Moreover the TOF information would allow a considerable reduction of image artefacts that arise from limited-angle tomography. Nevertheless, although the progress in both detector and electronic fields are rapid, at present, no evidence is shown that such a device could currently be employed in a clinical environment. Additionally, the positron signal detected by PET is intrinsically delayed with respect to the fragmentation processes taking place during the irradiation and the extremely low induced β^+ activity represents a further challenge for *real-time* PET imaging.

4.1.1 Ion range verification with PET

In the previous paragraph it was pointed out that ion range verification has been one of the most important quantities deduced from PET monitoring. More in detail, the systematic deviations observed between measured and recalculated PET images in the early therapy session at GSI Darmstadt in 1998, indicated a lack of accuracy in the carbon ion range, especially in the soft tissue regions (Parodi 2004). These deviations were imputed to the non optimal calibration of the correlation curve between CT Hounsfield numbers and water-equivalent path length (M. Krämer et al. 2000) that was therefore successively corrected (Enghardt et al. 2000). Consequently, the higher reliability of the precision on the ion range in tissue allowed extending treatment plans to more critical irradiation field like cranio-lateral portal in which the beam has to be stopped precisely in the tumour in front of the brain stem that in this case represents the organ at risk (Parodi 2004).

The analysis of PET images for 205 patients treated at GSI Darmstadt until 2003 led to new X-ray CT re-exposure for 6 of them (Parodi 2004). In 5 cases the investigation confirmed a local anatomical change and for one patient a new treatment plan was elaborated. For sake of objectivity, it has to be pointed out that, in practice, proper safety margins and careful selections of the beam portals are always taken into account to avoid too delicate irradiation fields and therefore, in all the observed cases of ion range deviation, no serious clinical consequences were encountered (Parodi 2004).

More recently Fiedler et al. performed a first quantitative study on the accuracy of the in-beam PET method to detect range deviations between the planned and applied treatment in clinical relevant situation using simulations based on clinical data obtained with 81 patients treated at GSI Darmstadt (Fiedler et al. 2010). For each patient a range difference of ±6 mm in water was virtually applied to produce simulated PET images which have been visually compared by six experienced evaluators to PET images without any change. The results indicate that over and lower ranges have been recognized by the evaluators in about 90% of the cases. Nevertheless there is strong evidence that specific effects impede the visibility of range deviations, such as beam passing through inhomogeneous tissues, large irradiation volumes as well as low dose. To show an example, in figure 4-3 are reported the profiles of the reconstructed β^+ activity distribution taken in a beam direction crossing the isocenter field of view of the PET camera. In figure 4-3a is represented a case of a patients in which the over and lower ranges on the PET images have been correctly recognized while in figure 4-3b the majority of the evaluators failed in detecting the range differences. Anyhow, as already stated, PET demonstrated to be a valuable tool for *in vivo a posteriori* range verification.

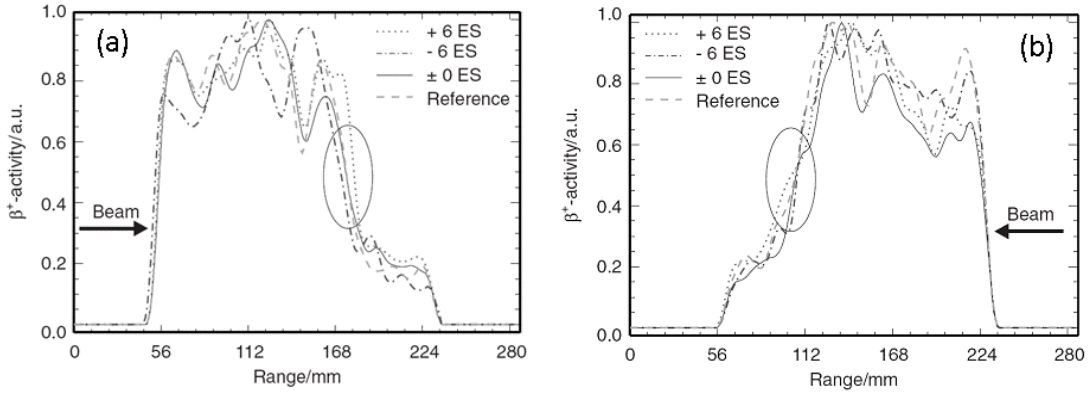

figure 4-3: Profiles of reconstructed β^+-activity distribution taken in a beam direction crossing the isocenter field of view of the PET camera. The different activity distributions are drawn for range variations of ±6 energy steps (ES) corresponding to projected range variation in water of ±6 mm. The ±0 ES curve differs from the reference distribution only by statistical fluctuations during the simulation. The region where the range difference is expected is marked as an ellipse. In (a) it is shown a case of a patient in which the over and lower ranges have been correctly recognized while in (b) it is shown an example of patient in which the majority of the evaluators failed to detect the differences in ranges ; figure adapted from (Fiedler et al. 2010).

4.2 Prompt photon radiation

Prompt γ-ray emission from excited fragments produced either during the impact of ion beams with a target (Riess 1989) or from nuclear fission products (Nifenecker et al. 1972) is a well known phenomenon which has been exploited for several purposes. For example, nondestructive assay methods that rely on measurement of prompt γ-rays from nuclear fission have been proposed as a means to determine the mass of fissile materials in the field of nuclear safeguard measurement (Valentine 2001). Moreover, at several neutron spallation sources, the prompt gamma-ray activation analysis (PGAA) is used as non-destructive method for determining the presence and amount of many elements simultaneously in samples which are continuously irradiated with a beam of neutrons (Dilmanian et al. 1998). The constituent elements of the sample absorb some of these neutrons and emit prompt γ-rays which are measured with high-resolution γ-rays spectrometers (Crittin et al. 2000). PGAA is then based on the fact that the energies of these γ-rays identify the neutron-capturing elements, while the intensities of the peaks reveal their concentrations.

In medical field, prompt gamma spectroscopy has been proposed as an in-vivo non invasive technique to determine the boron uptake in tumors treated with Boron Neutron Capture Therapy (BNCT) (Rosenschöld et al. 2001). The technique is based upon the measurement of γ-rays promptly emitted in the $^{10}B(n,\alpha)^{7}Li$ and $^{1}H(n,\gamma)^{2}D$ reactions. The amount of prompt γ-rays is then correlated with the boron concentration in the tumor or directly evaluated as a measure of the absorbed dose due to the neutron capture reactions in boron and hydrogen (Kobayashi et al. 2000).

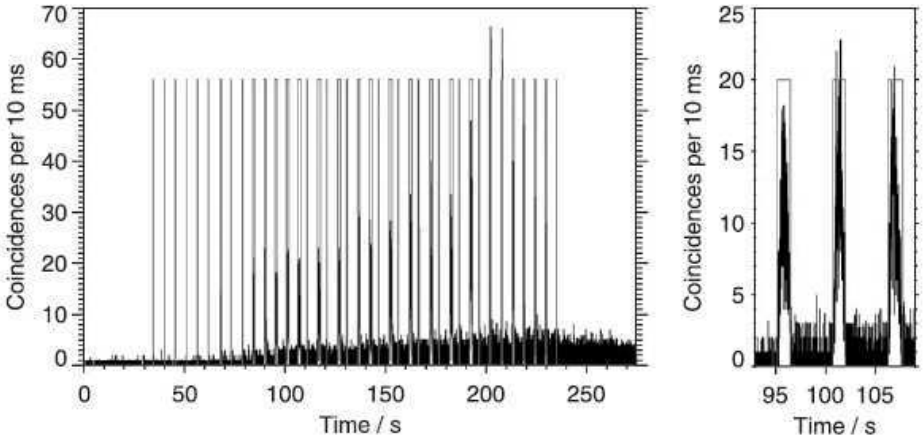

figure 4-4: Example of the time course of the coincidence rate acquired by the in-beam PET camera during the application of an entire treatment field to a patient at GSI. The rectangular pulses, better visible in the enlarged view on the right-hand side, indicate the beam extractions from the synchrotron. The coincidence rate during beam extraction is about one order of magnitude higher than during the beam pauses due to the high amount of prompt γ-rays emitted within the spill time course; figure from (Parodi et al. 2005).

In the domain of charged particle therapy, as already discussed above, in-situ monitoring of the dose delivery is currently performed with PET. Here prompt γ-rays represent noisy events that cannot be separated at present from the usable decays of long-lived β^+-emitters, which generate the valid signal detected by positron tomographs (Parodi et al. 2005). Indeed, as clearly shown in figure 4-4, the coincidence rate acquired by the positron camera during the beam extraction is about one order of magnitude higher than during beam pauses. This is due to the high amount of single γ-rays promptly emitted during the beam extraction pulses which, by definition, produce fake coincidence signals. For this reason, at GSI Darmstadt, the status (on or off) of the beam delivered by the synchrotron in spills of about 2 s duration followed by 3 s pause (Parodi et al. 2005) was recorded in order to allow the discard of all coincidence signals registered during particle extraction (Enghardt et al. 2004). With the irradiation scheme presented in figure 4-4, the rejection of the in-spill data was roughly estimated to reduce the counting statistics up to 40% and a worse situation is expected for synchrotrons dedicated to ion-therapy, in which the duty cycle (ratio between spill and pause duration) will be increased to reduce the overall treatment time (Parodi et al. 2005).

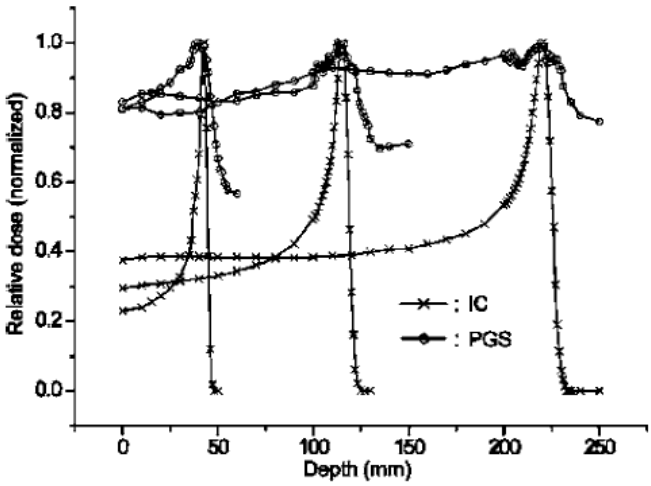

figure 4-5: Comparison of the depth-dose distribution at proton energies of 100, 150 and 200 MeV, measured by ionization chamber (IC) and right-angled prompt- γ-rays with the prompt gamma scanner (PGS). The correlation between the prompt gamma distribution and the Bragg-peak is within 1-2 mm for the first curves with proton energy of 100 MeV; figure from (Min et al. 2006).

More recently, a series of experiments demonstrated that the measurement of prompt γ-rays could be directly correlated with the ion range in proton (Min et al. 2006) and C-ion therapy (E. Testa et al. 2008). As in the case of PET systems, it is assumed that the nuclear fragmentation of both primary beam and target nuclei is correlated with the particle range. Indeed fragmentation occurs almost all along the ion path till 2-3 mm before the Bragg-peak where nuclear reaction cross sections start dropping when the available energy in the projectile-target nuclei center of mass approaches the Coulomb barrier. This implies that, in principle, the measurement of the emitted prompt photons, raised from primary and secondary ion nuclear interactions, could bring valuable information both on the dose distribution and on the Bragg-peak position. The latter point was verified with proton beams by Min et al. with an accuracy of 1-2 mm for protons at 100 MeV as reported in figure 4-5.

The extension of the work by Min et al. to C-ion beams was performed by our group at the GANIL facility (Caen, France) in 2007 with 73 MeV/u $^{13}C^{6+}$ ions impinging on a PMMA target. The details of this experiment and the following ones will be discussed in the next chapter, but it can already be stated that, as shown in figure 4-6, the correlation between prompt photons and the Bragg-peak was obtained even for C-ions in which both target atoms and primary ions undergo nuclear fragmentation (E. Testa et al. 2008). Moreover, the discrimination between prompt photons and background radiation made with time of flight (TOF) represents the main characteristic of our experimental set-up and it avoids the use of bulky neutron shielding like in the case of the work presented by Min et al. As it will be discussed in the next paragraph, this feature is of particular importance since it permits to significantly reduce the size of the shielding material (E. Testa et al. 2009) allowing a stacked multi-detector set-up that, in principle, can be employed clinically for *real-time in-situ* ion range monitoring.

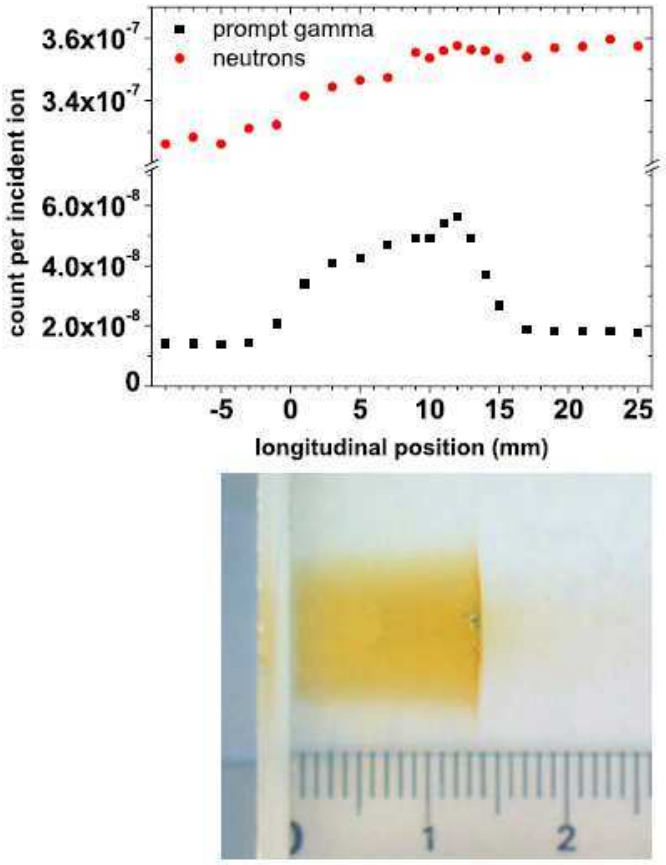

figure 4-6: Upper part: detection rates as a function of the longitudinal position of target, obtained for two different time of flight (TOF) selections: prompt -rays (square symbols) and neutrons (round symbols). Bottom image: scaled photograph of the irradiated PMMA sample; figure from (E. Testa et al. 2008)

Coming back to protontherapy, the discussion about the potential use of prompt γ-ray emission as a method to verify the accuracy and efficacy of dose delivery during proton irradiation was recently raised by Polf et al. In a first work based on Monte Carlo simulations they presented the results of a preliminary study on secondary prompt γ-ray emission produced within tissue during proton irradiation (Polf, Peterson, Ciangaru et al. 2009). In a second work, they performed measurements of prompt γ-ray spectra using a detector shielded either with lead or a Compton suppression system (Polf, Peterson, McCleskey et al. 2009). Although in both studies the analysis was focused only on the characteristic γ-ray spectra emitted during proton irradiation, a strong correlation was found between the delivered spread-out Bragg-peak (SOBP) dose distribution and the characteristic emission lines from the major elemental constituent atoms. To show that prompt γ-ray in particle therapy has recently gained remarkable interest, we finally cite the experimental work done by Styczynski et al with a proton beam irradiating a Lucite phantom and a lead collimated detector arranged orthogonally to the beam (Styczynski et al. 2009). They conclude that the results of the measurements are promising and indicate the feasibility of prompt gamma emission as a means of characterizing the proton beam range in-situ.

4.2.1 Collimated Prompt Gamma Camera

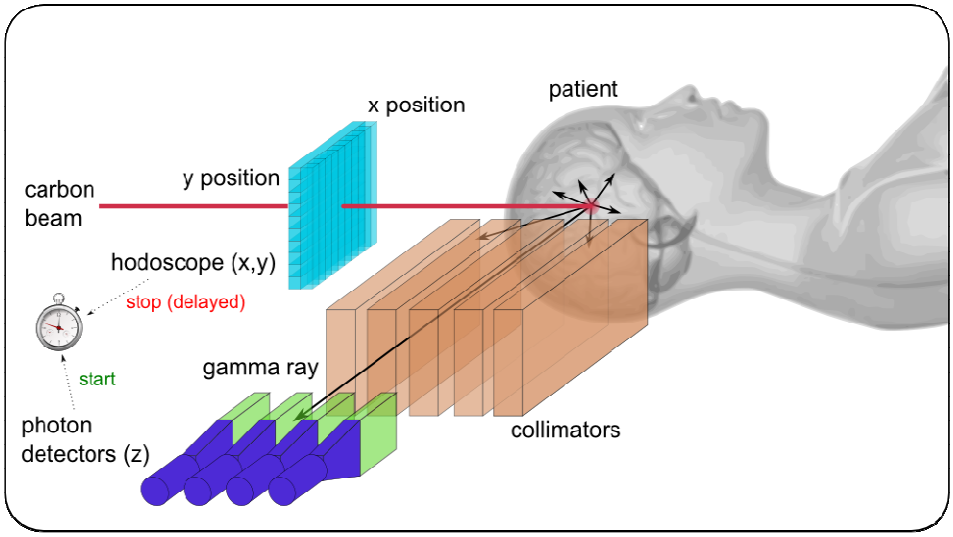

figure 4-7: Artistic scheme of the multi-collimated multi-detector prompt gamma camera. The hodoscope tags the ions in time and space coordinates. The collimator allows selecting only the photons emerging orthogonally to the beam. A series of stacked thin detectors are aligned to each collimator slit and provide snapshots of the longitudinal photon profile.

As already mentioned in section 0, ion range verification with PET cannot be performed during patient treatment mainly because of the time necessary to acquire the intrinsically delayed positron annihilation signals. Nevertheless, since the range is one of the most indicative factors of variation in dose delivery (Fiedler et al. 2010) and a tendency toward hypofractionation can be expected (Tsuji et al. 2005) it becomes highly desirable to have a tool able to detect range deviation during the patient treatment *in vivo* and in *real-time*. For such a purpose our group proposed to develop a device called collimated prompt gamma camera. Indeed, exploiting the detection of prompt γ-rays which are emitted within much less than a nanosecond after nuclear fragmentation, *real-time* information about dose delivered and Bragg-peak position becomes, in principle, possible. Moreover, as already mentioned in section 0 the correlation between prompt gamma emission and the primary ion path has been demonstrated both for protons (Min et al. 2006) and C-ions (E. Testa et al. 2008).

More specifically, the information about the photon source-point location, and, consequently, on the Bragg-peak position is provided by the collimated detection set-up that allows selecting only the prompt photons emerging orthogonally to the beam direction as sketched in figure 4-7. The use of TOF technique to discriminate the prompt photon component from a large background radiation mainly due to neutrons makes any further shielding around the detectors unnecessary. This means that a series of thin detectors, each of them aligned to a corresponding collimator slit, can be stacked as depicted in figure 4-7. Such a set-up allows stacking as many detectors to cover the entire longitudinal range of ions. The details of the spatial resolution that can be achieved with this multi-collimator and multi-detector set-up will be discussed

in detail in chapter 5 but it can already be stated that longitudinal resolutions of few millimetres could be achieved.

The monitoring of hadrontherapy obviously requires three dimensional (3D) dose cartography. Therefore not only the longitudinal range, but also precise information on the transverse position of the beam is required and it can be provided by a position sensitive hodoscope as depicted in figure 4-7. Assuming that the beam direction is provided by the hodoscope, it consequently implies the conjecture that particles will travel in straight lines from the hodoscope to their rest point. This is a reasonable assumption for C-ions but will require some further uncertainties evaluations for protons which have larger lateral scattering. Another major task of the beam hodoscope will be to provide the stop signal for the TOF measurement in case of non-pulsed beams. The details of the implication of the beam time-structure on the TOF measurements will be discussed in details in the next chapter. Nevertheless we can say that in case of synchrotrons conventionally used for particle therapy, the beam hodoscope must supply individual tag for each ion. Particle fluencies of 10^8 C-ions/s and up to 10^{10} proton/s are typically employed in therapy (Peters et al. 2008) and they can be expected to be measured, although with some technological challenge, with hodoscopes made of scintillating fibres (Achenbach et al. 2008) or synthetic diamond (Rebisz et al. 2006). Both kinds of hodoscopes are currently being developed in our laboratory and by collaborators from CEA-List Saclay France (Bergonzo et al. 2001).

Like for any other imaging technique, the major difficulty that must ultimately be overcome by the prompt gamma camera is the accumulation of enough counting statistics to obtain ion range profiles with spatial resolution of the order of the millimetre. In the next chapter, detailed considerations about the statistics which can be accumulated during a typical irradiation treatment will be discussed as well as possible solutions to increase it.

4.2.1 Compton Camera

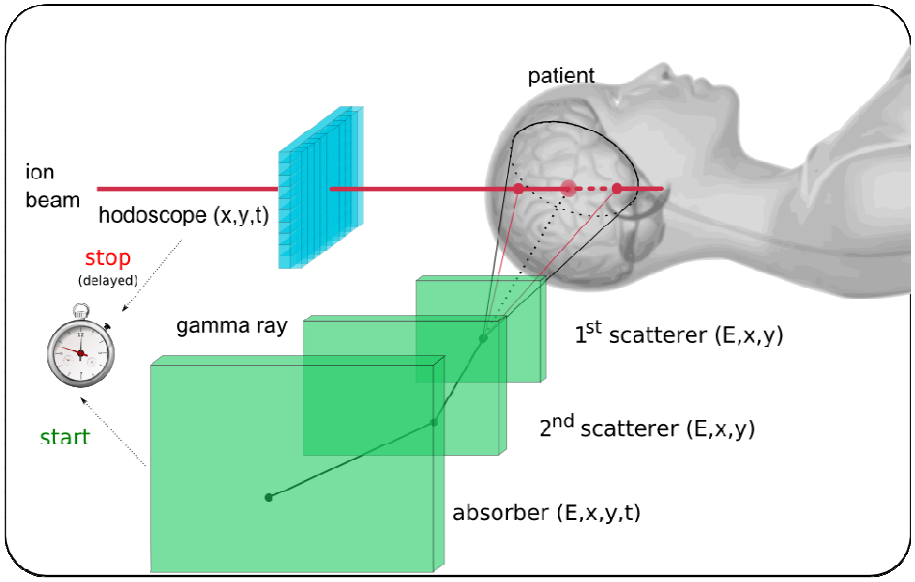

figure 4-8: Artistic scheme of a TOF-Compton camera setup. The hodoscope tags the ions in time and space coordinates. The Compton camera constituted by 2 scatter detectors and 1 absorber detector detects the prompt γ-rays emitted subsequently to the nuclear fragmentation processes induced in the patient body; figure from (M.-H. Richard et al. 2010).

Compton camera is another device proposed by our group for *in vivo* and in *real-time three dimensional* (3D) monitoring of the Bragg-peak position during a hadrontherapy treatment. Although it is not the subject of this thesis work, its main characteristics will be resumed in this section. The main advantage of Compton cameras over a collimated gamma-camera as the one presented in section 0, is the potentially increased efficiency of nearly two orders of magnitude due to the replacement of the performance-limiting absorbing collimator by an electronically-operating collimator (Dauvergne et al. 2009).

Traditionally, Compton cameras consist of one scatter detector and one absorber detector, and they are currently under development worldwide, for application mainly in gamma astronomy (Bloser et al. 2003) and medical imaging (Meier et al. 2002). The technique is based on a two-step process. First, a γ-ray undergoes a Compton scattering in the first (scatter) detector and second, the scattered photon is absorbed in the second (absorber) detector. Provided either photons are totally absorbed in the second detector, or their incident energy is known, it is possible, from the measurement of the deposited energy and the interaction position in both detectors, to reconstruct cones containing the incident trajectory of the incoming γ-ray. Basically, the photon emission points can be therefore reconstructed by intersecting all these cones.

For particle therapy application where the prompt gamma energy spectra is very broad and rises up to energies of several MeV, it would be difficult to envisage a complete absorption in the second detector, keeping the position information. Therefore, in a first study made by our group a solution with two

scatter detectors was investigated. This set-up allows making a direct analytic reconstruction of the direction of the incoming γ-ray (M.-H. Richard et al. 2010). The configuration of the detection system is reported in figure 4-8. The originality of the set-up relies on the use of a beam hodoscope, together with the Compton camera. The hodoscope is of the same kind as the one already discussed in section 0 and supplies the tagging of ions in time and space coordinates. For all the events in which a γ-ray undergoes a Compton scattering without energy escape (the recoil electron deposits all its energy in the scatter detector) in each scatter detector and an interaction in the absorber equations 4-1 to 4-5 can be written.

$$\cos(\theta_1) = 1 - m_e c^2 \left(\frac{1}{E_1} - \frac{1}{E_0} \right) \quad \textbf{4-1}$$

$$\cos(\theta_2) = 1 - m_e c^2 \left(\frac{1}{E_2} - \frac{1}{E_1} \right) \quad \textbf{4-2}$$

$$E_0 = \Delta E_1 + E_1 \quad \textbf{4-3}$$

$$E_1 = \Delta E_2 + E_2 \quad \textbf{4-4}$$

$$\cos(\theta_2) = \frac{(\mathbf{r_1} - \mathbf{r_2}) \cdot (\mathbf{r_2} - \mathbf{r_3})}{\|\mathbf{r_1} - \mathbf{r_2}\| \cdot \|\mathbf{r_2} - \mathbf{r_3}\|} \quad \textbf{4-5}$$

θ_1 and θ_2 are the photon scattering angles in the first and second scatter detectors. E_0, E_1 and E_2 are the photon energy value before it reaches the first scatter detector, the second one and the absorber respectively. $\mathbf{r_1}$, $\mathbf{r_2}$ and $\mathbf{r_3}$ are the interaction position vectors in the three detectors. ΔE_1 and ΔE_2 are the energies deposited in the two scatter detectors. The system composed of equations 4-1 to 4-5 is analytically solvable since it consists of five unknown quantities (θ_1, θ_2, E_0, E_1, E_2) and five measurable quantities ($\mathbf{r_1}$, $\mathbf{r_2}$, $\mathbf{r_3}$, ΔE_1, ΔE_2). It has to be noted that equation 4-1 and 4-2 do not take into account the Doppler broadening (due to the initial momentum distribution of the electrons) in the scatterers which introduces an error in the reconstruction.

Once θ_1 is determined, it is possible to reconstruct a cone on which lies the trajectory of the incident photon. The possible prompt gamma emission points are then given by the intersection of the reconstructed cone and the ion trajectory provided by the hodoscope. Nevertheless these reconstructed prompt gamma emission points may be affected by several uncertainties mainly given by the limited spatial resolution of the hodoscope, the lateral scattering of ions and the interaction of secondary particles in the detectors. Specific energy selections on the detected events are therefore necessary to eliminate wrongly reconstructed γ-rays emission points. Moreover reconstruction algorithms must be very fast since the information about the detected interaction points has to be processed in real-time.

Investigations on the influence of various parameters such as the photon energy and the inter-detector distances on the achievable spatial resolution and

detection efficiency with a photon source point, have been initiated in a recent work by our group (M-H. Richard 2009). The main purpose of this study was to develop a Monte Carlo simulation tool able to provide the main guidelines for the design of a Compton camera, namely the detectors geometrical and energy-resolution requirements (M.-H. Richard et al. 2010). The double scattering configuration resulted to be promising concerning the feasibility of the *real time* monitoring in ion beam therapy. Nevertheless the still limited counting statistics imposed to adopt a stack of Si(Li) detectors (Walenta et al. 2005) as scatterers of the Compton camera prototype which is currently being developed in our laboratory and which is supposed to have an efficiency increased by one or two orders of magnitude compared to the double scattering camera presented above.

4.3 Interaction Vertex Imaging (IVI)

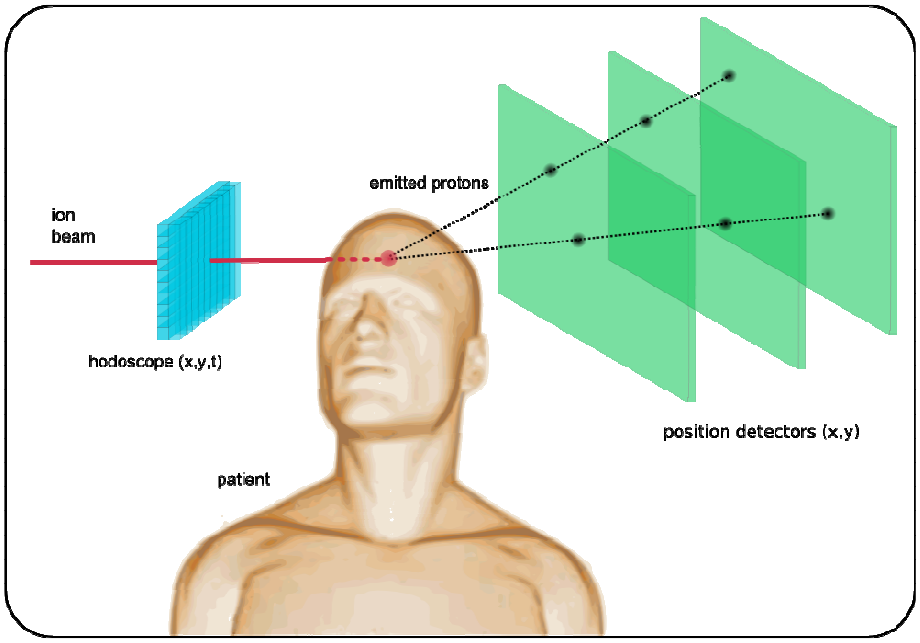

figure 4-9: Artistic scheme of the interaction vertex imaging (IVI) system. The hodoscope tags the ions in time and space coordinates. In single-track vertexing, the vertex is reconstructed as the intersection of the particle trajectory and the beam direction provided by the hodoscope. In multi-track vertexing, the vertex is reconstructed by the intersection of 2 or more particle trajectories arising from the same fragmentation point.

All the methods proposed so far for hadrontherapy monitoring and ion range verification are based on the detection of photons arisen either from positron annihilation by emitters created during ion beam fragmentation (PET), or from prompt gamma de-excitation of nuclear fragments (collimated and Compton prompt gamma cameras). An alternative technique, based on the detection of energetic charged particles emerging from the patient, which are generated in the nuclear interaction between the incoming ions and target molecules, is currently under investigation by a collaboration between our group and TERA foundation (Henriquet 2010).

This new technique called interaction vertex imaging (IVI) is, in principle, similar to vertex identification problems in fixed target particle physics experiments. The scheme of IVI system is shown in figure 4-9 and it is based on the reconstruction of the trajectories of the emerging particles which are then extrapolated back to their production point (Dauvergne et al. 2009). Indeed, as for PET and prompt gamma imaging techniques, the position of the fragmentation points are expected to be correlated with the ion range, and the amount of emerging charged particles could be, in principle, correlated to the dose. The main advantage of IVI compared to systems based on prompt photon detection is the counting statistic potentially achievable. Indeed, for example, the amount of protons emitted at 10° with respect to the beam direction has been measured in about $6x10^{-5}$ p ion^{-1} msr^{-1} for ^{12}C at 95 MeV/u (Braunn et al. 2010) and $5x10^{-4}$ p ion^{-1} msr^{-1} for ^{12}C at 200 MeV/u (Gunzert-Marx et al. 2008). These values are about 2-3 orders of magnitude higher than the ~$5x10^{-7}$ prompt-γ ion^{-1} msr^{-1} measured orthogonally to the beam direction (M. Testa et al. 2010) and therefore they make IVI a potentially attractive technique.

The vertex reconstruction can be done with two different techniques based on the particle multiplicity arising from each fragmentation vertex. In the simplest form, also named single-track vertexing, the particle trajectory is obtained by linear fit of the interaction points in the pixilated detectors and the vertex is reconstructed as the intersection of this line with the beam direction provided by the hodoscope. Therefore, in this case, all the events with one emerging particle per fragmentation vertex (multiplicity = 1) may potentially be reconstructed. Nevertheless, this reconstruction technique is intrinsically limited to primary fragmentation laying on the primary beam direction provided by the hodoscope. The reconstruction uncertainties will first depend on the spatial resolution of the hodoscope and on the lateral scattering of the primary ions. Second, the emerging angle of the particles will affect the final resolution of the system and although forward emitted particles are the most abundant, they would be at the same time the most imprecisely reconstructed. Indeed the geometrical uncertainties on the reconstructed vertex increases with decreasing the angle between the interpolated line from the particle interaction points and the beam direction. Moreover, forward emitted particles are usually the most energetic and therefore less sensitive to multiple scattering which represents another limitation of the method: one has to find the best compromise between angular accuracy (best at large observation angle) and low angular straggling (preferably with higher energetic particles at forward angles). Moreover, the angular position of the particle detectors must be chosen as a trade off between counting statistics and spatial resolution of the reconstructed vertexes. For such a purpose Monte Carlo simulations are currently being performed (Henriquet 2010).

A second approach for vertex reconstruction, also called multi-track vertexing, is based on the reconstruction of events in which, for each fragmentation vertex, two or more particles are emitted (multiplicity>1). In practice, a multiplicity equal to two will be considered as the most probable scenario. In this case the vertex would be identified by the intersection of the two particle trajectories

interpolated by linear fit of the interaction points in the pixilated detectors as shown in figure 4-9. With multi-track vertexing, the beam direction provided by the hodoscope is, in principle, accessory although it could anyway simplify the reconstruction algorithm and be used for timing. To determine the amount of nuclear fragmentation reaction leading to particle multiplicity higher than one, a series of experiments are currently being performed by our group at the GANIL facility (Henriquet 2010).

5 Physical measurements of the prompt radiation originated from ion fragmentation

A series of test measurements to characterize the scintillation detector performances have been carried out before performing the experiments with accelerated ion beams. In particular the evaluation of the scintillators background energy spectra due to their internal radioactivity along with the assessment of energy resolution and photon detection efficiency are presented in the following for all the scintillators used in the experiments with accelerated C-ions. Moreover, some test measurements with neutron sources have been performed to evaluate the pulse shape discrimination (PSD) properties of our scintillators. PSD was indeed one of the techniques that we envisaged to apply in this work to discriminate the prompt photons from the large neutron background that is produced during ion fragmentation.

5.1 Properties of scintillation detectors

Scintillation detectors exploit the fact that some materials, when struck by ionizing radiations, emit a flash of light, *i.e.* a scintillation, which is a property of radioluminescence. Radioluminescence occurs when an incoming radiation particle collides with an atom or molecule, exciting an orbital electron – or an electron from the valence band of the solid - to a higher energy level. The electron then returns to its ground energy level by emitting the extra energy as a photon of light. When coupled to an amplifying device such as a photomultiplier, the scintillation photons can be converted into electrical pulses which can then be electronically analyzed or counted to give information concerning the incident radiation. The main requirements a scintillator material has to satisfy are *i)* high efficiency for conversion of exciting energy to fluorescent radiation *ii)* transparency to its own fluorescent radiation so as to allow transmission of the light *iii)* light emission in a spectral range consistent with the spectral response of existing photomultipliers *iv)* a short decay constant (τ). Scintillator materials are usually classified as organic and inorganic.

Organic scintillators are aromatic hydrocarbon compounds containing linked or condensed benzene-ring structures. Their most distinguish feature is a very rapid decay time of the order of a few nanoseconds or less and they are mainly used for charged particle detection. In contrast, their efficiency for gamma detection is not optimal because of their low density and low light yield which is of the order of 10^4 photons/MeV or even less (Solevi P. 2007). Scintillation light in these compounds arises from transitions made by the free valence electrons of the organic molecules. These delocalized electrons are not associated with any particular atom in the molecule and occupy what are known as π-molecular orbitals. Because of the molecular nature of luminescence in these materials, organic scintillator can be used in many physical forms without losing their scintillating properties. As detectors, they

are used in form of pure crystals and as mixture of one or more compounds in liquid and solid solutions.

Inorganic scintillators can be impurity-activated alkali halides crystals like NaI(Tl), CsI(Tl), $LaBr_3$(Ce), oxides doped with rare earth elements like LYSO ($LuYSiO_5$:Ce) or self-activated non alkali materials like BaF_2 or BGO (Van Eijk 2001). The advantage of inorganic crystals over organic scintillators lies in their greater stopping power due to their higher density and higher atomic number. Among all the scintillators they also have some of the highest light output (see Table 5-1), which results in better energy resolution. This makes them suitable for detection of gamma rays and in the last years there has been a positive trend towards the development of faster, more luminous and denser scintillator materials (K. W. Krämer et al. 2006). The luminescence process occurring in inorganic scintillators are of two types according to the time scale in which light emission takes place: fluorescence, if the time constant is shorter than 10^{-8} s, and phosphorescence or afterglow, with emission time larger than 10^{-8} s and for some materials as large as several hours (Solevi P. 2007).

Scintillator	Density [g/cm^3]	Decay time [ns]	Light yield [N_{ph}/keV]	ΔE/E(662 keV) (% FWHM)
NaI(Tl)	3.67	230	41	5.6
BaF_2	4.89	0.7 fast 620 slow	2 fast 8.2 slow	10
LYSO ($Lu_{1.8}Y_{0.2}SiO_5$:Ce)	7.1	41	33	7-9
$LaBr_3$:Ce	5.3	35	61	2.9
BC501	0.87	3.2	14	-

Table 5-1: Comparison of scintillator properties. Values adapted from (P. Crespo et al. 2007).

It is well known, that for both organic and inorganic scintillators, the amount of fluorescence light emitted is not directly proportional to the energy deposited by the ionizing particle. Indeed the response of the scintillator is a complex function of not only energy but the type of particle and its specific ionization. Experimentally it was found that generally, the amount of scintillation light produced by particles of the same energy decreases for heavier particles. The first semi-empirical model to describe such a behavior was proposed by Birks (Birks 1951). Birks' theory relates the light output per unit length (dL/dx) to the specific energy loss (dE/dx) according to equation 5-1. It is assumed that the nonlinearity between emitted light and deposited energy is due to quenching interactions between the excited molecules along the path of incident particle. Therefore, quenching interactions drain energy that would otherwise go into luminescence mainly through phonons and heat production. Since a higher ionizing power produces a higher density of excited molecules, more

quenching will take place for these particles and therefore the light production will be lower.

$$\frac{dL}{dx} = \frac{A\frac{dE}{dx}}{1 + kB\frac{dE}{dx}} \qquad \textbf{5-1}$$

In equation 5-1, A is the absolute scintillation efficiency and kB is a parameter relating the ionization density to dE/dx. In practice, kB is obtained by fitting Birks' formula to the experimental data and tabulated values of kB can be found in the literature as function of the scintillator material, particle type and energy (Leo 1994).

As reported in Table 5-1, the number of scintillation photons N_{ph} emitted when an amount of energy E is absorbed in a scintillator is given by equation 5-2 (Lempicki et al. 1993).

$$N_{ph} = N_{e-h}SQ = \frac{E}{\beta E_{gap}}SQ \qquad \textbf{5-2}$$

$N_{e\text{-}h}$ represents the number of thermalized electron-hole pairs produced in the interaction process. E_{gap} is the band-gap energy between valence and conductive band and β is a parameter which indicates the average energy required to produce one thermalized electron-hole pair: $E_{e\text{-}h}=\beta E_{gap}$, β ~2-3 (Van Eijk 2001). S is the transport/transfer efficiency of the e-h pairs to luminescence centers (LC) and Q is the quantum efficiency of the LC, i.e., the efficiency for photon emission once a LC is excited.

5.1.1 Characteristics of BaF_2 – NaI(Tl) – LYSO – BC501 scintillators

In this work four types of detectors have been used: BaF_2, NaI(Tl), LYSO, BC501. Their main characteristics are reported in Table 5-1 and the specific dimensions are reported in Table 5-2. NaI(Tl), BaF_2 and LYSO($Lu_{1.8}Y_{0.2}SiO_5$:Ce) are commonly employed γ-detectors made of high Z elements while BC501 ®Saint-Gobain Crystal is a liquid organic scintillator particularly suited for neutron detection.

Scintillator	Dimensions
NaI(Tl) 2 inches	Cylindrical Ø 5 cm thickness: 5 cm
NaI(Tl) 3 inches	Cylindrical Ø 7.5 cm thickness: 7.5 cm
BaF_2	Hexagonal Ø 9 cm thickness: 14 cm
BC501 ®Saint-Gobain Crystal	Cylindrical Ø 5 cm thickness: 15 cm
LYSO pixel	4x48x22 mm
LYSO medium	3x50x40 mm
LYSO large	5x50x40 mm

Table 5-2: Dimensions of the detectors used in this work for γ and neutron measurements.

In figure 5-1 are reported the calibration energy spectra of the four detectors described above obtained with ^{137}Cs and ^{60}Co radioactive sources. NaI(Tl) has

the best energy resolution and the full width at half maximum (FWHM) of the 662 keV γ-peak from the ^{137}Cs source is in complete agreement with the values which can be found in the literature and that are reported in Table 5-1. Again, compared to literature values of Table 5-1, a slightly worse energy resolution is found for the BaF_2 detector while our LYSO detectors present poor energy resolution. This is mainly due to the limited volume of the scintillator and a non optimal coupling with photomultiplier tube (PMT). For sake of precision we can mention that FWHM of 15% at 662 keV can be found when the LYSO detector is calibrated with ^{137}Cs alone and therefore no Compton interaction from the ^{60}Co source are superimposed to 662 keV γ-peak. This same effect is of minor relevance for NaI(Tl) and BaF_2 where the majority of the photons from the source undergo total absorption due to the big scintillator volume. As already mentioned, BC501 is a liquid, low-density, low-Z organic scintillator intended for neutron detection and therefore its efficiency for γ-detection is inevitably poor as shown in figure 5-1 where Compton-front structures rather than photoelectric absorption peaks are observed for both ^{137}Cs and ^{60}Co sources.

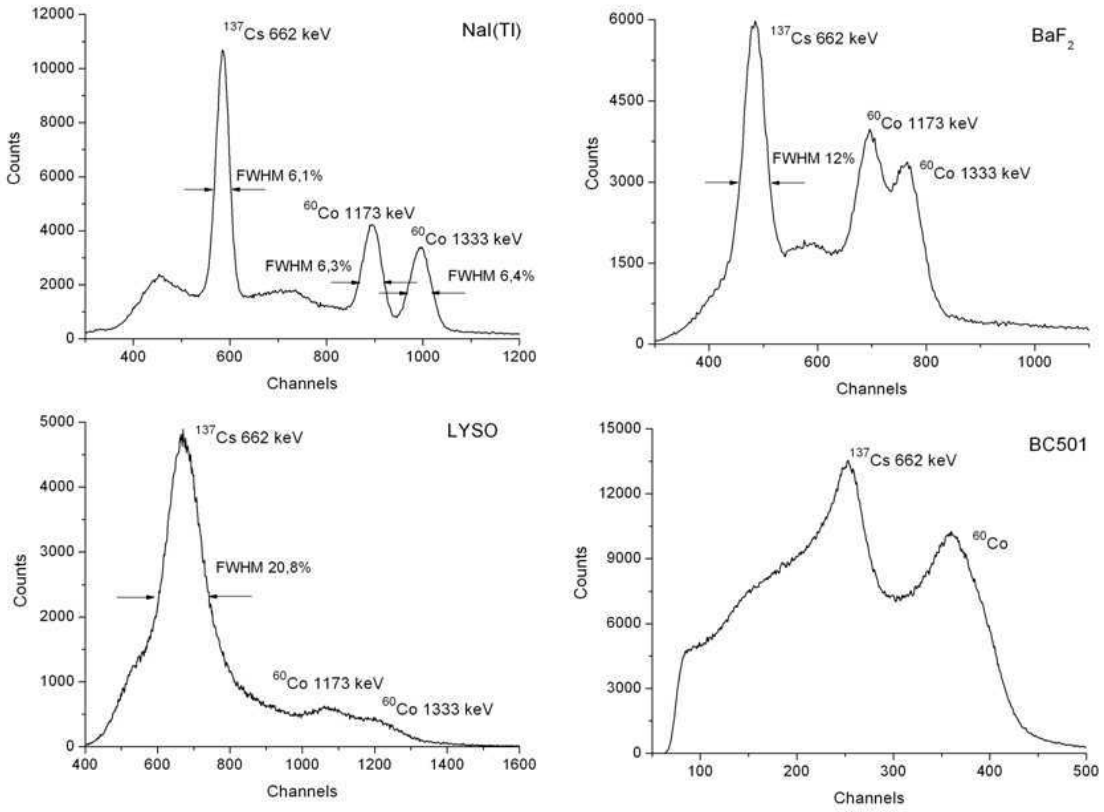

figure 5-1: Calibration energy spectra for NaI(Tl) 3 inches, BaF_2, LYSO medium and BC501 detectors with ^{137}Cs and ^{60}Co radioactive sources at the same time.

One of the main characteristics of both BaF_2 and LYSO scintillators is their internal radioactivity respectively due to ^{226}Ra and ^{176}Lu impurities. Considering BaF_2, the ^{226}Ra radioactive disintegration chain (Wisshak & Käppeler 1984) is reported below and the characteristic energies of the four α

disintegrations are clearly visible in the energy spectra reported on the left part of figure 5-3.

$$^{226}Ra \xrightarrow{\alpha:4.87MeV} {}^{222}Rn \xrightarrow{\alpha:5.59MeV} {}^{218}Po \xrightarrow{\alpha:6.11MeV} {}^{214}Pb$$

$$^{214}Pb \xrightarrow{\beta^-} {}^{214}Bi \xrightarrow{\beta^-} {}^{214}Po \xrightarrow{\alpha:7.83MeV} {}^{210}Pb$$

LYSO is a lutetium-based scintillator which contains the radioactive isotope ^{176}Lu which is a naturally occurring beta emitter *(K_{β}^{max}=1.2 MeV)*. ^{176}Lu beta decays into ^{176}Hf 99.66% of the time to the 597 keV excited state (Firestone et al. 1996). This state decays with a 3 γ-ray cascade of 307 keV, 202 keV and 88 keV as depicted in figure 5-2.

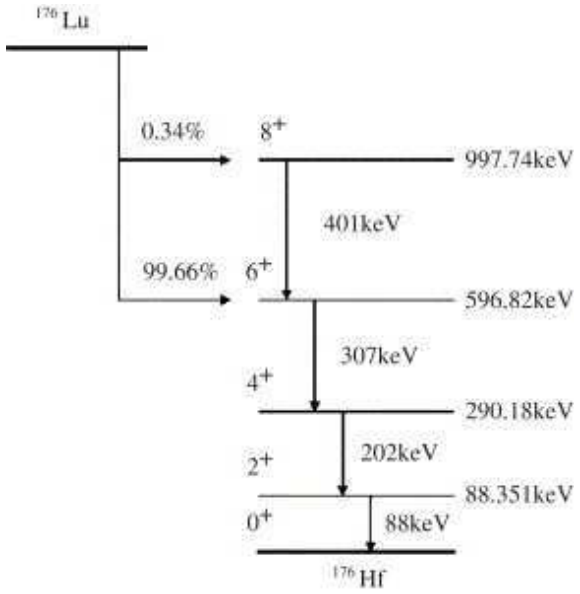

figure 5-2: Decay scheme of ^{176}Lu from (Firestone et al. 1996).

Two structures, corresponding respectively to the 597 keV excited state and to the 290 keV state (202+88 keV) can be identified in the background energy spectrum reported in the right part of figure 5-3.

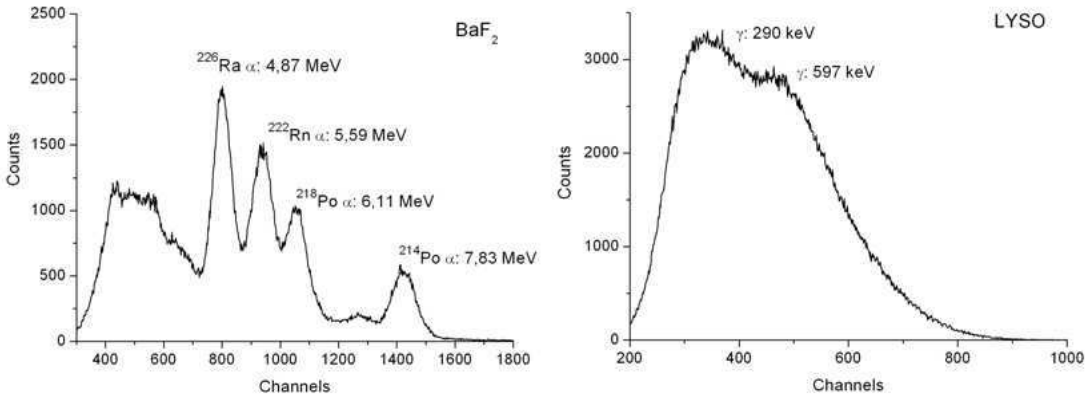

figure 5-3: Background spectra due to the internal radioactivity of BaF_2 and LYSO scintillators. For the BaF_2 detector the ^{226}Ra measured activity is about 350 Bq. For LYSO, ^{176}Lu measured activity is about 40 Bq/g.

The detection efficiency for BaF_2 and BC501 scintillators has been simulated with Geant4 Monte Carlo code (Agostinelli et al. 2003) for monoenergetic pencil

beams of photons and is reported in figure 5-4. A more detailed description of the simulation code will be given in the next chapter. The detectors were modeled to accurately reproduce the scintillators shape and dimensions. Each pencil beam consisted of $5x10^4$ photons parallel oriented to the detector axis and hitting the center of the front side of the scintillator. As expected, the photon detection efficiency is higher for BaF_2 than for BC501 detector. Moreover, BaF_2 efficiency is rather constant in the photon energy range from 0.1 to 10 MeV and a slight increase in the efficiency is observed for E>6MeV due to the increase of pair production cross sections. On the other hand, for few MeV energy photons, BC501 efficiency decreases exponentially with the increase of the photon energy since for such low Z-materials the decrease in the Compton interaction cross section is dominant and pair production cross section becomes influent only for E>60 MeV.

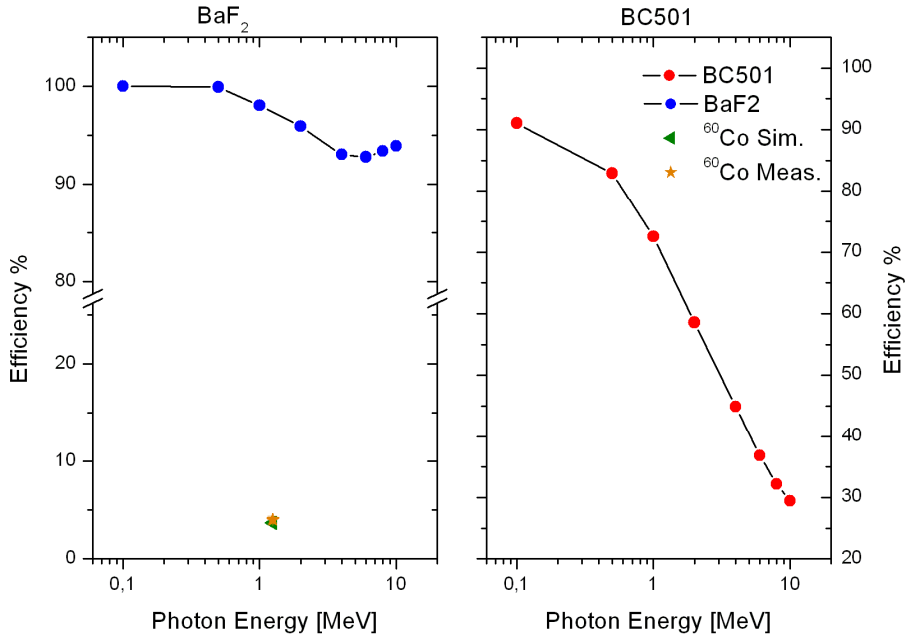

figure 5-4: Intrinsic efficiency of BaF_2 (left) and BC501 (right) detectors to monoenergetic pencil beams of photons obtained by Geant4 simulations. The measured detection efficiency of BaF_2 (left) for a 24 kBq ^{60}Co radioactive source placed at 10 cm (^{60}Co Meas.) has been compared to the source detection efficiency (^{60}Co Sim.) obtained by simulation.

To validate the Geant4 simulations, the detection efficiency for a 24 kBq ^{60}Co radioactive source was measured with the BaF_2 detector and compared to the efficiency obtained by simulation. The source was placed at 10 cm from the front side of BaF_2 scintillator to avoid photon pile-up in the detector and the ^{60}Co was modeled in the simulations as an isotropic source of photons with energy of 1.25 MeV. An energy selection on photons depositing more than 100 keV in the scintillator allowed disregarding the dependence on the detection efficiency on the electronic threshold. Therefore, after dead time correction the measured detection efficiency of 4% was compared with the respective simulation efficiency of 3.7% and found in good agreement as reported in figure 5-4.

5.1.2 Pulse shape discrimination (PSD) for BaF_2 and BC501 scintillators

The basic idea of pulse shape discrimination (PSD) relies on the fact that information about the type of particle interacting with a scintillator is carried in the pulse shape of the signal which is generated by the detector. Historically PSD is associated with scintillation detectors (Winyard et al. 1971) although it has also been applied to semiconducting detectors for particle identification (Ammerlaan et al. 1963) and improvement in energy resolution (Jones & Woollam 1975). Nevertheless, in this work we will only deal with PSD applied to organic and inorganic scintillators.

In principle, all the scintillators which have at least one fast and one slow light decay component (τ), as for example CsI(Tl), CeF_3, BaF_2 and several organic liquid scintillators, are eligible for PSD. Indeed, fast and slow components arise from the de-excitation of states which are populated differently according to the specific energy loss *(dE/dx)* of the interacting radiation. As sketched in the left part of figure 5-5, highly ionizing radiations (like neutrons) excite more likely scintillator states which have longer de-excitation times, and therefore longer duration signals, compared to low ionizing radiations (like photons). Indeed photons induce preferentially dipolar transitions toward excited states with very short lifetime, while high LET particles produce multi-excitations which could lead to metastable states.

Two methods are usually employed for PSD: the zero-crossing and the charge comparison (Wolski et al. 1995). In the zero-crossing method the anode signal of the scintillator is firstly integrated then differentiated and the time at which the differentiated signal crosses the base line (zero crossing) is representative of the kind of particle interacting with the scintillator (Barnabà et al. 1998). The main drawback of this method is that it requires dedicated electronic modules specifically designed for pulse duration and decay constant of each particular scintillating material. Therefore, in our work, we adopted the more versatile, although underachieving at low energies (< 300 keV), charge comparison method (Normand et al. 2002). It consists of integrating the anode signal of the scintillator over gates of different duration with a charge integrating analog to digital converter (QDC) module. The principle of this method can be easily understood by geometrical considerations over the integrated charges subtended to the scintillator signals. As already mentioned, the more ionizing the particle, the longer the signal tail, due to the long life of the metastable energy states. Therefore, considering for example the case of BaF_2 represented in the upper part of figure 5-5, the integration over a short (50 ns) and a long (500 ns) gate (Gunzert-Marx 2004) of a γ signal will lead to almost the same amount of charge for both gates. In other words, for γ-rays, if we call $Q_{\gamma\text{-}S}$ the charge integrated over the short gate and $Q_{\gamma\text{-}L}$ the charge integrated over the long gate, the ratio $Q_{\gamma\text{-}S}/Q_{\gamma\text{-}L}\approx 1$. This will not be the case for a neutron signal, in which, following the same notation, $Q_{n\text{-}S}/Q_{n\text{-}L}<1$. This difference in the ratio of the integrated charges can be visualized on the 2D PSD spectra reported in the right part of figure 5-5. Indeed, if we plot, for each signal, the amount of charge integrated over the short *vs* long gate, all neutron interactions will lay along a line whose slope is given by $Q_{n\text{-}S}/Q_{n\text{-}L}$ and which will be necessarily below the γ

interaction line with slope $Q_{\gamma\text{-}S}/Q_{\gamma\text{-}L}$. Again, this fact can be understood by considering that for the same amount of charge integrated over the long gate, the charge integrated over the short gate will necessarily be higher for a γ than for neutron signal. Analogous considerations can be done for the integration gates chosen to perform PSD with the BC501 scintillator (Barnabà et al. 1998). In this case, we used two gates of the same duration (300 ns) but shifted one respect to the other (35 ns) named total and delayed gate respectively. Therefore, in the 2D PSD spectrum, following the same notation introduced above, $Q_{n\text{-}D}/Q_{n\text{-}T} > Q_{\gamma\text{-}D}/Q_{\gamma\text{-}T}$ and thus the neutron-line will lay above the γ interaction line. The choice of adopting two different pairs of integration gates for BaF_2 and BC501 detectors was done according to the results found in the literature and which turned out to lead to the best PSD performance for each type of scintillator.

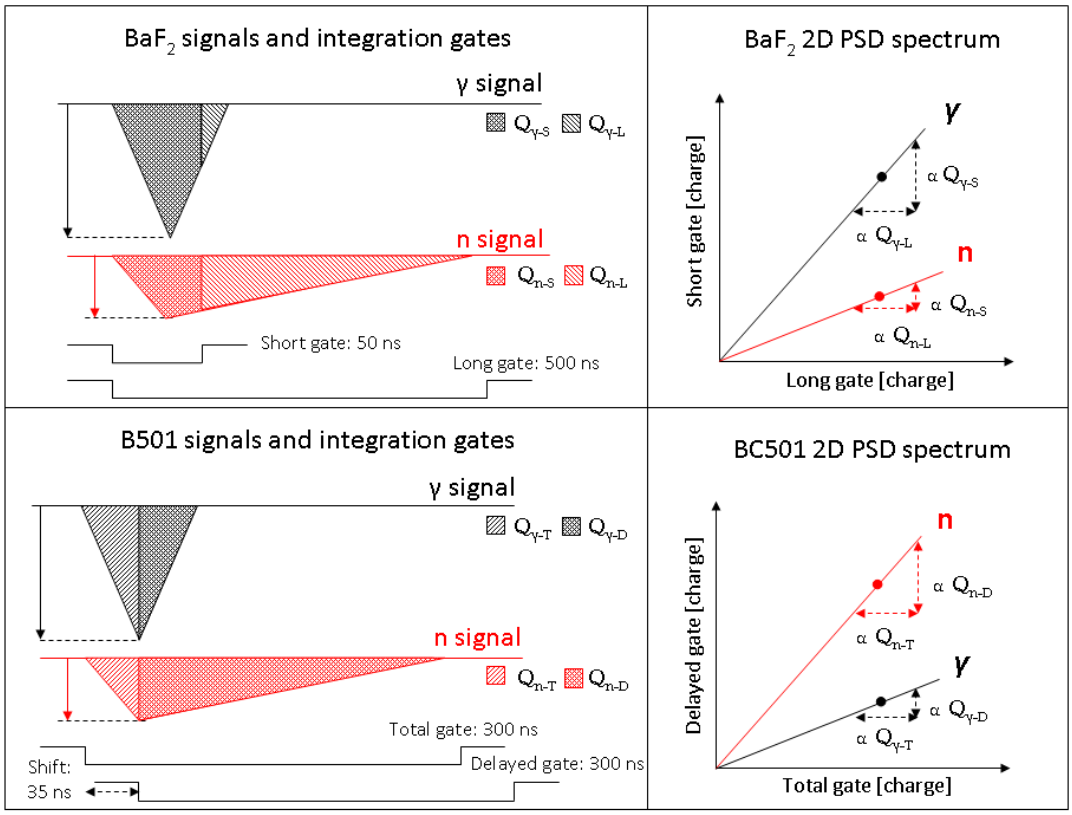

figure 5-5: Scheme of Pulse Shape Discrimination (PSD) principle. Left: γ (black) and neutron (red) signals integrated over different gates. Right: scheme of two dimensional PSD spectra showing the relative position of γ (black) and neutron (red) lines according to the specific choice of integration gates. $Q_{\gamma\text{-}S}$ represents the charge (Q) of the γ signal integrated over the short gate (S), the other notations follow accordingly.

As reported in the previous paragraph BaF_2 crystal is slightly radioactive due to ^{226}Ra impurities which decay through a chain of α and β^- disintegrations. These two forms of internal radioactivity can be distinguished through PSD and are clearly identifiable in the 2D PSD spectrum presented on the left part of figure 5-6 where two series of points (stripes) corresponding to β^- and γ *vs* α interactions are well differentiated. By definition photon and electron interactions cannot be distinguished since, physically, a photon interacts setting

in motion electrons- and in most cases once at a time- of the detector. The only difference could come from the interaction point in a large volume detector: the photon interacts in a random location of the detector, whereas an electron interacts continuously along its trajectory, starting from the entrance face of the detector. Therefore the charge collection time may differ slightly for geometrical reasons. Furthermore, as already explained above, in a 2D PSD spectra where we plot the integrated charges over short *vs* long gates, the higher the ionization density of the particle, the lower the ratio Q_S/Q_L (where Q_S and Q_L represent the charge integrated over the short- and long gate respectively). Therefore the signals due to α interactions will produce a set of points which will lay down the β^- and γ stripes. In the right part of figure 5-6 it is shown an energy spectrum of BaF_2 internal radioactivity on which we performed a differentiation on the type of particles which contribute to the spectrum. The four α peaks, already shown in figure 5-3, could thus be distinguished from the electrons produced in the β^- decay and a further peak could be identified and attributed to the 1.46 MeV γ-ray emitted by ^{40}K impurities (Wisshak & Käppeler 1984).

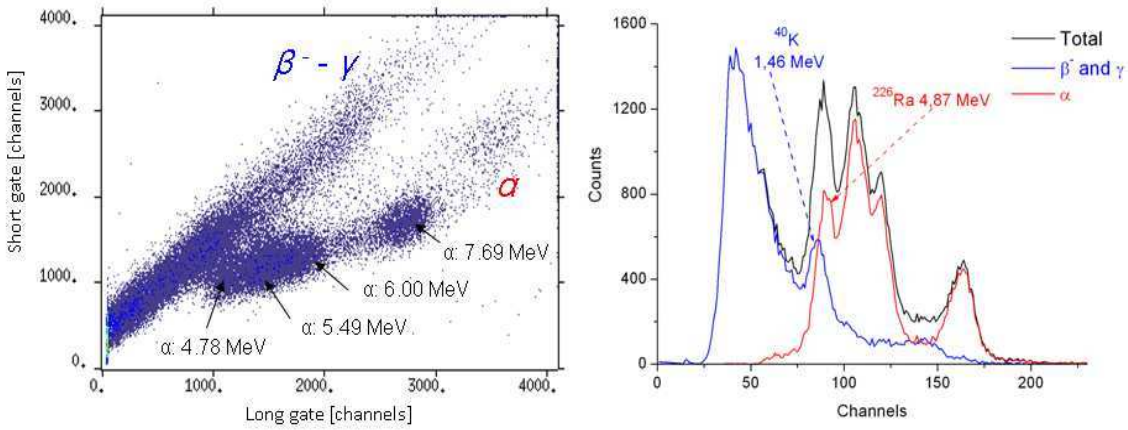

figure 5-6: PSD applied to the internal radioactivity of BaF_2 scintillator. Left: 2D PSD spectrum in which signals arising by photon and alpha are clearly distinguishable as two separate sets of points. Right: internal background radioactivity energy spectra (black curve) in which a selection is operated on signals arising from β^- decay and γ interactions (blue curve) and from α decay interaction (red curve).

5.1.2.1 PSD test measurements with a ^{241}Am-Be source

In order to assess the PSD properties for neutron-gamma discrimination of BaF_2 and BC501 scintillators some test measurements have been performed with a 160 MBq ^{241}Am-Be source. The ^{241}Am-Be is a radioactive source in which neutrons with energies up to 10 MeV (Lorch 1973) are produced through (α, n) and (γ, n) nuclear reactions. ^{241}Am is indeed a natural α-emitter and beryllium is the target material undergoing the following reactions which lead to the production of free neutrons and γ-rays from nuclear de-excitation:

$$^{241}Am \rightarrow {}^{237}Np + \alpha$$

$$\alpha + {}^{9}Be \rightarrow {}^{13}C^{*} \rightarrow \begin{cases} {}^{12}C^{*} + n; & {}^{12}C^{*} \rightarrow {}^{12}C + \gamma(4.44MeV) \\ {}^{8}Be + \alpha + n \\ 3\alpha + n \end{cases}$$

$$^{9}Be + \gamma \rightarrow {}^{8}Be + n$$

The reaction cross sections of reactions reported above depend in a complex way on the α energy (Geiger & Van der Zwan 1975) therefore no easy estimation of the branching fractions is possible. With ^{241}Am as α-source, a neutron yield of about 70 neutrons per 10^6 α-particle is generally obtained (Leo 1994).

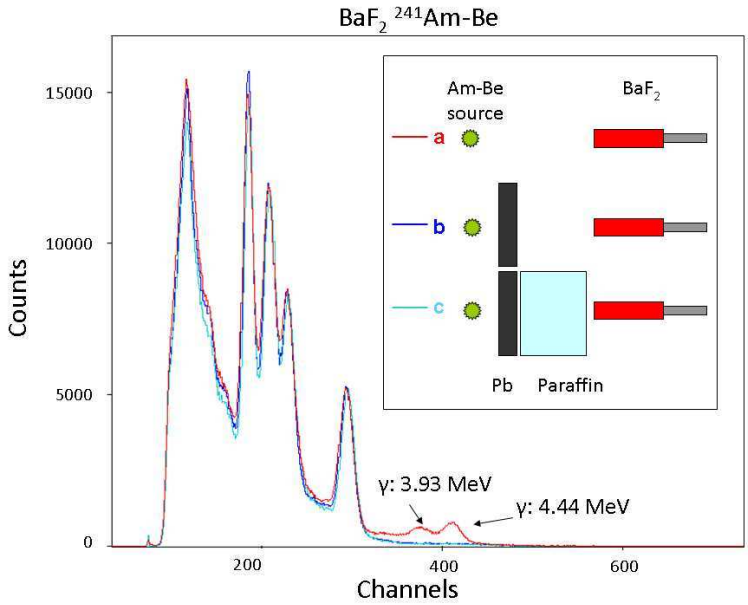

figure 5-7: Energy spectra of a "low activity" (160 MBq) Am-Be source obtained with BaF_2 detector. As reported in the inset, the measurements have been performed with three different configurations: no shielding (red curve), 10 cm lead shielding (dark blue curve), 10 cm lead and 40 cm paraffin shielding (light blue curve).

In figure 5-7 is shown an energy spectra of the ^{241}Am-Be measured with BaF_2 detector. As can be noticed the spectrum is completely overwhelmed by the β- structures and the four α-peaks due to the internal radioactivity of BaF_2 presented in figure 5-6. Indeed, the ^{241}Am-Be source activity of 160 MBq leads to a neutron yield of ~10^4 neutron/s emitted in 4π sr which, taking into account the detection efficiency and solid angle, is of the same order of magnitude as the ~350 Bq internal activity of the BaF_2 detector. The only contribution from the ^{241}Am-Be to the spectrum is given by the γ-peak at 4.44 MeV corresponding to the $^{12}C^{*}$ excited state and the single 0.511 MeV γ-escape peak at 3.93 MeV (Mowlavi & Koohi-Fayegh 2004). As represented in the inset of figure 5-7, in order to spotlight the neutron contribution to the energy spectrum two additional measurements have been performed with a 10 cm lead shielding and 40 cm paraffin shielding interposed between the source and the BaF_2 detector. The paraffin was supposed to diffuse the neutrons that could therefore be

visualized by spectra subtraction with the measurement performed with lead shielding only. Nevertheless no evidence of a recognizable ^{241}Am-Be neutron spectrum as reported in the literature (Park 2003) could be achieved while, in contrast, the lead shielding demonstrated to be effective in suppressing the γ-peaks from the spectrum.

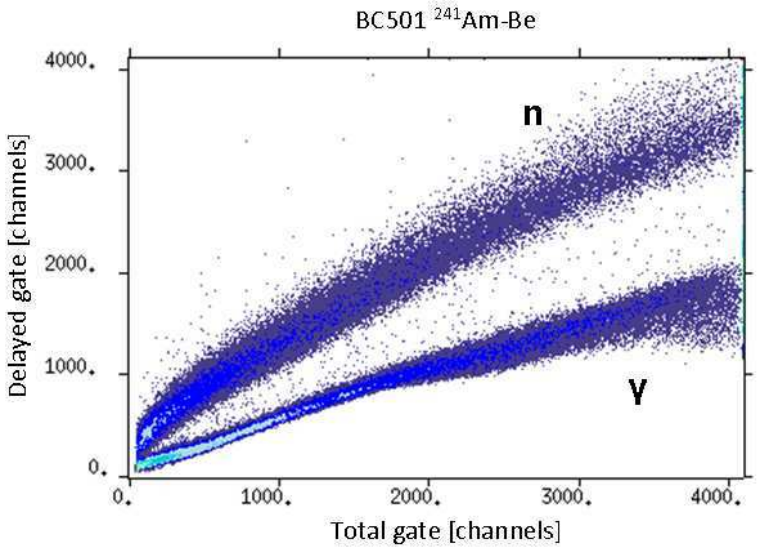

figure 5-8: 2D PSD spectrum of Am-Be source obtained with BC501 detector. Two different aligned sets of points corresponding to neutron and γ interactions are clearly distinguishable.

The main goal of our test with the ^{241}Am-Be source was to identify neutron interactions on the 2D PSD spectra. This turned out to be unachievable with BaF_2 mainly because of the already mentioned overwhelming signal from internal radioactivity. Nevertheless, dedicated experiments on pulse shape analysis of signals from BaF_2 failed to observe pure neutron signals with a neutron beam arising from ^{9}Be(p,n)^{9}B reaction (Marrone et al. 2006). Indeed for neutron energies below 5 MeV inelastic scattering is by far the most probable interaction on both fluorine and barium atoms which finally most frequently de-excite through photon emission.

On the contrary, neutron identification resulted to be straightforward with BC501 detector as represented in figure 5-8. BC501 presents no internal radioactivity and therefore the background signal is in practice inexistent. Moreover, the detection efficiency of neutrons below 10 MeV is higher for BC501 scintillator than BaF_2 (Gunzert-Marx et al. 2005). Indeed, on the 2D PSD spectrum of figure 5-7 obtained with BC501, two aligned sets of points corresponding to neutrons (up) and γ (down) are clearly distinguishable and denote the good PSD performances of BC501.

5.1.2.2 PSD test measurements with 14 MeV neutrons

In order to further assess the PSD properties for neutron-gamma discrimination of BaF_2 and BC501 scintillators a series of test measurements have been performed with 14 MeV neutrons provided by a SODERN "GENIE 26" sealed

neutron tube generator (Rivaton & Arnold 2008) available at the Laboratoire de Physique Corpusculaire (LPC), Clermont-Ferrand (France).

Monoenergetic neutrons of 14 MeV kinetic energy were produced through the nuclear fusion reaction reported below

$$^{2}H + {}^{3}H \rightarrow \alpha + n$$

The maximum neutron flux which could be generated was ~2x10^{8} n/s isotropically emitted in 4π sr, while the α-particles produced in the reaction have a kinetic energy of 3.5 MeV which cannot enable their escape from the tube generator. Both BaF_2 and BC501 detectors were placed with their front side at about 10 cm from the neutron production point.

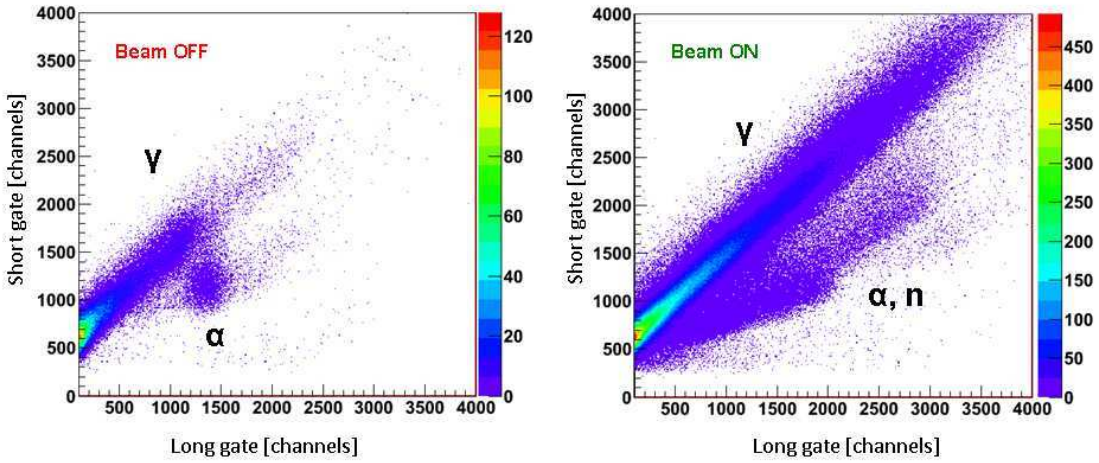

figure 5-9: 2D PSD spectra for 14 MeV neutrons obtained with BaF_2 detector. Left: background measurement performed with the neutron beam switched off and corresponding to the internal radioactivity of BaF_2 scintillator (analogous to figure 5-6 left). Right: neutron measurement with beam turned on. Two different aligned sets of points corresponding to γ and massive particle interactions are distinguishable.

In the left part of figure 5-9 it is shown the background 2D PSD spectrum of BaF_2 acquired with the neutron beam switched off. The γ and α interactions are due to the internal radioactivity of BaF_2, nevertheless this spectrum differs from the one presented in figure 5-6 because the high voltage applied to the PMT was set to lower values to allow for a larger range in the charge integration on the acquired signal. In the right part of figure 5-9 is shown the 2D PSD spectra acquired during neutron irradiation. It can be noticed that a large increase in γ-interactions compared to background is clearly visible from the big γ aligned set of points. Indeed, the neutrons produced by the tube generator undergo a huge amount of scattering reactions on the walls of the very small volume (< 1 m^3) irradiation cave with a consequent production of photons through (n,nγ) reactions.

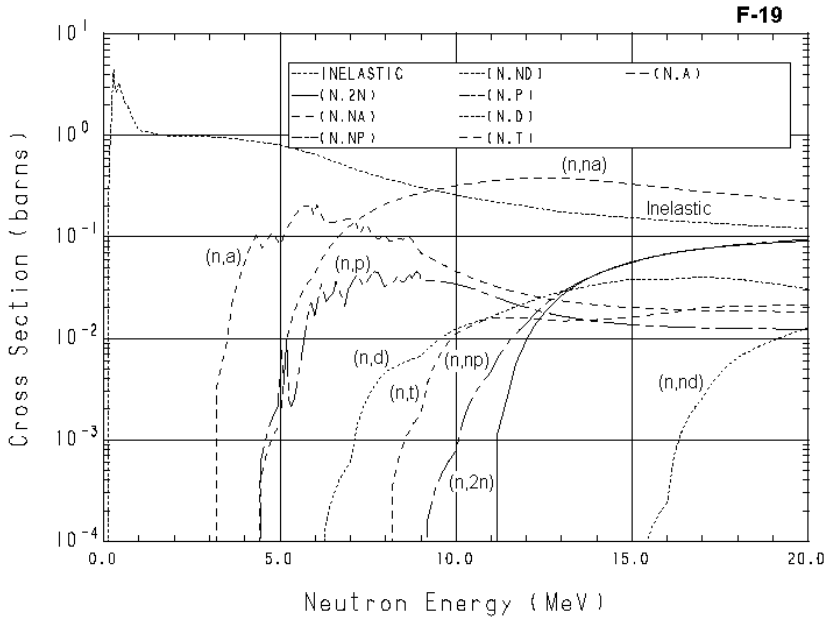

figure 5-10: neutron interaction cross sections on ^{19}F atoms. In the inset 'Inelastic' stays for inelastic scattering mainly leading to (n,nγ) reactions. Figure obtained from http://wwwndc.jaea.go.jp/

The analysis of neutron interactions is more delicate. Indeed, at least in principle, a clearly identifiable aligned set of points due to neutron interactions would be expected to rise in between the γ and α stripes since, on average, neutrons have an ionizing power in between γ and α particles. This is not the case of the 2D PSD spectrum on the right of figure 5-9 in which, neutrons seem rather to produce a stripe of points overlaying the α-particles. Nevertheless, particular care has to be taken in analyzing the kind of reactions neutrons undergo in BaF_2. On average, neutron interaction cross sections on fluorine are two orders of magnitude higher than on barium (JAEA website), and fluorine is twice as abundant as barium in BaF_2 scintillator, therefore we can just consider fluorine cross section in our analysis. As can be noticed in figure 5-10, for neutrons of 14 MeV the sum of ^{19}F cross sections leading to α production, namely (n, α) and (n, nα) is one order of magnitude higher than the sum of reaction cross sections leading to proton production, namely (n, p), (n, d), (n, t), (n,np). Therefore it is not astonishing that the main neutron 'signature' would result as a α stripe of points on the 2D PSD spectrum. To be rigorous, in figure 5-9, after channel 2000 on the long gate axis, the slope of the α-stripe changes slightly. This could be the signature of rarer reactions leading to proton production, but this hypothesis should be further investigated. Some attempts have been done in using different integration gates for the BaF_2 signal, namely the same total and delayed integration gates applied to BC501, but this did not lead to any better achievement in PSD quality. Finally we can conclude that n-γ discrimination with BaF2 is quite poor at least when compared to PSD performances that can be achieved with BC501 in the same experimental conditions and reported in figure 5-11.

It has to be pointed out that neutron interactions with BC501 scintillator mainly occur through elastic and inelastic scattering of neutrons over free hydrogen nuclei of the liquid scintillator. This makes n-γ discrimination particularly efficient as shown in figure 5-11 where neutron and photon signals can be clearly discriminated down to energy of few hundreds keV.

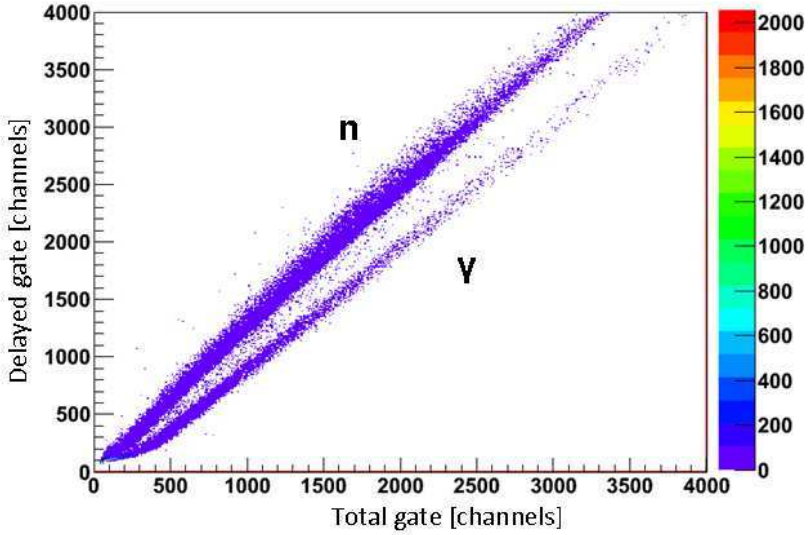

figure 5-11: 2D PSD spectra for 14 MeV neutrons obtained with BC501 detector. Two different aligned sets of points corresponding to γ and neutron interactions are clearly distinguishable.

5.2 Measurements of prompt γ-rays produced from C-ion fragmentation

The first experiment performed by our group about prompt γ-rays measurements produced from C-ion fragmentation has been performed at GANIL cyclotron with 73 MeV/u $^{13}C^{6+}$ ions (E. Testa et al. 2008). As already mentioned in section 4.2 the main result of the experiment was the demonstration of the correlation between the longitudinal prompt photon profile and the Bragg-peak position (see figure 4-6). The basic set-up of that first experiment, i.e. a collimated scintillator detecting the prompt γ-rays emitted orthogonally to the beam direction, has been re-proposed and improved in this work and it is presented in the following sections. In particular, better achieving scintillators have been employed for TOF measurements and specific neutron detectors have been used to investigate a possible prompt neutron correlation with the ion range. Moreover we extended our measurements to high energy C-ions and to synchrotron accelerators. Finally, we performed a preliminary experiment with a multi-detector set-up to identify the main constraints on the design of a future prototype of multi-collimated and multi-detector prompt gamma camera which would be potentially applied clinically and which is planned to be built in our group.

5.2.1 GANIL and GSI single-detector experimental set-up

Two new series of experiments for the measurement of prompt photons produced during ^{12}C-ion fragmentation have been performed at GANIL and GSI facilities.

In the experiment performed with 95 MeV/u ^{12}C-ions at GANIL, C-ions extracted from the vacuum beam line directly hit a cubic polymethyl methacrylate $(C_5H_8O_2)_n$ (PMMA, ρ=1.2g/cm^3) target (50 x 50 x 50 mm^3). At GSI, higher energy ions, of 292 MeV/u and 305 MeV/u, bombarded a water target (12 × 25 × 20 cm^3). In figure 5-12 are shown the schemes of the two experimental set-ups. In both experiments the targets were placed on a table which could be remotely moved along the beam axis. Two detectors were used: the BaF_2 and the BC501 scintillators which have already been presented in Table 5-2. The BaF_2 scintillator was chosen for its excellent time response and its high efficiency for photon detection, while the BC501 was used for its high neutron detection efficiency therefore particularly suitable to investigate a possible prompt neutron component correlated with the ion range. Moreover, as described in the previous paragraphs, BC501 presents excellent quality for neutron-photon identification through pulse shape discrimination.

At GANIL, two different collimation materials (i.e., lead and paraffin) were respectively employed for the BaF_2 and BC501 detectors. This was done to optimize the collimation of the photon component for the BaF_2 detector, and of the neutron component for BC501 scintillator. Moreover we investigated the effect of the target density on the photons rate production by inserting in the PMMA target a 2mm thick plate of bone equivalent material (PTFE ρ=2.3g/cm^3) and a 6mm thick plate of lung equivalent material (Soft tissue ICRU-44 ρ=0.2g/cm^3). We investigated as well the influence of the target volume on the photon diffusion and attenuation by irradiating a small cylindrical PMMA target (2 cm diameter – 5 cm length) and a big cubic water target (30 × 30 × 30 cm^3).

At GSI, a single lead collimator was used for both the BaF_2 and BC501 detectors, which were stacked as it can be seen in figure 5-13. Nevertheless an additional paraffin collimator was added behind the lead collimator in the experiment with 305 MeV/u C-ions. Indeed, the main difference between these two experiments performed at GSI, was the lead-collimator slit aperture which was, respectively, 10 mm and 4 mm for the 292MeV/u and 305 MeV/u experiments. The additional paraffin collimator was therefore used to better highlight the prompt photon signal over the neutron induced background as will be explained in more detail further in this chapter. A second minor difference between the two GSI experiments is the distance between the target and the detectors that was increased from 1 m to 1.3 m in the experiment with 305 MeV/u C-ions.

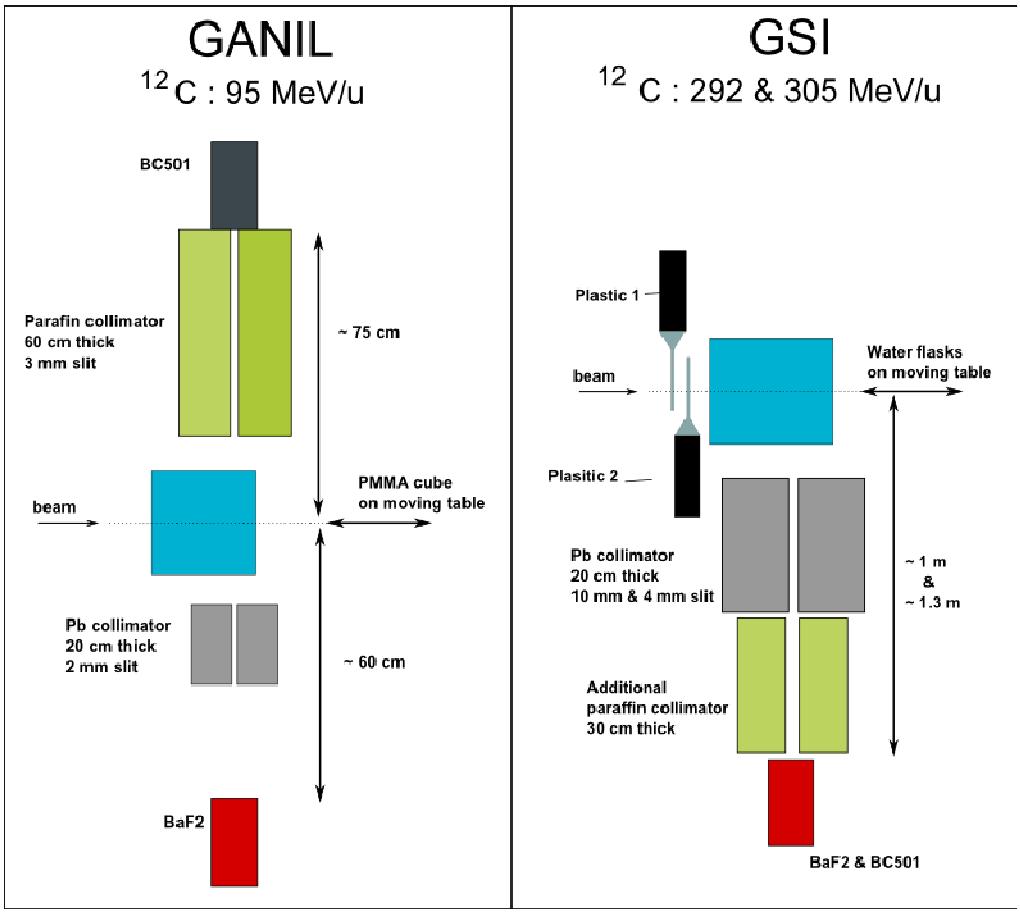

figure 5-12: Diagram of the GANIL (left) and GSI (right) experimental set-up. At GSI an additional paraffin collimator was added when the lead collimator slit was reduced to 4 mm in the experiment with 305 MeV/u C-ions. The distance between target and detectors was 1m for the experiment with 292 MeV/u C-ions (Pb-collimator slit: 10mm) and 1.3 m in the experiment with 305 MeV/u C-ions.

The main difference between GANIL and GSI experiments is related to time pick-up measurements where the beam structure plays a major role and which will be discussed more in details in section 0. In fact, our ion range verification technique rests upon the measurement of the time interval between the impact of the C-ions on the target and the photon detection by the scintillators. This is done by means of a Time to Amplitude Converter module (TAC). At GANIL, where the beam is pulsed (beam pulse of ~1 ns every 80 ns), the cyclotron high-frequency (HF) signal (suitably delayed) could be used as stop signal. The start signal was provided either by the BaF_2 or BC501 detection of a photon or neutron in an event-by-event acquisition mode. The choice of taking the start signals from those detectors showing the lowest counts was adopted to minimize the number of void events for which a start signal does not have a corresponding stop signal. The beam intensity was monitored by the NaI(Tl) '3 inches' detector presented in Table 5-2 (not shown in figure 5-12) placed at a large distance from the target, in order to obtain a counting rate proportional to the beam intensity but nearly independent of target position and collimation. This NaI(Tl) detector was calibrated with a Faraday cup at higher intensities (see Appendix). The beam intensity was set to about 1 nA (10^9 ions/s), in order to optimize the detector counting rates while avoiding pile-up and dead-time

effects. In contrast, at the SIS-GSI synchrotron, where a continuum extraction mode was used (~8 s extraction every ~10 s), the TOF stop signal was provided by two thin plastic scintillators intercepting the beam. During the carbon ion extraction, the intensity was kept at quite a low value (a few 10^5 ions/s), to allow an ion-per-ion triggering by the plastic scintillators (their efficiency was checked by comparing single and coincidence detection modes). These scintillators were also used to measure the integrated number of ions hitting the target. For both experiments, the detectors readout (time and energy distributions) was performed with conventional NIM electronics and a VME data acquisition system. The signal processing schematics are presented in the Appendix.

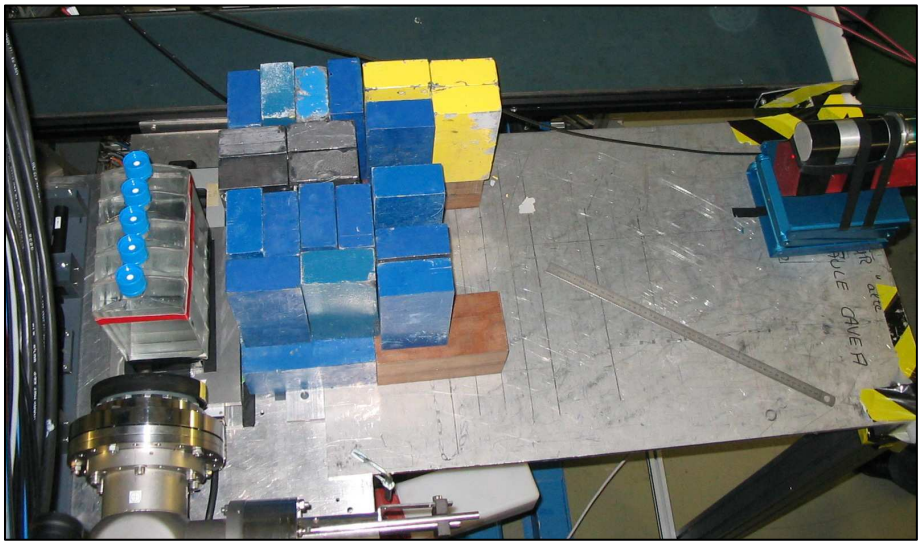

figure 5-13: Picture of GSI experimental set-up. From left to right are visible: the beam line exit window in front of the water filled flasks (target), the lead collimator (gray) with additional lead-bricks shielding (blue and yellow), the superimposed BaF_2 and BC501 detectors. Two thin plastic trigger-scintillators (not present in this picture) were place between the vacuum window and the water target. The additional paraffin shielding between the detectors and the collimator is not showed in this picture.

5.2.1.1 Calculation of detection solid angle and field of view

The determination of the solid angle and the detector field of view is not straightforward in our set-up with high energy γ-rays mainly because of the necessity of taking into account the scattering of photons, the collimator absorption and attenuation coefficients, and the detector efficiency. For these reasons the detection solid angle and the field of view have been evaluated by means of Monte Carlo simulations which therefore took into account the shadowing effects around the edges of the collimator slit. The detailed description of these Geant4 simulations may be found in (Le Foulher 2010).

The experimental set-up was reproduced in a simulation in which a linear source of isotropically emitted photons (with the same energy spectrum of prompt photons created during fragment de-excitation) replaced the PMMA or water target.

The detection field of view L, which, in our case, corresponded to the ion-range segment from which photons could be detected, is defined as

$$L = \int_{-\infty}^{\infty} P(z)dz \approx FWHM$$

$P(z)$ is obtained by simulation and it represents the probability of detecting a photon which has been emitted at an axial position z as reported in figure 5-14. In practice $P(z)$ is obtained by normalization of the spectrum of the detected photon emission points over its maximum value. Therefore L can be assumed equivalent to the FWHM of $P(z)$ and its values are reported in Table 5-3 for the different experimental set-up.

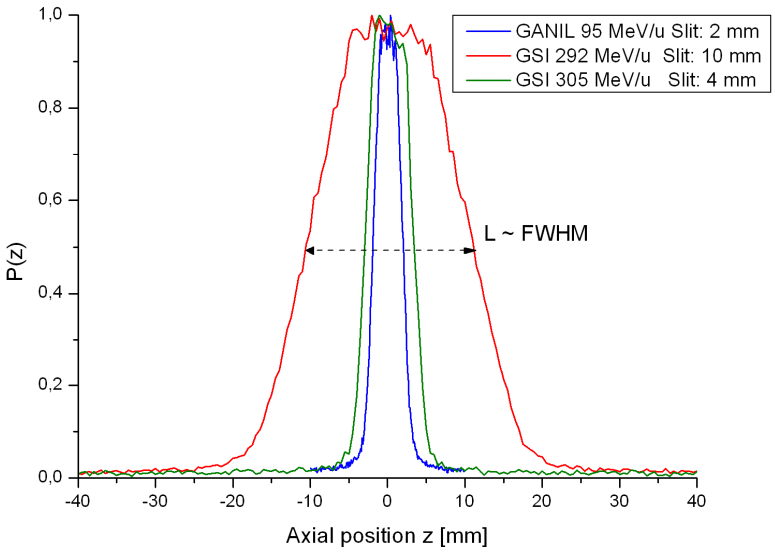

figure 5-14: Simulated detection probability for GANIL and GSI experimental set-up (20 cm long Pb collimator, geometry shown in Fig. 1-12). The origin of the axial position corresponds to the center of the collimator slit. Figure adapted from (Le Foulher 2010).

The detection solid angle Ω_d is defined as follows

$$\Omega_d = \frac{N_{\gamma-Det}}{\frac{dN_{\gamma-Emit}}{dz} L} 4\pi$$

$N_{\gamma\text{-}Det}$ is the total number of detected photons, $dN_{\gamma\text{-}Emit}/dz$ is the linear density of emitted photons and L is the detection field of view. The values of Ω_d for the different experimental configurations are reported in Table 5-3.

	Collimator slit aperture [mm]	Field of view L [mm]	Ω_d [sr]
GANIL 95 MeV/u	2	4.1	4.33×10^{-4}
GSI 292 MeV/u	10	22	1.07×10^{-3}
GSI 305 MeV/u	4	6.4	4.54×10^{-4}

Table 5-3: Values of field of view and detection solid angle obtained by Geant4 simulation. Table adapted from (Le Foulher 2010).

5.2.2 GANIL multi-detector experimental set-up

A preliminary experiment with a multi-collimator and multi-detector set-up has been recently performed at GANIL with 75 MeV/u ^{13}C-ions fully stopping in a cubic PMMA target (50 x 50 x 50 mm^3). As can be seen from figure 5-15, the general set-up of the experiment is similar to the one presented in the previous paragraph except for the fact that this time, four LYSO detectors (presented in Table 5-2: Dimensions of the detectors used in this work for γ and neutron measurements) have been stacked and each of them was aligned behind a dedicated slit of the tungsten alloy (Densimet® ρ=17 g/cm^3) multi-slit collimator positioned orthogonally to the beam direction. On the opposite side of the target, always orthogonally to the beam direction, a single 'reference' LYSO detector was aligned behind a lead collimator. Since in principle, the collimator allows to shield all the photons emitted not orthogonally to the beam direction, each LYSO scintillator is supposed to detect only the photons emitted in the field of view of its own aligned collimator-slit. Nevertheless, both collimator-slits and detectors photon "cross-talk" (scattering from one detector to the neighbouring one) can take place leading to axial photon detection positions different from the emitted positions. This phenomenon will be discussed in more detail in the next chapter.

Since the inter-slit distance was 8 mm (the inter-detector distance was therefore 8 mm as well) and the ion path was ~15 mm, only two LYSO detectors were aiming at the ion path at the same time. Therefore to allow, for each LYSO detector, a complete scan of the photon profile induced by the full ion path, the target was again placed on a remote controlled table moving along the beam direction. The still relatively high inter detector distance was nevertheless achieved by an optimized design of the detectors arrangement as shown in figure 5-16. Indeed the large photomultiplier tube (PMT) diameter (Ø 2 cm), compelled the use of symmetric and asymmetric light guide to connect the LYSO crystals to the PMT in order to achieve the most compact possible detector arrangement. Moreover, the choice of using LYSO crystals with different dimensions (as presented in Table 5-2) has been made to investigate which are the most suitable scintillator volumes for a future prototype. Indeed, as already mentioned, the actual multi-detector set-up is still preliminary and more detailed discussions about future improvements will be given in section 0.

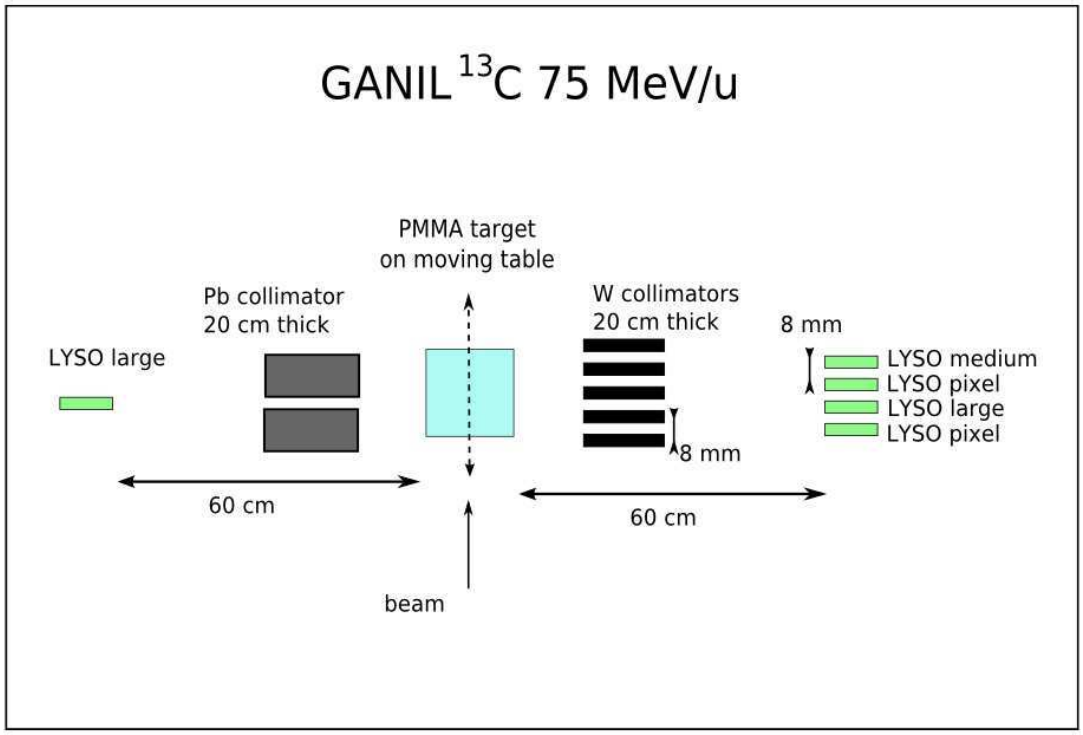

figure 5-15: Diagram of GANIL multi-detector experiment.

Like for the single-detector experiment at GANIL, the beam intensity was monitored by a NaI(Tl) detector whose counting rate was proportional to the beam intensity and independent of target position. The beam intensity was again set to about 1 nA (10^9 ions/s), nevertheless since in this experiment, five detectors were read out at the same time, dead-time corrections in data processing become necessary. As in the experiment with single-detector, the stop signal for TOF measurement was provided by the cyclotron high-frequency (HF) signal (suitably delayed). The start signal was provided by the detection of a photon or neutron by any of the five LYSO scintillators in an event-by-event acquisition mode. In the on-line and off-line data analysis a pattern unit module was used to identify which LYSO scintillator triggered the acquisition event.

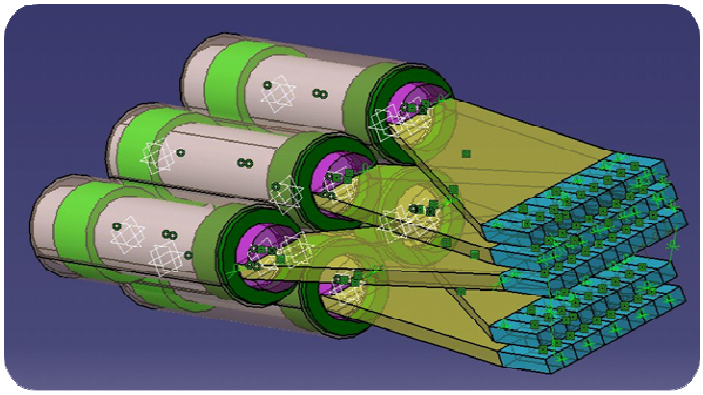

figure 5-16: Technical drawing of LYSO detectors arrangement. In the GANIL multi-detector experiment only two LYSO detectors were constituted by pixilated crystals.

5.3 Results and discussion

5.3.1 GANIL and GSI single-detector experimental results

5.3.1.1 Time of flight spectra analysis

In figure 5-17 and figure 5-18 are shown the time of flight spectra for the BaF_2 detector obtained at GANIL and GSI respectively. The time reference is set in a way that the origin of the time scale corresponds to the time when the C-ions hit the target. An energy selection on the events depositing in the detector more than 2 MeV and 4 MeV is performed to obtain the TOF spectra represented by the red and blue curves respectively.

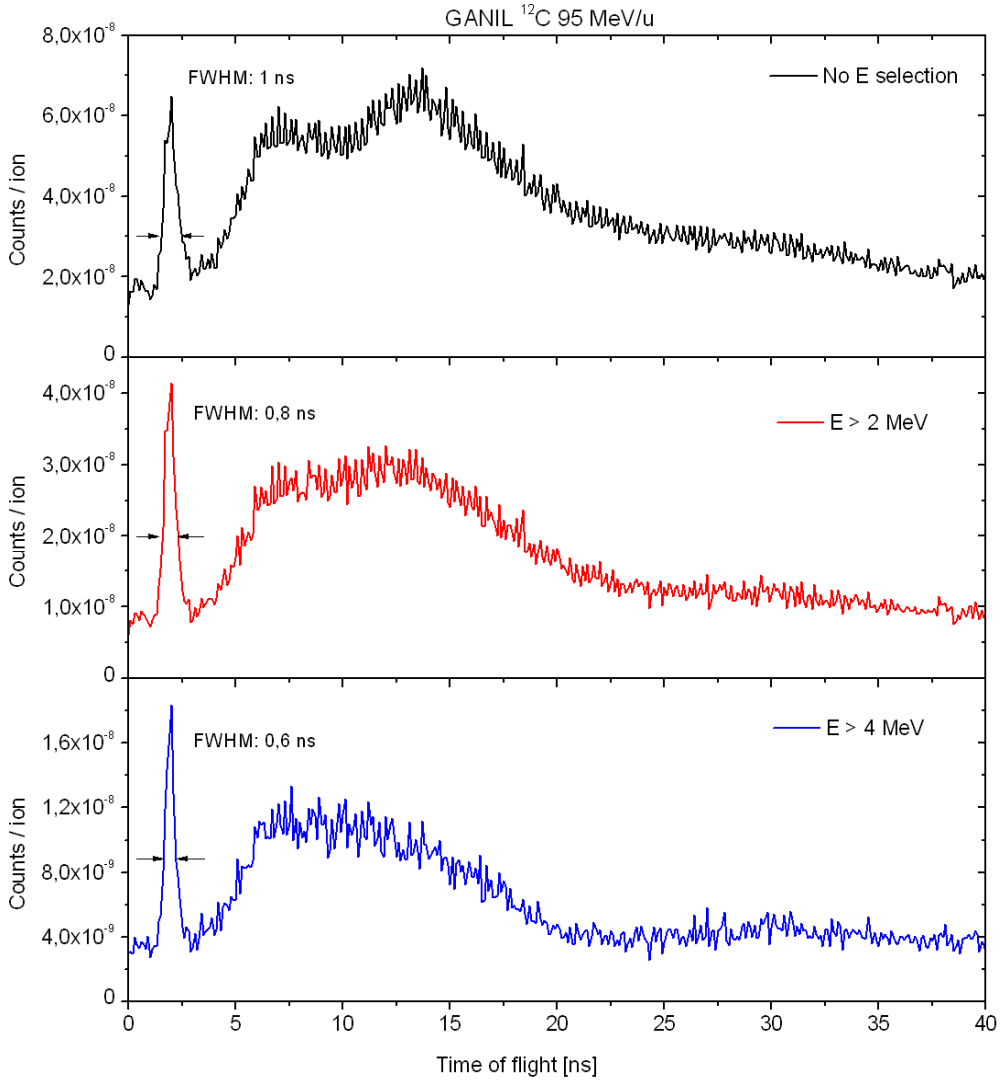

figure 5-17: Time of flight spectra for BaF_2 detector for the GANIL experiment with ^{12}C ions of 95 MeV/u. The origin of the time scale corresponds to the time when the C-ions hit the target. Red and blue spectra are obtained by selecting the events which deposit in the detector more than $2MeV_{pe}$ and $4MeV_{pe}$ respectively. Spectra are obtained with the collimated detector looking at a target penetration depth of 16 mm. The bin width is 0.1 ns.

In figure 5-17 a sharp prompt photon peak is clearly identifiable at 2 ns. The structures that follow the prompt photon peak are due to neutron-induced

radiation which is therefore detected after the prompt photons. These neutron-induced structures will be examined in more details in the next paragraph. Nevertheless we can already state that they are mainly due to neutron induced radiation produced in the collimator and in the experimental cave walls. Moreover their shape and integral are strongly affected by the energy selection performed on the TOF spectra. The lower the energy threshold, the higher is the number of detected photons which have scattered at the walls of the cave. This explains why, with no energy cut, the component at 10-20 ns is higher than the one at 5-10 ns.

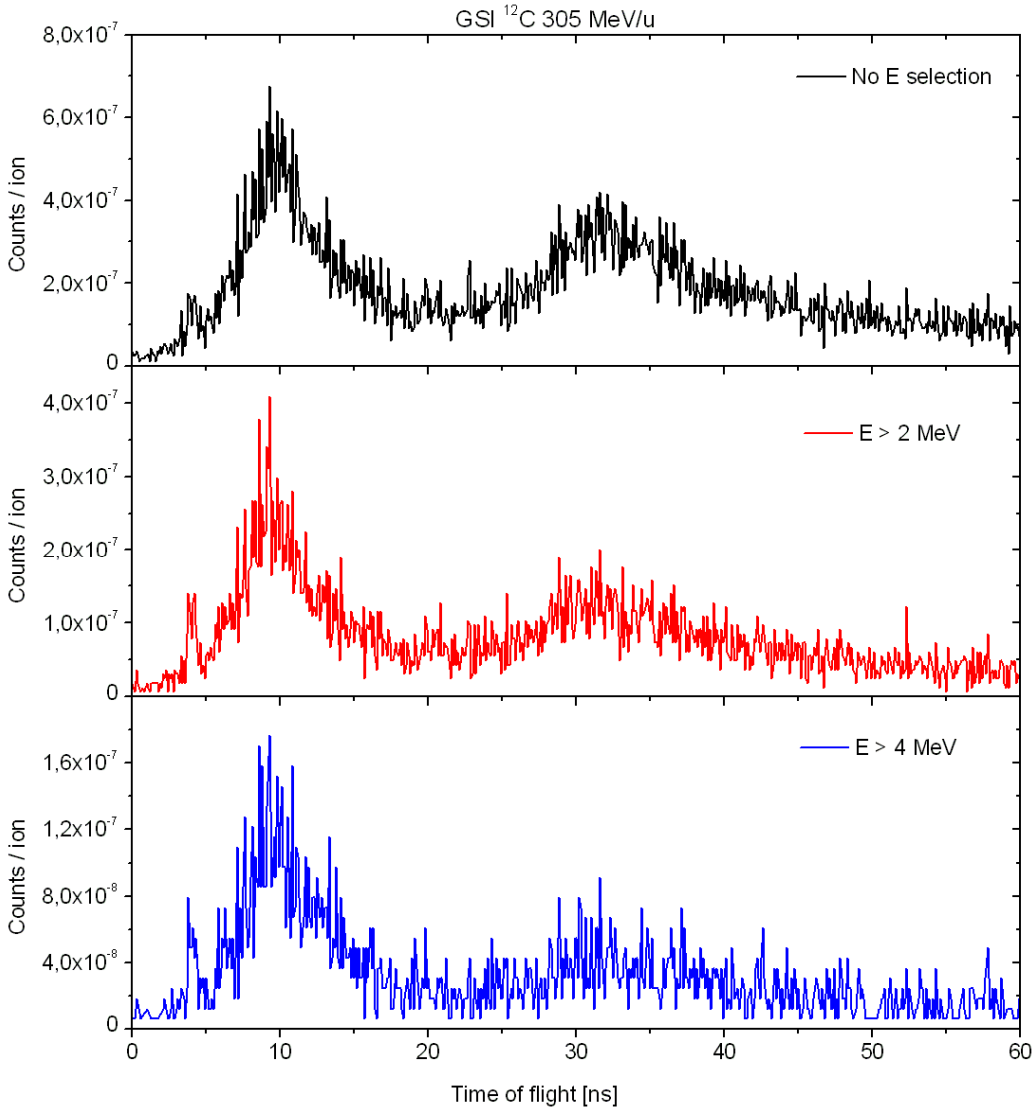

figure 5-18: Time of flight spectra for BaF_2 detector for the GSI experiment with ^{12}C ions of 305 MeV/u. The origin of the time scale corresponds to the time when the C-ions hit the target. Red and blue spectra are obtained by selecting the events which deposit in the detector more than 2 MeV_{pe} and 4 MeV_{pe} respectively. Spectra are obtained with the collimated detector looking at a target penetration depth of 170 mm. The bin width is 0.1 ns.

In figure 5-18 the prompt photon peak arises at about 4 ns. The main difference between the TOF spectra obtained at GSI and GANIL is the acquired counting statistics that is on average one hundred times lower at GSI. This is mainly due

to the limited beam time and the low beam intensity required for single ion triggering with the plastic scintillators. Moreover, an energy selection on the events depositing at least 2 MeV in the detectors is necessary to clearly spot the prompt photon peak. Indeed the neutron induced structure arising just after the prompt photon peak is due to the total neutron production along the entire ion path. Therefore on GSI spectra, this second structure is higher because the ion range at 305 MeV/u is ~180 mm compared to ~21 mm at 95 MeV/u and the average fragmentation rate is ~50 % for C-ions at 305 MeV/u and only ~10 % for C-ions at 95 MeV/u.

As already mentioned in section 0, an additional paraffin collimator was added in front of the lead collimator for the experiment at GSI with C-ions at 305 MeV/u. The influence of this additional paraffin shielding on the TOF spectra is shown on figure 5-19. It can be seen how the additional paraffin lowers the neutron induced structure arising just after the prompt photon peak which is, however, still clearly identifiable even without paraffin. Nevertheless, the major part of the experiment and all the results presented in the following have been performed with the additional paraffin shielding mainly because, in the online analysis, performed during the experiment, the effect of the paraffin shielding in increasing the ratio of prompt photon signal over neutron-induced background resulted to be higher than what it could have been more properly estimated offline and reported in figure 5-19.

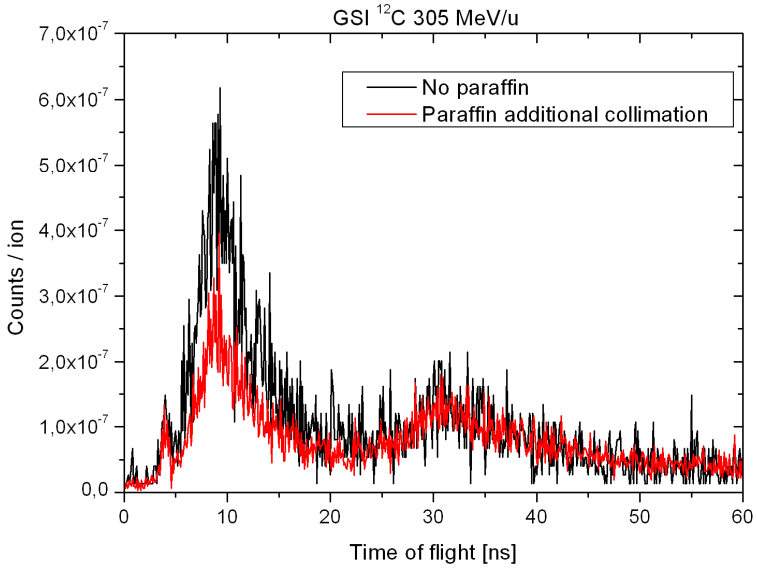

figure 5-19: Time of flight spectra for BaF_2 detector for the GSI experiment with ^{12}C ions of 305 MeV/u with (red curve) and without (black curve) additional paraffin shielding. Both spectra are obtained by selecting the events which deposit more than 2MeV$_{pe}$ in the detector. The origin of the time scale corresponds to the time when the C-ions hit the target. Spectra are obtained with the collimated detector looking at a target penetration depth of 150 mm. The bin width is 0.1 ns.

In the left part of figure 5-20 is shown a two-dimensional spectrum of the energy deposited in the BaF_2 detector as a function of the TOF, when the detector was looking at a region close to the Bragg-peak in the experiment at GANIL with 95 MeV/u ^{12}C-ions. As already shown in figure 5-17, a sharp

prompt photon stripe rises at 2 ns having a continuous energy distribution that goes up to more than 6 MeV. The energy calibration for this energy-TOF spectrum and as well for all the following energy-TOF spectra, was done using γ-emitting radioactive sources. It is observed that selecting photon energy above 2 MeV improves the signal-to-background ratio. It can be noticed that a time resolution of about 1 ns (see as well figure 5-17) has been achieved with the BaF_2 scintillator. The comparison with the energy-TOF spectrum reported in the right part of figure 5-20, and obtained in the first study performed by our group (not described in this work) with a NaI(Tl) detector (E. Testa et al. 2009) shows that BaF_2 has a time-resolution which is 4-5 times better than NaI(Tl) (Wisshak & Käppeler 1984).

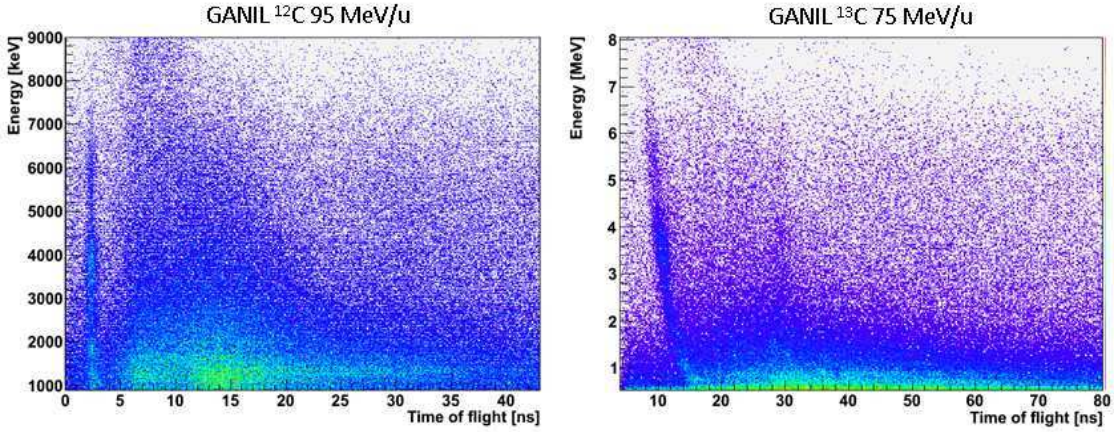

figure 5-20: Left: Two-dimensional spectrum of the energy deposited in the BaF_2 detector as function of TOF. The spectrum was obtained at GANIL with 95 MeV/u ^{12}C-ions with the collimated detector looking at a target penetration depth of 16 mm. The origin of the time scale corresponds to the time when the C-ions hit the target. The energy axis is calibrated for photons. Right: Two-dimensional spectrum of the energy deposited in a NaI(Tl) detector as function of TOF obtained at GANIL with 75 MeV/u ^{13}C-ions. Spectrum adapted from (E. Testa et al. 2009).

In figure 5-21 is shown a two-dimensional energy-TOF spectrum obtained with the BC501 detector looking at a region close to the Bragg-peak in the GANIL experiment with 95 MeV/u ^{12}C-ions. The prompt photon peak arising at 5 ns dominates the energy-TOF spectrum because of the poor γ-rays collimation properties of the paraffin collimator in front of the BC501 detector. Indeed the 60 cm thick paraffin collimator has an absorption length corresponding to ~5 cm of lead which is completely insufficient to shield prompt γ-rays with energy of several MeV produced during the fragments de-excitation and reported in spectrum of figure 5-21. Therefore it can be assumed that the amount of prompt-photons detected by the BC501 scintillator corresponds to the entire prompt photon production along the entire C-ion path and emitted in the field of view of the BC501 detector. As already mentioned, the paraffin collimator was employed to investigate a possible prompt neutron component in TOF spectrum and therefore, for practical considerations, the BC501 detector could be considered uncollimated for γ-rays. Nevertheless no prompt neutron component could be directly distinguishable on the spectrum of figure 5-21 and more detailed analysis using the PSD technique, will be presented in the next paragraph.

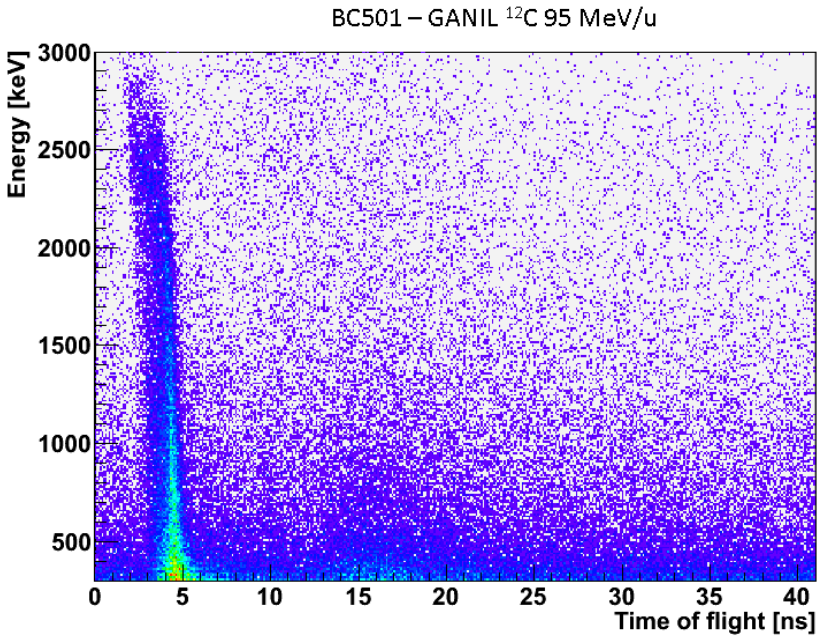

figure 5-21: Two-dimensional spectrum of the energy deposited in the BC501 detector as function of TOF. The spectrum was obtained at GANIL with 95 MeV/u ^{12}C-ions and the paraffin-collimated detector looking at a target penetration depth of 16 mm. The origin of the time scale is arbitrarily set. The energy axis is calibrated for photons.

In figure 5-22 is shown a two-dimensional energy-TOF spectrum obtained with the BaF_2 detector looking at a region close to the Bragg-peak in the GSI experiment with 292 MeV/u ^{12}C-ions. Although the acquired statistic is much lower than in the energy-TOF spectrum obtained at GANIL and presented in figure 5-20, the relatively large slit width (10 mm) of the lead collimator used in this experiment allows the identification of the prompt photon peak at ~5ns. On the contrary in the energy-TOF spectra obtained at GSI with a collimator slit width of 4 mm used in the experiment with 305 MeV/u ^{12}C-ions and corresponding to the spectra reported in figure 5-18, the prompt photon peak is hardly identifiable due to the too low acquired statistics. Indeed as first approximation the field of view of the detector, and therefore the rate of detected prompt photons, linearly depends on the collimator slit aperture. However, even the spectrum presented in figure 5-22, is dominated by neutron-induced radiation which is detected after the prompt photon component and which contributes to the broad background noise. It is observed even in this case, that selecting photon energy above 2 MeV improves the signal-to-background ratio.

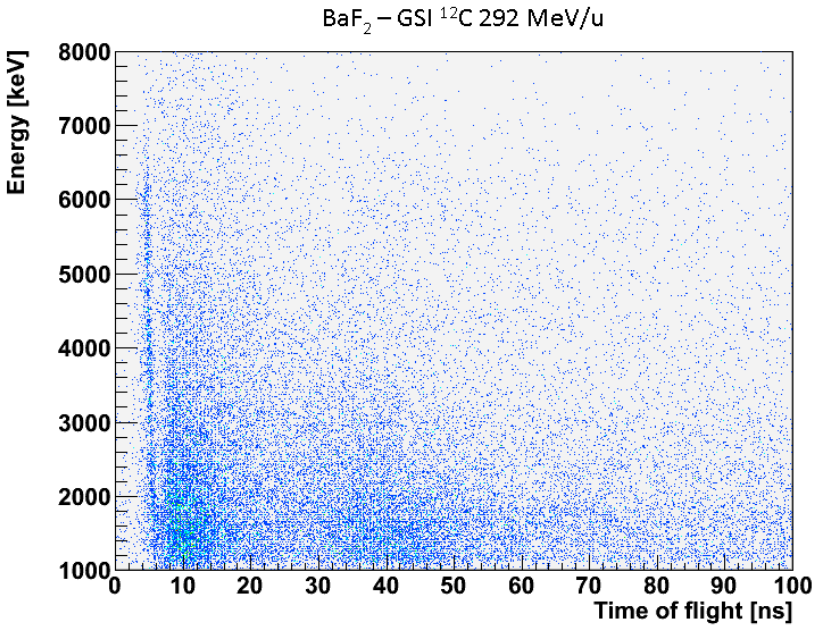

figure 5-22: Two-dimensional spectrum of the energy deposited in the BaF_2 detector as function of TOF. The spectrum was obtained at GSI with 292 MeV/u ^{12}C-ions and the collimated detector looking at a target penetration depth of 150 mm. The origin of the time scale is arbitrarily set. The energy axis is calibrated for photons.

5.3.1.2 Time of flight (TOF) spectra analysis conditioned by pulse shape discrimination (PSD)

As already mentioned in the previous paragraph, a more detailed analysis of the time of flight spectra can be performed introducing the information about the type of particle which contributes to each event of the TOF spectra. With PSD, neutrons and photons detected by the BC501 scintillator could be clearly distinguished in both the experiments performed at GANIL and GSI. At 90° with respect to the beam direction, where the detectors were placed, photons and neutrons overwhelm all the charged particles produced during ion fragmentation.

In figure 5-23 two examples of 2D PSD spectra obtained at GANIL and GSI are given for the BC501 scintillator. As already stated for the results of the test measurements of section 0, the good PSD properties of BC501 allowed distinguishing neutron and photon interactions down to energies of few hundreds of keV. On the contrary, no valuable information could be obtained from the PSD technique applied to BaF_2 detectors where the high internal self-radioactivity and the relatively high (n,α) cross sections made a clear discrimination between photon and neutrons interaction impossible, as it has already been reported in section 0.

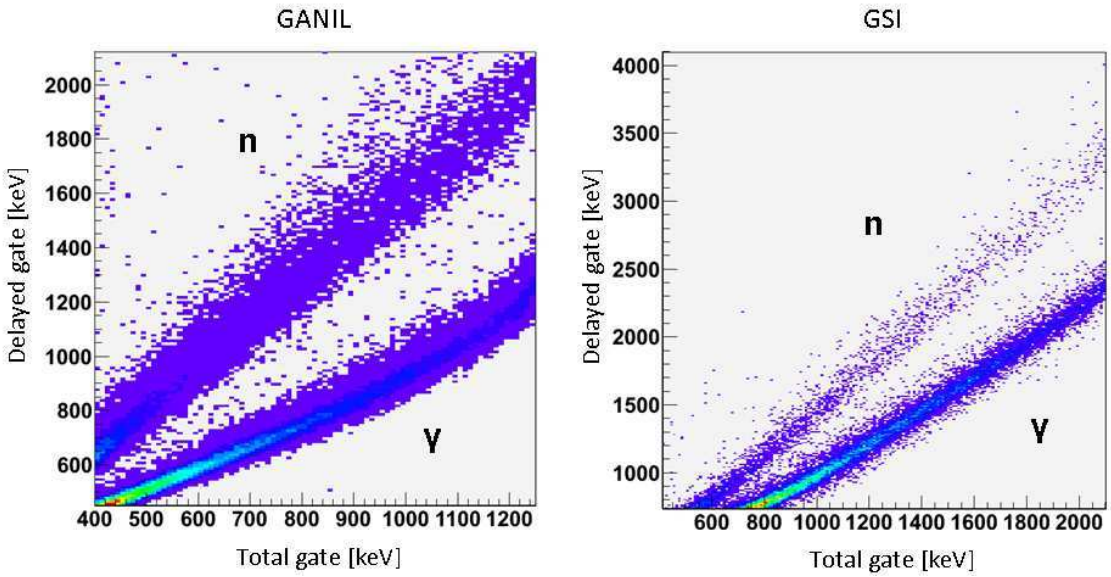

figure 5-23: 2D PSD obtained with BC501 detector for the experiment performed at GANIL with 95 MeV/u ^{12}C-ions (left) and at GSI with 305 MeV/u ^{12}C-ions (right). For both spectra the collimated BC501 detector was looking inside the ion path. The energy axes are calibrated for photons. Two different aligned sets of points corresponding to γ and neutron interactions are clearly distinguishable.

The upper part of figure 5-24 (a,b) shows the BaF_2 TOF spectra for two different longitudinal detector positions: in front of the target entrance (thin lines) and close to the Bragg-peak region (thick lines). In contrast, the lower part of figure 5-24 (c,d) shows the TOF spectra obtained with the BC501 detector for a position close to the Bragg-peak, depending on the nature of the detected particle: photon (thick lines) and neutron (thin lines). In figure 5-24 a and c it is clearly shown that the prompt photon peak arising at 2 ns (GANIL) and at 3-4 ns (GSI) completely disappears when the collimated detector is not focused on the ion path region. It is therefore concluded that these prompt-peak photons have reached the detector after passing through the collimator slit without undergoing any interaction.

In figure 5-24a, a broad distribution is present between 5 and 20 ns. Actually this broad distribution consists of two components hardly distinguishable in the figure (because of applied energy selection, E > 2MeV) but clearly visible in the spectrum with no energy cut of figure 5-17. We attribute the first component, rising between 5 and 10 ns, to photons created through (n-γ) reactions in the lead collimator. Two experimental pieces of evidence confirm this hypothesis: *i)* no structure is present between 5 ns and 10 ns in the BC501 TOF spectrum from the GANIL experiment (figure 5-24b) where the detector was placed behind a paraffin (and not lead) collimator, *ii)* at GSI, where both detectors were placed behind a lead collimator, the TOF-spectra look very similar for both BaF_2 and BC501 detectors (figure 5-24 c and d). Moreover, the simulated neutron energy spectrum presented in figure 5-25 (Le Foulher 2010) shows that, the kinetic energy of neutrons produced by the fragmentation of 310MeV/u ^{12}C-ion in a water target, which are emitted quasi-orthogonally to the beam direction, mainly do not exceed kinetic energies of 150 MeV. Therefore, if we consider the experiment at GSI presented figure 5-24c, the prompt photon peak rises at ~4 ns

while the maximum of the next component is placed at ~9 ns. This would mean that, if all the interactions occurring between the end of prompt photon peak and the maximum of the first structure (~9 ns) would be produced directly by neutrons they would need to have a velocity $v > 0.44c$ corresponding to a kinetic energy higher than 110 MeV. But, as represented in figure 5-25, the amount of neutrons with kinetic energy higher than 100 MeV is negligible at emission angles of ~90 degree while for forward emission angle neutron energy extends up to about twice the energy of the projectile per nucleon as found experimentally (Gunzert-Marx et al. 2008). Therefore we can conclude that even for the case of GSI TOF-spectra the structure rising between 5 and 15 ns in figure 5-24c is mainly due to photons created through (n-γ) reactions in the lead collimator.

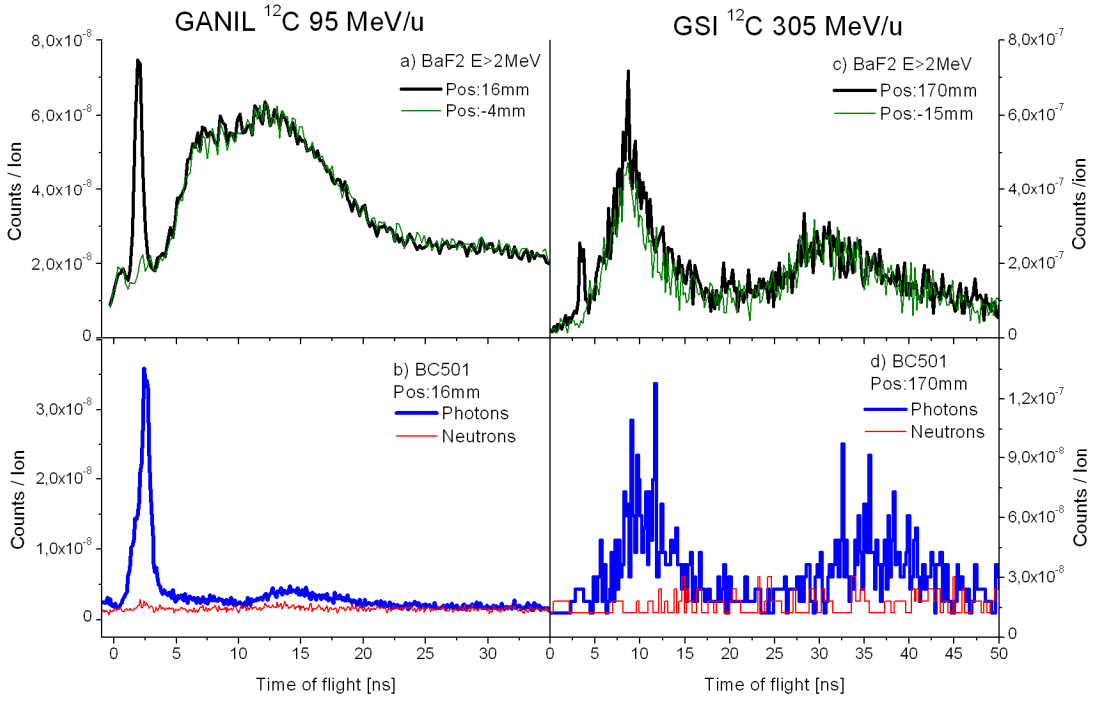

figure 5-24: Left: TOF-spectra for the GANIL (95 MeV/u ^{12}C ion beam) experiment. Right: TOF-spectra for the GSI experiment (305 MeV/u ^{12}C ion beam). The spectra were obtained for detector focussing on a given target penetration depths (Pos=0 corresponds to the target entrance, and the origin of the time scale corresponds to the time of ion impact on the target). The energy selection is performed on the photon equivalent energy of the detected count.

Coming back to figure 5-24a, the second component, rising between 10 and 20 ns, probably comes from photons that have scattered or were produced by neutrons through (n,γ) reactions in the walls of the experimental cave. The same structure is present in the photon TOF-spectrum of figure 5-24b but its intensity is attenuated, due to the low radial detection efficiency of the BC501 detector (5cm in diameter). Moreover, the corresponding structure on GSI TOF-spectra rising between 25 and 45 ns shown in figure 5-24c, demonstrated to not have being affected by the insertion of the additional paraffin in front of the detectors

(see figure 5-19) and therefore can be reasonably assumed to be due to photons scattered at the walls of the cave.

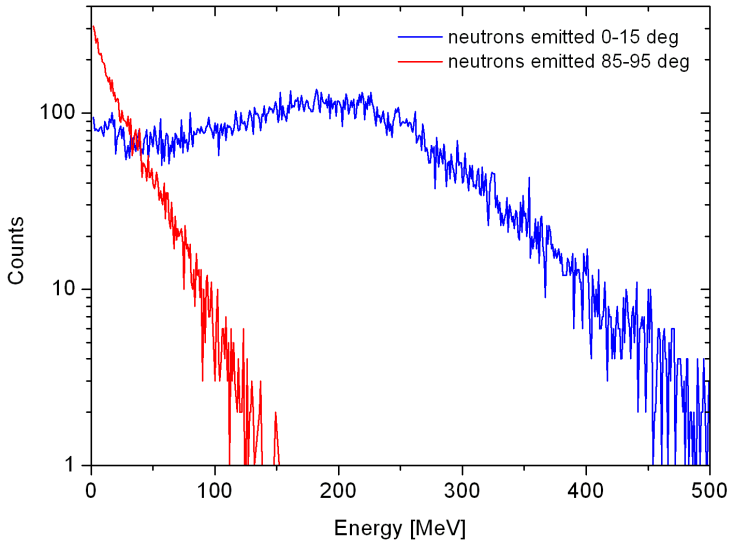

figure 5-25: Simulated neutron energy spectra at their emission points. Neutrons are produced by the fragmentation of 310 MeV/u ^{12}C-ions stopping in a water target. A selection is performed over the quasi-orthogonal neutrons emerging at angles between 85 and 95 degree with respect to the ion direction (red curve) and over the neutrons emitted at forward angle (blue curve). Figure adapted from (Le Foulher 2010).

In figure 5-24b one can notice that the prompt photon peak arising at about 2.5 ns is broader than that in the BaF_2 TOF-spectrum. This is mainly due to the poorer time resolution of the BC501 scintillator and to the photon collimation, which was not optimal because paraffin was specifically used to investigate any prompt neutrons. Additionally, the neutron component of the TOF-spectrum is completely flat (figure 5-24b) similar to that obtained for the GSI measurements (figure 5-24d). Interestingly, no prompt photon peak is visible in the GSI BC501 spectrum (figure 5-24d). This is due to the low statistics accumulated for each target position and to a much poorer photon detection efficiency of the BC501 detector compared to that of the BaF_2 detector (see figure 5-4). Nevertheless, as shown in figure 5-26, the prompt photon peak becomes visible even for BC501 TOF-spectra when the detected statistics is summed-up for all the runs in which the scintillator was looking inside the C-ion range.

As already mentioned, the BaF_2 TOF-spectrum shown in figure 5-24c (GSI) is rather similar to the one presented in figure 5-24a (GANIL) although the statistics was one hundred times lower at GSI. The relative intensity between the prompt photon peak and the photon distribution induced by neutron interactions in the lead collimator (arising from 5 to 15 ns) appears inverted compared to that in figure 5-24a. This is again, due to the total neutron production rate during fragmentation which is much higher at 305 MeV/u than at 95 MeV/u. The time difference between the prompt peak and the third bump (wall-scattered background photons, 25 to 40 ns) can be explained by the

geometrical dimensions of the experimental cave which is larger at GSI than at GANIL.

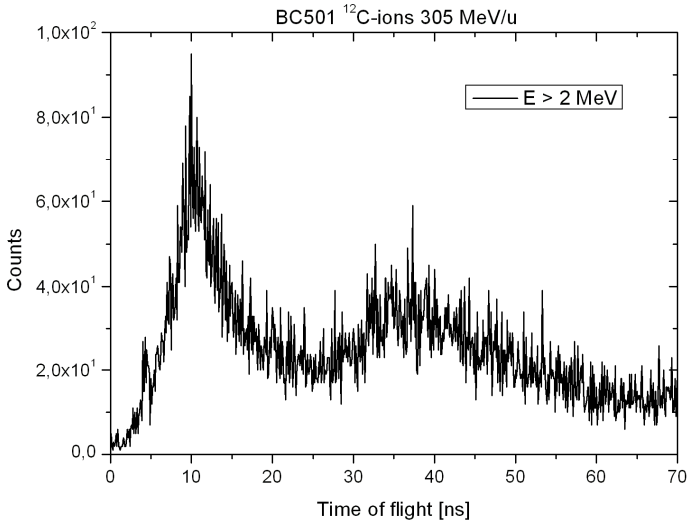

figure 5-26: Sum up of all the TOF spectra obtained with the collimated BC501 detector looking inside the ion path (GSI experiment with ^{12}C ions of 305 MeV/u) at eight different axial positions from 25 mm to 180 mm. The sum-up of the spectra allows the identification of the prompt photon peak. The origin of the time scale corresponds to the time when the C-ions hit the target. The bin width is 0.1 ns and the energy selection is performed on the photon equivalent energy of the detected count.

5.3.1.3 Photon and neutron scan profiles

The ultimate results of the TOF-spectra analysis presented in the previous paragraphs are the scan profiles shown in this section. The prompt photon scan profiles presented in figure 5-27 (red points) was obtained by integrating the counts detected by the BaF_2 scintillator in the prompt photon peak of the TOF-spectra (see figure 5-17) at various longitudinal positions: position 0 corresponds to the target entrance, and the Bragg peak position is marked by a dashed line. The time integration interval was 1.5 ns centered on the prompt photon peak. The scan profile represented by the black points of figure 5-27, is obtained by integrating the counts detected by the BaF_2 scintillator over the entire TOF-spectrum. As mentioned above, a photon energy threshold of 2 MeV was chosen to optimize the statistics and the signal-to-background ratio. In the case of the scan obtained by integrating the prompt photon component of the TOF-spectrum (red points) a clear correlation is observed between the ion path and the photon production yield. The increase of the γ-ray yield at the end of the ion path can be attributed to an increase of the fragmentation cross section and photon emission multiplicity, when the ion energy decreases. On the contrary, the scan profile obtained by integrating the entire TOF-spectrum (black points) is completely flat and therefore uncorrelated to C-ions range. This demonstrates the absolute need of time-of-flight selection of the prompt γ-ray component of the TOF-spectrum to obtain photon scan profiles correlated with the ion range when using the present BaF_2 detector. Indeed it has to be noted that the signal-to-background ratio measured in the present case was not yet optimized: more than 90% of the 1 litre volume of BaF_2 detects only

background, which requires a large quantity of lead shielding to be used, which in turn creates a high neutron and gamma background

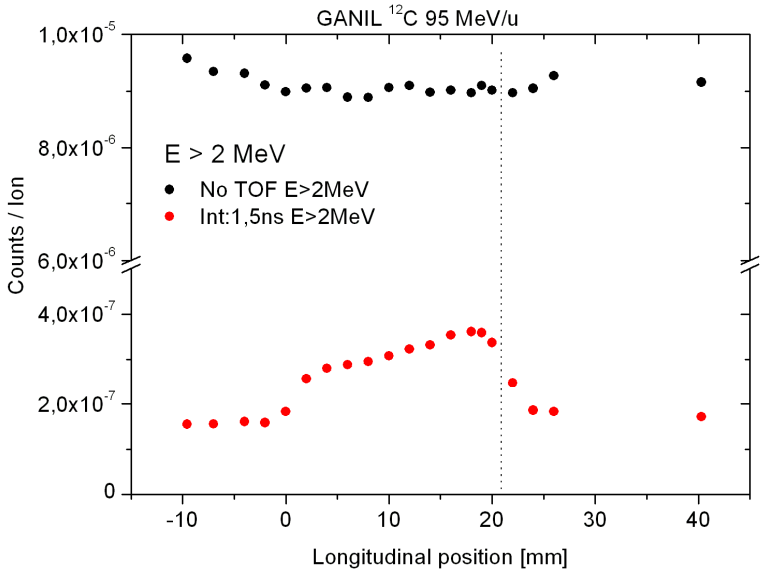

figure 5-27: Longitudinal scan profile obtained for GANIL experiment with 95 MeV/u ^{12}C-ions. The origin of the longitudinal axis corresponds to the target entrance position. The prompt gamma yield obtained by TOF selection (red points) is strongly correlated to the ion path in the target, whereas the counting rate profile without TOF selection (black points) is almost flat. The calculated Bragg-peak position is given by the dashed vertical line.The error bars corresponding to statistical errors are hidden in the dot symbols and the energy selection is performed on the photon equivalent energy of the detected count.

The scan profiles presented in figure 5-28 were obtained by integrating the counts detected by the BaF_2 scintillator in the prompt photon peak of the TOF spectra (see figure 5-18 and figure 5-22) at various longitudinal positions of the GSI experiment with 292 MeV/u and 305 MeV/u ^{12}C-ions. Position 0 corresponds again to the target entrance, and the Bragg peak position is marked by a dashed line. As already done for the GANIL experiment, the time integration interval was 1.5 ns centred on the prompt photon peak and a photon energy threshold of 2 MeV was chosen to optimize the statistics and the signal-to-background ratio. Again, a clear correlation is observed in both cases between the ion path and the photon production yield. A decrease by a factor of about 2 (contrast factor) is seen close to the Bragg-peak position, as reported above for lower energy C-ions from the GANIL facility. On average, the detected prompt γ-ray yields in the experiment with 292 MeV/u are one order of magnitude higher than with 305 MeV/u C-ions. This is due to the larger collimator slit aperture (respectively 10 and 4 mm) which leads to a larger detection solid angle and field of view as reported in Table 5-3.

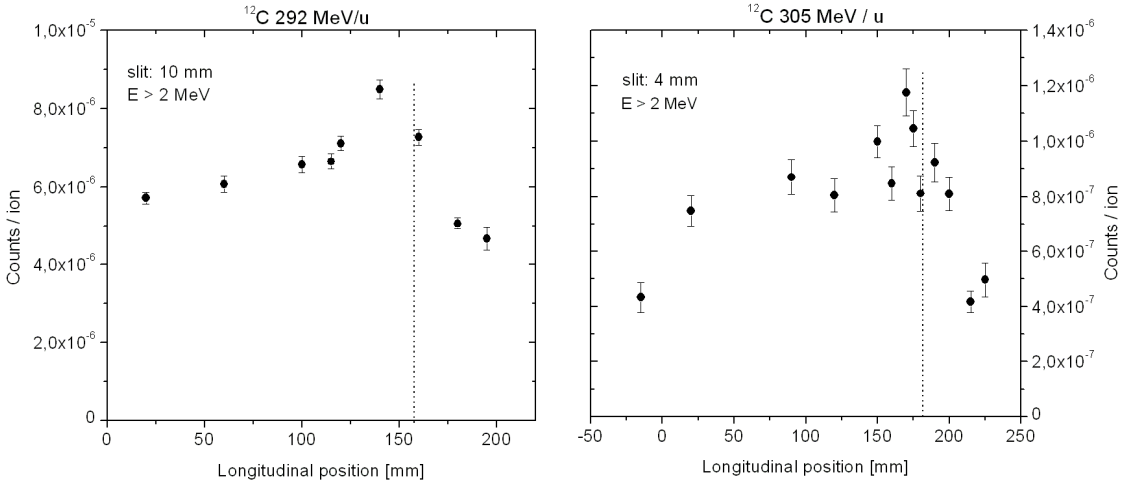

figure 5-28: Longitudinal prompt photon scan profile obtained for GSI experiment with 292 MeV/u ^{12}C-ions (left) and 305 MeV/u ^{12}C-ions (right). The calculated Bragg-peak position is given by the dashed vertical line. The error bars correspond to the statistical errors only and the energy selection is performed on the photon equivalent energy of the detected count.

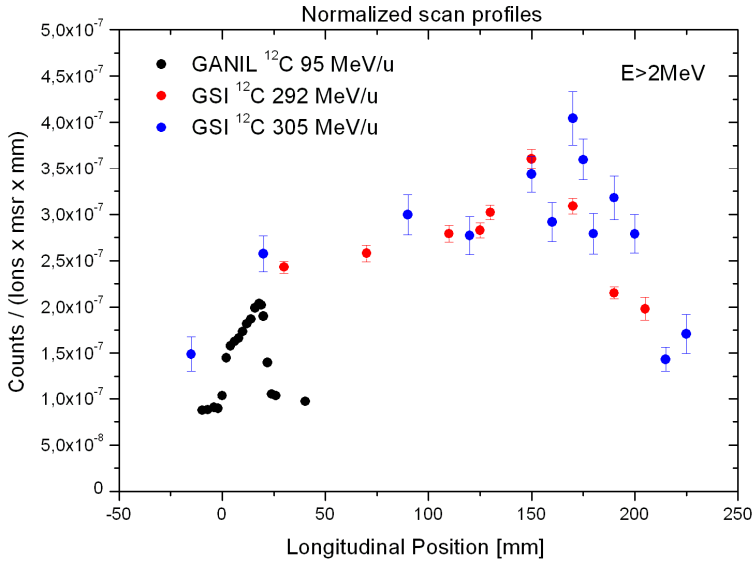

figure 5-29: GANIL and GSI prompt photon profiles normalized over the detection solid angle and field of view presented in Table 5-3. The energy selection is performed on the photon equivalent energy of the detected count.

To compare the detected prompt γ-ray yield for GANIL and GSI experiments it is required to normalise the scan profiles presented in figure 5-27 and figure 5-28 to the respective values of detection field of view and solid angle reported in Table 5-3. The normalised scan profiles are reported in figure 5-29. For a prompt photon energy threshold of 2 MeV, we obtained along the ion path, in all experiments, a net count rate per incident carbon ion, unit solid angle and unit path length of ~1×10^{-7} photons/(ion×msr×mm). For comparison, the background count rate slightly depended on the experimental set-up and was about ~$1\text{-}2\times10^{-7}$ photons/(ion×msr×mm).

As already described in section 0, in the GANIL experiment with 95 MeV/u ^{12}C-ions we tried to investigate the influence of target density and dimensions on the prompt photons yield. In figure 5-30 is shown the prompt photon scan profile obtained by inserting in the PMMA target a 2mm thick plate of bone equivalent material (PTFE ρ= 2.3g/cm^3) and a 6mm thick plate of lung equivalent material (Soft tissue ICRU-44 ρ=0.2g/cm^3). It is clearly noticeable how the prompt photon yield directly depends on the target density. Indeed a remarkable decrease of prompt photon detection is observable between 6 and 12 mm in strict correlation with the position where the lung equivalent material was inserted. The same but opposed effect is visible for the increase in photon yield between 10 and 12 mm where the bone equivalent plates were inserted. Moreover the relative lower and higher C-ion range induced respectively by the bone and lung inserts is discernable on the photon scan profile. Indeed the fall-off of prompt photon detection, which can be compared with the calculated Bragg-peak positions marked as a dashed line, take place respectively at lower and higher longitudinal positions for bone and lung insertions with respect to the full PMMA target. This demonstrates the potentially good spatial resolution which can be achieved with a collimated set-up and that can be estimated to about ~1-2mm.

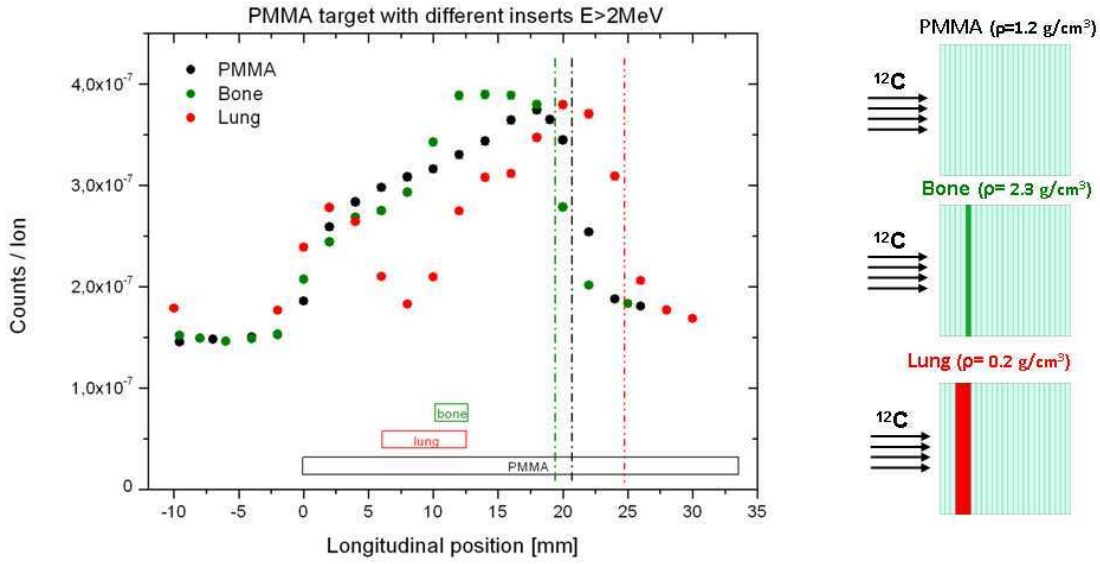

figure 5-30: Prompt photon profiles for PMMA target with different inserts: the rectangles indicate the longitudinal position of the bone equivalent (green) and lung equivalent (red) inserts. It is observed a variation of counting rates *vs* the material density and the differences on the ion range induced by the inhomogeneities can be detected. The calculated Bragg-peak position is given by the dashed vertical lines. The inset on the right shows an illustration of the target with the different material inserts. The energy selection is performed on the photon equivalent energy of the detected count.

In figure 5-31 is shown the prompt photon scan profile performed to investigate the influence of different target volumes on the photon yield. It is found that photon diffusion and attenuation in the target are directly linked to the

phantom size. In particular, the scan obtained by irradiating a big cubic water target (30 × 30 × 30 cm^3) shows that the ratio between the photon yield in the middle of the C-ion range and at the background (contrast factor) is reduced to 1.24 compared, respectively, to the 1.45 and 1.54 for the regular cubic PMMA target and the small cylindrical PMMA target (2 cm diameter – 5 cm length). These values are obtained from figure 5-31 where no energy selection on the prompt photon is applied and for a longitudinal position of 10 mm. In practice it can be assumed that, for real patient anatomy, the contrast in prompt photon detection between the region before and after the Bragg-peak would be comparable with the contrast factors we found with the cubic PMMA target (50 x 50 x 50 mm^3). Indeed the maximum reduction of the contrast factor between the small cylinder (2 cm diameter) and the big cubic water target (side 30 cm) is about 20%.

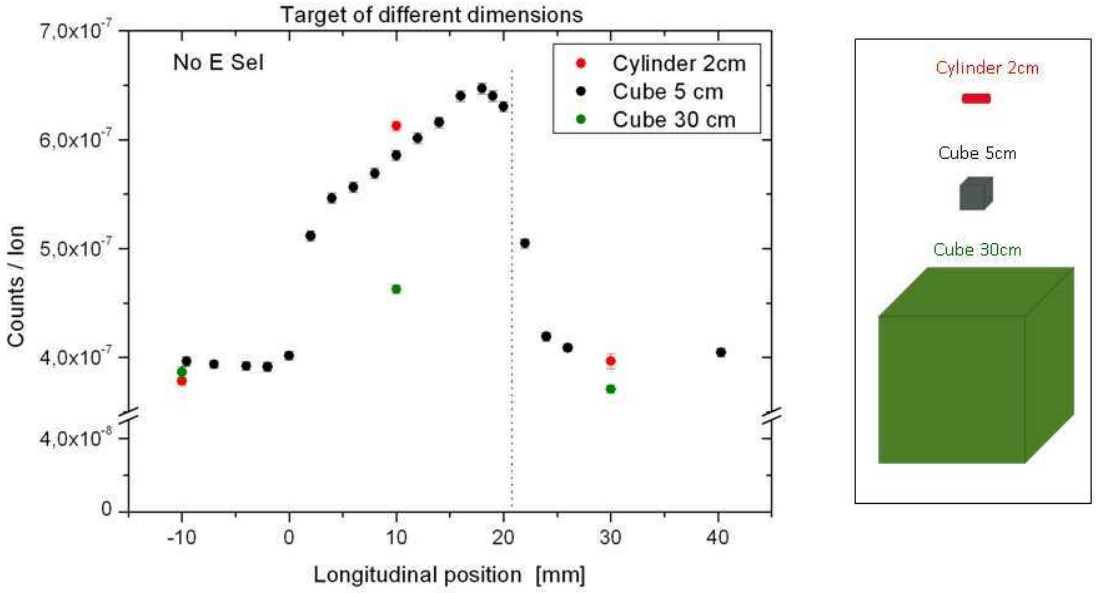

figure 5-31: Prompt photon profiles for different target volumes. The signal to background ratio decreases when the target volume increases due to the higher probability of photon scattering. The inset on the right shows an illustration of the different targets.

As already mentioned, an energy threshold on the detected prompt photons can increase the signal-to-background ratio. Indeed, as reported in Table 5-4 for the big water target, selecting photons which deposit energy higher than 2 MeV and 4 MeV, respectively leads to an increase of contrast factors by 24 % and 37%. Nevertheless these last two values, where an energy selection is applied, must be reconfirmed by further investigations since a slight uncertainty in the normalisation of the measurements has occurred.

Contrast factors		No E Selection Counts ×10^{-7}	E > 2 MeV_{pe} Counts ×10^{-7}	E > 4 MeV_{pe} Counts ×10^{-7}
Cylinder 2 cm	IN	6.11	3.78	1.35
	OUT	3.96	1.70	0.64
	Contrast factor	**1.54**	**2.22**	**2.11**
Cube 5 cm	IN	5.86	3.13	1.21
	OUT	4.03	1.68	0.63
	Contrast factor	**1.45**	**1.86**	**1.92**
Cube 30 cm	IN	4.61	2.43	1.00
	OUT	3.71	1.58	0.59
	Contrast factor	**1.24**	**1.54**	**1.69**

Table 5-4: Achievable contrast factors on the photon scan profiles for different target size as function of the energy selection applied on the photon counts. Photons counts have detected at a longitudinal position of 10 mm (IN) and at the background level (OUT).

5.3.1.4 TOF-spectra and prompt photon scan profile comparisons between measurements and Geant4 Monte Carlo simulations

In parallel with the experimental measurements presented so far, Geant4 Monte Carlo simulations have been performed in the group in order to reproduce the measurements and to perform a benchmark of Geant4 code with measured data of prompt γ-rays created during nuclear fragment de-excitation. The details of all these simulations can be found in (Le Foulher 2010).

The experimental set-up, and in the case of GSI experiment, also the major constituents of the experimental cave (walls, target supporting table, beam dump) (Iwase et al. 2005) were reproduced in the simulations in order to realistically take into account the influence of the environment on scattering radiation.

In figure 5-32 is presented the comparison between measured and simulated TOF-spectra for the experiment performed at GSI with 305 MeV/u ^{12}C-ions. The qualitative general features of the measured spectrum are reproduced by the simulations although a large discrepancy is observed on the amount of the detected signal which is overestimated by about one order of magnitude by Geant4. Indeed in the simulated TOF spectra presented in figure 5-32 a normalization factor (~12) has been applied to all the detected photons. The structure arising just after the prompt photon peak, between 5 and 15 ns, that in measured spectra we identified, thanks to PSD, as due to photons created trough (n,γ) in the lead collimator (see section 0) is, on the contrary, attributed by the simulations directly to neutrons interacting with BaF_2 detector. At present the mismatch between the nature of the radiation composing this structure is still an unsolved issue. The second structure arising between 25 and 40 ns and which had been identified in measured TOF-spectra as due to photons diffused in the experimental cave walls, correspond in the simulation TOF-spectrum to the bump arising between 40 and 70 ns. Although at present, this delay time-shift of the simulated structure compared to measurements, has not been understood yet, is nevertheless confirmed to be mainly due to photon scattering on the floor and on the wall containing the beam dump.

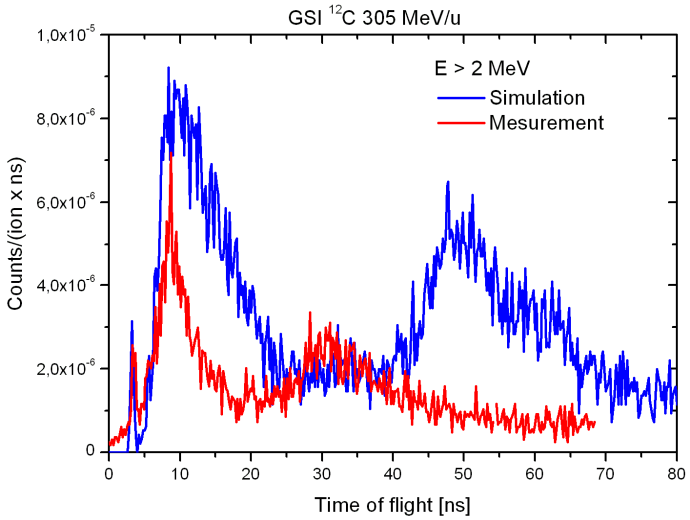

figure 5-32: Comparison between TOF spectra obtained from GSI measurements with 305 MeV/u ^{12}C-ions (as in figure 5-18) and Geant4 v9.1 simulation. In the hadronic physics list the Binary Cascade model (BC) was used. The origin of the time scale corresponds to the time when the C-ions hit the target. In the simulated TOF spectrum a normalisation factor (~12) has been applied to all the detected photons. Figure adapted from (Le Foulher 2010).

In figure 5-33 are compared the measured prompt photon scan profiles for the GANIL and GSI experiments with the simulated scan profiles obtained using the quantum molecular dynamics (QMD) model to handle the hadronic interactions. In the QMD model, the nucleus is described as a self-binding system of nucleons, which are interacting with each other through the effective interactions in the framework of molecular dynamics. One can estimate the yields of emitted light particles, fragments and excited residual nuclei resulting from the heavy ion collision. The QMD simulation describes the dynamical stage of the reactions. At the end of the dynamical stage, excited nuclei are created and must be forced to decay in a statistical way to get the final observed state (Sihver et al. 2008). The ways for de-excitation of fragments formed at the end of the intranuclear interactions depends on the energy of the projectile and they are the same for both cases analyzed here. Four competing de-excitation modes are taken into account in Geant4: (i) at low excitation energy, the evaporation decay based on the Weisskopf-Ewing model, (ii) for excitation energy above 3 MeV/u, the statistical multi-fragmentation, (iii) for highly excited light nuclei, the Fermi break-up, and (iv) the photon evaporation channel. The latter manages two kinds of decays: the continuum and discrete gamma-ray de-excitations and also the high energy photons (Le Foulher et al. 2010).

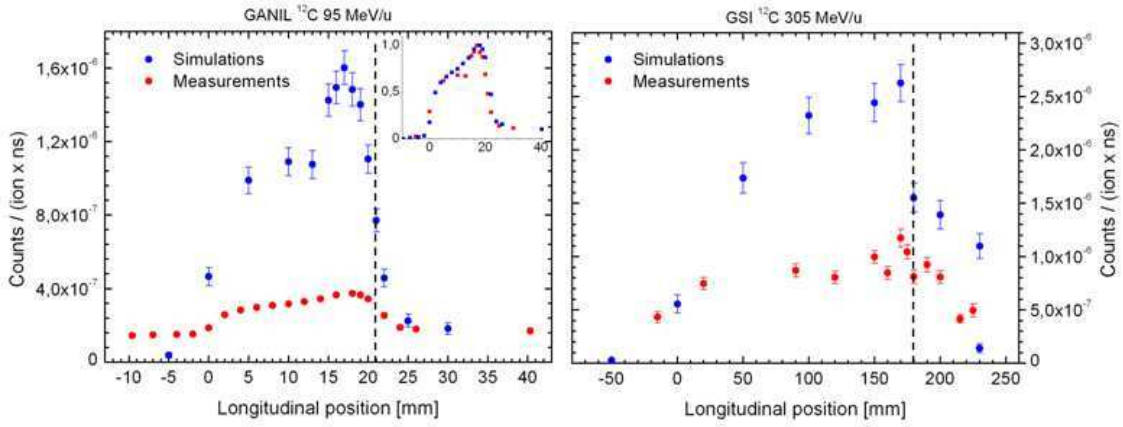

figure 5-33: Comparison between Geant4 (v.9.3) simulated and measured (as in figure 5-27 and figure 5-28) photon scan profiles obtained for GANIL and GSI experiments. In the hadronic physics list the Quantum Molecular Dynamic model (QMD) and the Fermi break-up de-excitation model were used. The calculated Bragg-peak position is given by the dashed vertical line. In the inset of the figure (left) are reported the simulated and measured profiles normalised to the maximum photon yield. The error bars correspond to the statistical errors only. Figure adapted from (Le Foulher 2010).

The comparison of the photon scan profiles presented in figure 5-33 shows that simulations performed with Geant4 v.9.3 with QMD and Fermi break-up models overestimate the detection of prompt gamma-rays by a nearly constant factor of ~5. This represents a rather good improvement compared to the simulations presented in figure 5-32 and performed with Geant4 v.9.1 and BC model where, as already mentioned, the photon yield was overestimated by a factor of ~12. It has to be noted that the fact of not reproducing in the simulations the environment of the cave (walls etc.) for the GANIL experiment plays a negligible role on the photon scan profiles which are obtained, as usual, by the integration of the detected counts under the prompt photon peak. Indeed, as clearly visible in figure 5-32, the prompt photon peak on the simulated TOF spectra is well isolated and distinguishable from the following structures induced by the delayed particles and radiation scattered in the environment. Again in figure 5-33, the enhancement of the prompt photon detection toward the end of the C-ion range and more generally the entire photon scan profiles are quite well reproduced by the simulations. This feature is highlighted in the inset on the left part of the figure where both measured and simulated profiles are normalised to the maximum photon yield. Nevertheless further developments of the models handling the hadronic interactions in Geant4 are highly desirable to finally making available a fully reliable simulation code.

5.3.2 GANIL multi-detector preliminary experimental results

5.3.2.1 Time of flight (TOF) spectra analysis

In figure 5-34 are shown the time of flight spectra for one of the LYSO detectors used in the multi-detector experiments performed at GANIL with 75 MeV/u ^{13}C-ions. In particular the spectra correspond to the LYSO medium detector that

was positioned at one of the edge of the scintillator stack (see figure 5-15). The time reference is arbitrarily set and an energy selection on the events depositing in the detector more than 2 MeV and 4 MeV (photon equivalent energy) is performed to obtain the TOF spectra represented by the red and blue curves respectively. The most distinguishing feature of these LYSO TOF-spectra compared to BaF_2 TOF-spectra presented in figure 5-17 and figure 5-18 is the lack of any other detailed structures except the prompt photon peak arising from 6 to 10 ns. Indeed the small dimensions of LYSO scintillators lead to little detection efficiency for scattered background radiation.

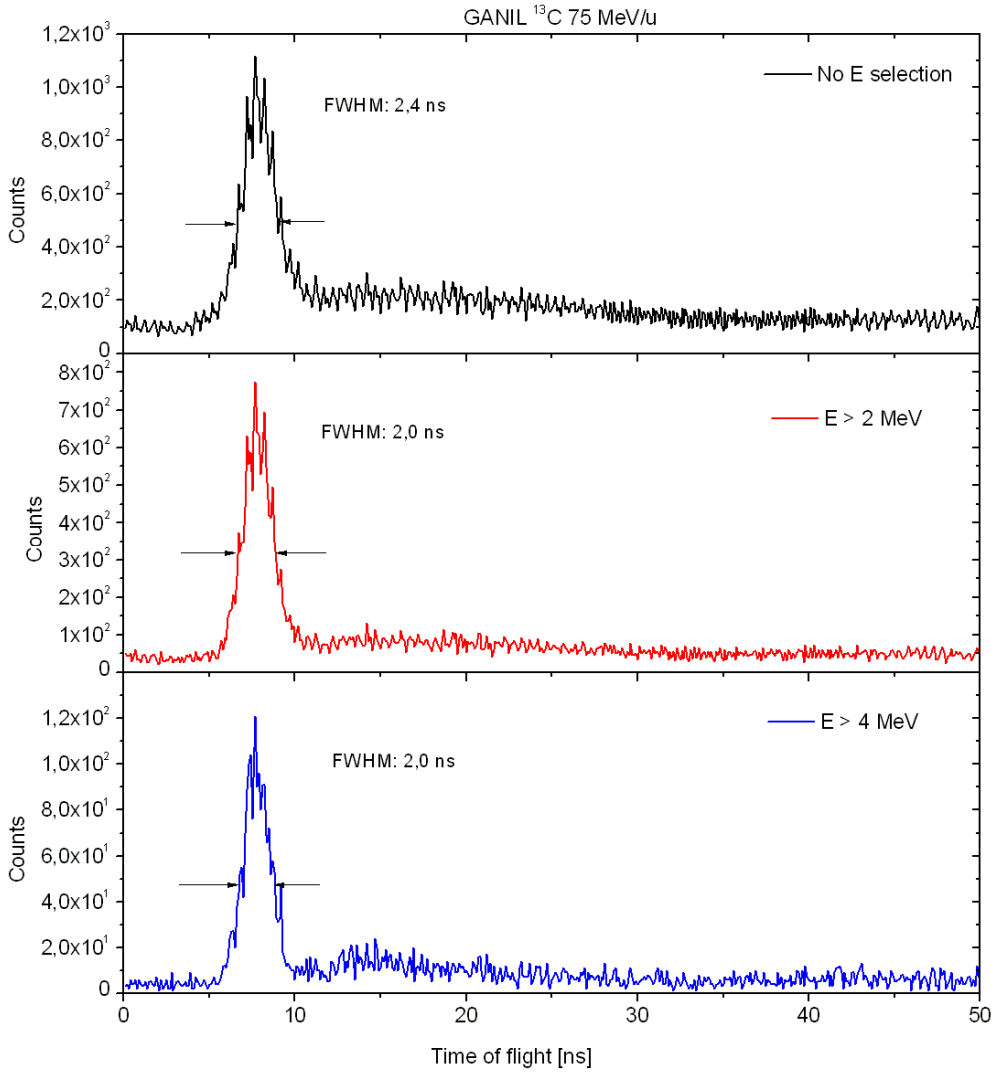

figure 5-34: Time of flight spectra for one of the LYSO (medium) detectors employed in the GANIL experiment with ^{13}C ions of 75 MeV/u. Red and blue spectra are obtained by selecting the events which deposit in the detector more than $2MeV_{pe}$ and $4MeV_{pe}$ respectively. Spectra are obtained with the collimated detector looking at a target penetration depth of 10 mm. The origin of the time scale is arbitrarily set. The bin width is 0.2 ns.

Nevertheless, as can be noted from the energy TOF spectrum reported in figure 5-35, an energy selection above 2 MeV still improves the signal-to-background ratio. If compared to all the detected events, prompt photons which deposit more than 2 MeV in the LYSO detector accounts for 30% of the entire signals.

For GANIL and GSI TOF-spectra presented in figure 5-17 and figure 5-18 this same value was respectively 5% and 2%. Therefore an increase of about one order of magnitude on the signal to background ratio is achieved with the small volume LYSO detectors compared to BaF_2 where more than 95% of its 1 litre volume detected only background.

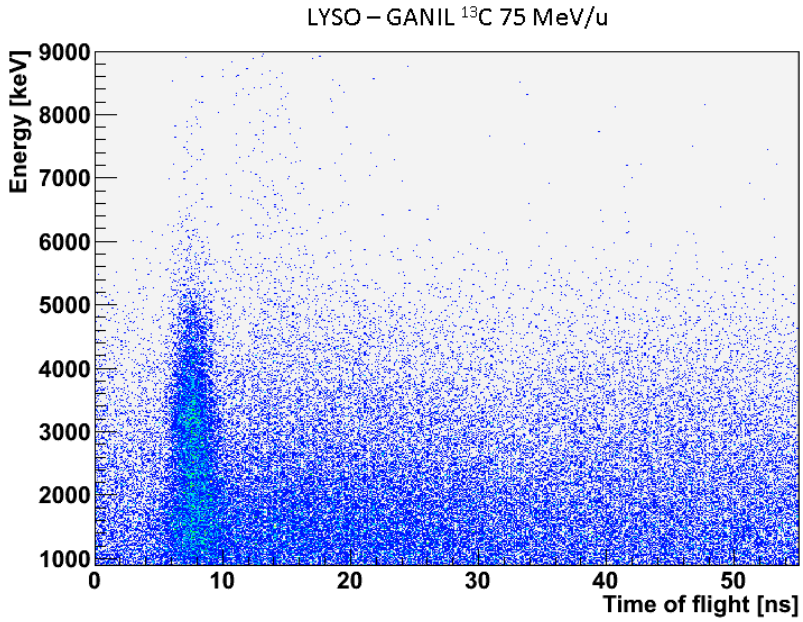

figure 5-35: Two-dimensional spectrum of the energy deposited in one of the LYSO (medium) detectors as function of TOF. The spectrum was obtained at GANIL with 75 MeV/u ^{13}C-ions and the collimated detector looking at a target penetration depth of 10 mm. The origin of the time scale is arbitrarily set. The energy axis is calibrated for photons.

5.3.2.2 Multi-detector prompt photon scan profiles

The preliminary series of prompt photon scan profiles presented in figure 5-36 were obtained by integrating the counts detected by the LYSO scintillators in the prompt photon peak of TOF-spectra (see figure 5-34) at various longitudinal positions. The PMMA target was translated in front of each of the four stacked detectors to allow a full scan of the entire C-ion range and then, the longitudinal position axis was rescaled in order to make position 0 to correspond to the target entrance.

A clear correlation is observed between the ion path and the photon production yield and a decrease by at least a factor of about 2 (contrast factor) is seen close to the Bragg-peak position for each scan measurement. If we consider the single LYSO detector which was positioned opposite to the stack of the four LYSO scintillators, its contrast factor is respectively 4.8 with no energy selection (see figure 5-36) and 7.5 with an energy selection E > 2 MeV on the detected prompt photons (scan not shown). These values have to be compared to the contrast factors achieved with the single BaF_2 and reported in section 0, which were respectively 1.5 with no energy selection and 2.0 with an energy selection E > 2 MeV. The increase of the contrast factors with LYSO detectors compared to BaF_2 scintillator is due to the much better signal to background ratio obtained with the small LYSO scintillators which has already been reported in the previous

paragraph. In the case where no energy selection is performed in the off-line analysis, what determines the minimum detectable photon energy is the constant fraction discriminator (CFD) threshold which was set for all the experiments to about 800 keV photon equivalent energy.

Nevertheless, still on figure 5-36, the average contrast factor for the stacked LYSO detectors is about ~2 with no energy selection and about ~3 with an energy selection E >2 MeV (not shown). The decrease in the contrast factor for the LYSO scintillators from the single-detector configuration to the stack of four detectors is due to "photon crosstalk", i.e. the multiple detection of photons scattering from one detector to the neighbouring ones. As already mentioned, these are still preliminary results and some further considerations about the quantification of the cross-talk probability as function of the detector thickness and position may be found in (Constanzo 2010).

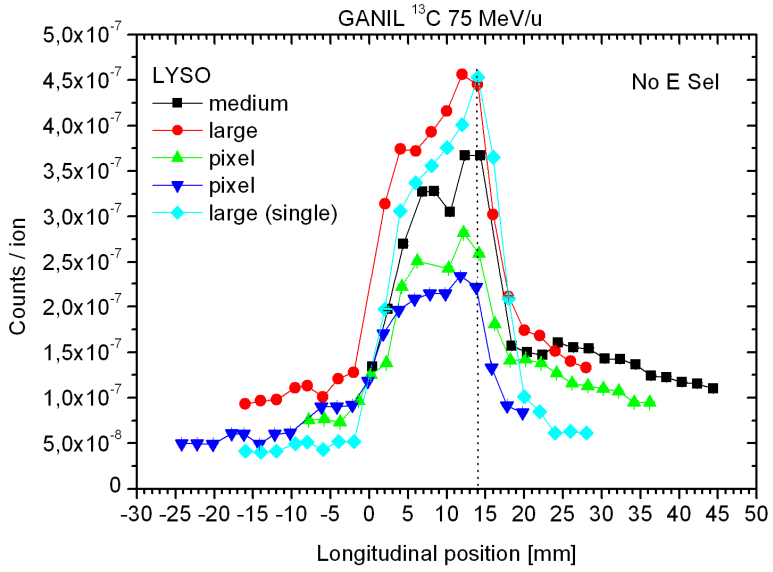

figure 5-36: Prompt photon scan profiles for the multi-detector experiment performed at GANIL with 75 MeV/u ^{13}C-ions. Position 0 corresponds to the target entrance. The calculated Bragg-peak position is given by the dashed vertical line.

Although the contrast factor is almost constant for each of the four stacked LYSO detectors, the absolute detected photon yield inside and outside the C-ion range largely depends on the specific scintillator. This is partly due to the intrinsic difference in detection efficiency due to the different crystal volumes and to photon crosstalk probability which depends on the number of neighbouring detectors, but secondly and most importantly, it depends on practical drawbacks of the technique we used to assemble the detectors which leads to scarce control of the tightness of the contact between the light-guide and PMT that brings poor reproducibility of detector performances. It is anyhow clear, that the gain in the contrast factor that can be achieved reducing the detector volumes is somehow faded by the increase of radiation cross-talk. Nevertheless a still acceptable contrast factor of ~2 was obtained in this preliminary experiment without any specific optimisation of the detection set-up to reduce photon cross-talk.

A second major difference between the scan profiles obtained with the large BaF_2 detector and the stack of LYSO scintillators arises on the TOF selections which have to be performed to obtain a photon scan profile correlated with the C-ion range. As shown in figure 5-37, the six times larger signal to background ratio which can be achieved with the small LYSO detectors compared to the large BaF_2 scintillator allows to not make any prompt photon selection on the TOF spectra and still produce scan profile correlated to C-ion range. This finding was completely impossible to achieve with the BaF_2 detector where, as shown in figure 5-27, with not TOF selection, a scan profile completely flat and therefore uncorrelated to C-ions range was obtained. Nevertheless the use of time-of-flight is still unavoidable to achieve exploitable contrast factors and acceptable spatial resolution. Indeed average contrast factors of only ~0.3 are found in figure 5-37 whereas the spatial resolution which could be reasonably assumed on the order of 2-3 mm in figure 5-36 degrades by about a factor of two in the scan of figure 5-37.

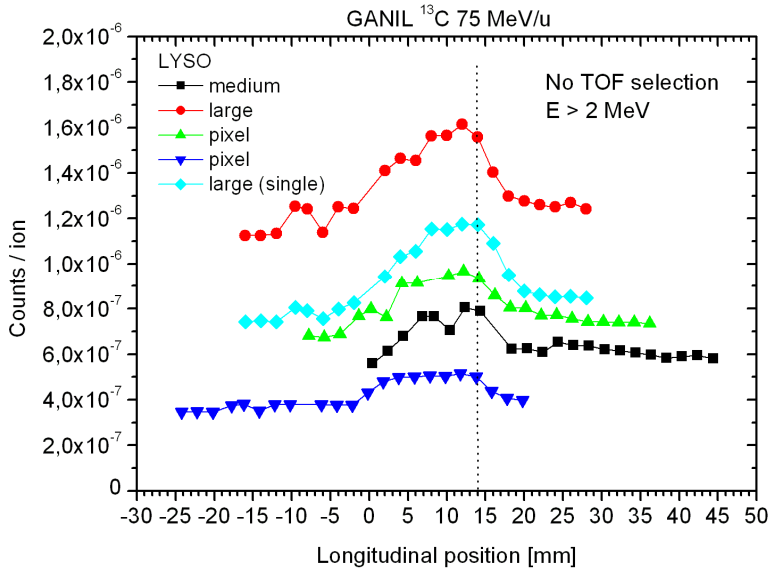

figure 5-37: Scan profile for the multi-detector experiment performed at GANIL with 75 MeV/u ^{13}C-ions obtained with no selection on the TOF spectra. The calculated Bragg-peak position is given by the dashed vertical line.

5.4 Conclusions and perspectives

The major requirements on the measured γ-ray profiles are a spatial resolution of about 1-2 mm and a clear difference between the region before and after the Bragg-peak. Based on the results of the present work, prompt photon detection appears a promising technique to be used for real-time ion-range monitoring. Indeed, as shown in figure 5-29, for a prompt photon energy threshold of 2 MeV, we obtained along the ion path, in both experiments, a net count rate per incident carbon ion, unit solid angle and unit path length of 1×10^{-7} photons/(ion×msr×mm). Based on this detected value, if we consider as an example a patient treatment plan in which 7×10^{8} carbon ions are required to deliver an absorbed dose of 1 GyE to a tumour volume of 120 cm^3, divided in 39 slices each 3 mm wide (M. Krämer et al. 2000), there are on average 1.8×10^{7}

carbon ions per slice. According to the above-mentioned values we would obtain, as reported in Table 5-5, with the single BaF_2 detector as used in the present experimental configuration and a photon threshold of 2 MeV, about 7 γ-counts within and 3 γ-counts outside the ion-path for the GANIL scan shown in figure 5-27, while we would obtain about 20 γ-counts within and 7 γ-counts outside the ion path for the GSI scan with 305 MeV C-ions shown in figure 5-28. Assuming a uniform distribution of C-ions in the tumour volume it's a first round approximation to estimate the number of photons potentially detectable per tumour slice. Indeed, for some clinically applied particle delivery techniques, about 90% of the delivered spots have a weight of ≤ 10% of the maximum weight in any individual field (Lomax et al. 2004). In practice, this would mean, that with a collimated gamma camera, it would be easier to perform range verification of the most distal energy slices for which the relative dose is higher than all the successive proximal energy slices. We remind that the signal-to-background ratio measured in the present case was not optimized: more than 95% of the 1 litre volume of BaF_2 detected only background, which required a large quantity of lead shielding to be used, which in turn created a high neutron and gamma background.

		Measured counting rates [counts/ion]	Estimated photon Counts/Slice
GANIL 95 MeV/u ^{12}C-ions	Inside ion path	4×10^{-7}	**7.2**
	Outside ion path	1.5×10^{-7}	**2.7**
GSI 305 MeV/u ^{12}C-ions	Inside ion path	1.1×10^{-6}	**19.7**
	Outside ion path	4×10^{-7}	**7.2**

Table 5-5: Estimated photon counts per tumour slice based on measured counting rates with a single BaF_2 detector and a 2MeV energy threshold applied over detected photons. The estimation is performed for a typical clinical case in which 1 GyE dose is delivered to a 120 cm^3 tumour volume (M. Krämer et al. 2000).

The discrimination between prompt photons and background radiation made with time-of-flight represents the main characteristic of our experimental set-up and it avoids the use of bulky neutron shielding. This feature is of particular importance since it permitted to significantly reduce the size of the shielding material (E. Testa et al. 2009) allowing a preliminary experimental set-up with stacked multi-detectors as it was presented at end of the chapter. Furthermore, TOF technique allowed demonstrating the correlation of the prompt photon production and the primary ion path while great insights to better understand the photon and neutron contribution in TOF spectra was brought by the PSD technique applied to neutron scintillator BC501.

Although we used high neutron detection efficiency BC501 scintillator with a specific paraffin collimation to investigate a possible prompt neutron component correlated with the ion range, no such correlation was found. Therefore, fast neutrons detected at 90° cannot be considered to provide useful information for ion range verification. However, this does not imply that

neutrons could not provide some information at a more forwarded angle, but this remains to be investigated in another study.

The investigation of the effects of target density inhomogeneities demonstrated a remarkable correlation of the prompt photon production with the target density. Moreover the relative C-ions under and over range induced respectively by the higher and lower density inserts in the PMMA target is discernable on the photon scan profile. This demonstrates the potentially good spatial resolution which can be achieved with a collimated set-up and that can be estimated to about ~1-2 mm. The investigation of the influence of the target volume on the prompt photon yield revealed that photon diffusion and attenuation in the target are directly proportional to the phantom volume and they play a significant role on the measured signal to background ratio. In particular, the scan obtained by irradiating a big cubic water target ($30 \times 30 \times 30$ cm^3) showed that, compared to the irradiation of the regular cubic PMMA target ($5 \times 5 \times 5$ cm^3), the ratio between the prompt photon yield and background photon yield (contrast factor) is reduced by about 20 % with an energy selection on photons with more than 2 MeV. Therefore, we conclude that, for real patient anatomy, the contrast in prompt photon detection between the region before and after the Bragg-peak will be adequate for ion range verification.

We demonstrated that the correlation between prompt photon scan profile and C-ion range is maintained for those high energies typical for ion therapy. Moreover, we have shown that the different beam time-structures (pulsed or continuous) do not preclude TOF measurements with sub-nanosecond precision. In case of a 'continuous' spill structure (with respect to the time scale relevant for this study, *i.e.* neglecting the beam micro-structures) the main requirement for TOF systems is to allow identification of the primary ions one by one, while in case of a pulsed spill structure the pulse duration has to be of the same order as the time resolution of TOF systems (~1-2 ns). Thus, our technique may be applicable both at cyclotrons if the pulse time-length is about 1 ns, and at synchrotrons if a detector is available that allows to trigger at particle fluencies of about ~10^8 ion/s typically used in C-ion therapy (Peters et al. 2008). Such a detector (hodoscope) could be made of scintillating fibres (Achenbach et al. 2008) or synthetic diamond (Rebisz et al. 2006) and both types of such hodoscopes are currently being developed at our laboratory.

The preliminary results with the multi-detector set-up have shown that a clear correlation is observed between the ion path and the photon production yield for each of the stacked LYSO detectors. Moreover, the ratio between prompt photon signal over all the detected events in the TOF spectra is about ~6 times higher than what it could be achieved in the same experimental conditions with the BaF_2 scintillator. This leads to an increase of about a factor of ~3 on the contrast factor of the photon scan profiles obtained with a single LYSO scintillator compared to the single BaF_2 detector. Nevertheless the gain in the contrast factor between the region before and after the Bragg-peak that can be achieved reducing the detector volumes is somehow faded by the increase of

radiation cross-talk and therefore, finally, with the actual experimental set-up, the contrast factor for each of the stacked LYSO detectors (~2) is mainly the same of the one was obtained with the single BaF_2 scintillator.

Note that the present system is based on moving the target in front of a fixed collimator. In clinical operation conditions, the gamma camera should be moveable, which is made possible by using relatively compact shielding, thanks to the TOF technique. Nevertheless, the use of several collimated detectors focussing on different positions in the patient would in principle allow detection of the dose profile along the primary ion range without moving the patient. This was not yet the case of the preliminary experiment performed with the multi-detector set-up where, for geometrical reasons, due to the still relatively large detector thickness (inter-detector distance of 8 mm) and small C-ion path (~15 mm) only two LYSO detectors were aiming at the ion path at the same time. Therefore to allow, for each LYSO detector, a complete scan of the photon profile induced by the full ion path, the target was again placed on a remotely controlled table moving along the beam axis. Nevertheless the final design of a collimated prompt gamma camera will have to be compact enough to achieve spatial resolution of about ~1-2 mm and covering at the same time, the entire photon profile induced by the full ion path. In the next chapter several geometrical configurations for both collimators and stack of detectors are systematically studied and the considerations on the main design constraints are reported.

6 Geant4 Monte Carlo simulations for the design of a multi-detector multi-collimator Prompt Gamma Camera

In order to assess the influence of the main design parameters on the efficiency and spatial resolution achievable with a multi-detector and multi-collimated Prompt Gamma Camera we performed a simulation study with a Geant4 Monte Carlo program developed in our group. A simplified set-up in which a linear source of photons replaced the prompt γ-rays produced by fragment de-excitation was reproduced in the simulations and several geometrical configurations for both collimators and stack of detectors have been systematically investigated. At the end of the chapter the considerations on the main design constraints are reported.

6.1 Application of Monte Carlo simulation codes in medical physics

Monte Carlo simulations are widespread in medical physics and several codes are available for a very broad range of applications. The most widely applied codes to conventional radiation therapy with photon and electron beams are EGS (Electron Gamma Shower) (Bielajew et al. 1994) and PENELOPE (Penetration and Energy Loss Of Positrons and Electrons) (Baro et al. 1995). Other multipurpose simulation codes like FLUKA (Battistoni et al. 2007), MCNPX (Waters et al. 2007), PHITS (Niita et al. 2006) and SHIELD-HIT (Gudowska et al. 2004) have gained high potential in particle therapy application since they handle hadronic interactions. Besides and more specifically for the field of medical imaging, dedicated Monte Carlo tools for PET and SPECT like SimSET (Harrison et al. 2002) and more recently GATE (Jan et al. 2004) are rapidly gaining interest in the nuclear medicine community.

Among all the Monte Carlo tools used in particle and nuclear physics we chose Geant4 (GEometry And Tracking) (Agostinelli et al. 2003) for its flexibility in geometry and physics modelling other than an already established expertise in the group. Geant4 has already been extensively employed in the particle therapy domain mainly to study the spatial distributions of β^+-activity produced by therapeutic beams of ^{3}He and ^{12}C-ions in various tissue-like materials for PET monitoring applications (Pshenichnov et al. 2007). In addition, more recently, a study on nuclear fragmentation reactions on extended media has been performed with the aim of analyzing the implications for ion-beam cancer therapy and shielding from cosmic radiation (Pshenichnov et al. 2010). Moreover a validation of Geant4 physics models for application in C-ion therapy has been performed (A. Lechner et al. 2010) and it showed that the positions of experimental Bragg-peaks could be reproduced within 0.2% of the particle range in water along with an accurate rendering of their full width at half maximum (FWHM).

6.1.1 A short overview of the code architecture and physical models used in Geant4

Geant4 is a C++ object oriented software based on a modular and flexible architecture letting the implementation and validation of physics processes transparent and open to users. To give an example, the way cross-sections are calculated, *via* formulas, parameterizations or interpolation of databases is exposed. In the last case the information extracted from the database is separated from the way it is accessed and used, giving the opportunity of using different databases and allowing their applicability to be tailored by particle, energy, material, etc. (Agostinelli et al. 2003). The user has ability to create a geometrical model with a large number of components of different shapes and materials, and to define ''sensitive'' elements that record the information needed to simulate detector responses (Carminati & al. 1991). To model the behavior of particles in matter a wide set of physics processes is implemented in three main domains: particle decay, electromagnetic physics and hadronic physics. The class G4Decay handles the particle and element decay according to branching ratios and models to determine the distribution of secondary particles according to default decay tables. For electromagnetic and hadronic interactions, several physics models are available in Geant4. The electromagnetic (EM) physics is divided into two categories: the standard and the Low Energy (LE) physics. In our simulations, we adopted the Standard EM Package which describes bremsstrahlung and annihilation processes for electrons and positrons other than photoelectric effect, Compton scattering and pair production for photons. Several validations of the electromagnetic physics of Geant4 (Cirrone et al. 2010) justified our choice of not employing the low energy EM physics class since standard EM provides sufficient precision for our simulation purposes. In conventional simulations for particle therapy applications, the most critical choice concerns the selection of the most appropriate hadronic physics models. As already reported above, this is not the case of the study presented here since we simulated a simplified set-up in which a linear source of photons replaced the prompt γ-rays produced by fragment de-excitation. Nevertheless, for completeness, we can mention that, for energies of interest in particle therapy, Binary cascade and Quantum Molecular Dynamics (QMD) are the most utilised models. In section 5.3.1.4 we had already briefly described both of them, while an extensive analytical and validation study of the hadronic physics of Geant4, with particular considerations for the emission of prompt radiation, can be found in (Le Foulher 2010).

6.2 Simulations of a simplified multi-collimated and multi-detector Prompt Gamma Camera

6.2.1 Basic principles of collimator design

In nuclear medical imaging, especially prior the widespread diffusion of PET tomographs, γ-cameras, also called scintillation cameras or Anger cameras (Anger 1964), were common devices used to image γ-rays emitted from radioisotopes combined with pharmaceuticals (to form radiopharmaceuticals) and are still of some usefulness in the diagnostic exams where the expense and resource implications of a PET scanner cannot be justified. Gamma cameras are employed in two main diagnostic techniques called scintigraphy and single photon computed emission tomography SPECT. Both applications are based on the internal uptake of radionuclides by the patient through injection, inhalation or ingestion while the emitted γ-ray radiation is captured by external detectors (gamma cameras) to provide 2D images in the case of scintigraphy and 3D images in the case of SPECT. The most common isotopes used in medical nuclear imaging are ^{133}Xe (γ-rays 81 keV), ^{67}Ga (γ-rays 93-185-300 keV), ^{123}I (γ-rays 159 keV) and ^{18}F (γ-rays 511 keV). A technique to correlate the detected photons with their point of origin is thus required in order to obtain some spatial information about the emission points of detected γ-rays. Therefore the most conventional method is to place a collimator in between the imaging subject and the camera detectors. In figure 6-1 is illustrated a selection of the main types of collimators which are employed in Anger cameras classified on the type of their focusing (Saha 2006). Pinhole collimators are made in conical shape with a single hole and are used in imaging small organs such as the thyroid glands to provide magnified images. Converging collimators are made with tapered holes converging to an outside point and are employed to provide magnified images when the organ of interest is smaller than the size of the detector. Diverging collimators are constructed with tapered holes which are divergent from the detector face and are used to image organs such as lungs that are usually larger than the size of the detector. Therefore, as can be noticed from the diagrams of figure 6-1, images are magnified by converging collimators and minified by diverging collimators. Parallel-hole collimators are made with holes that are parallel to each other and perpendicular to the detector face. Depending on the collimator design the shape of the holes can change from hexagonal, triangular or square while their number usually ranges between 4000 and 40000. These collimators are the most commonly used in nuclear medicine procedures and furnish a one-to-one projected image. Because pinhole and converging collimators magnify and diverging collimators minify the image of the object, the gamma camera response is no longer translationally invariant and some distortions occur in images obtained with these collimators which therefore lead, for example, to SPECT reconstruction methods that are much more complicated than in the case of parallel-holes collimators.

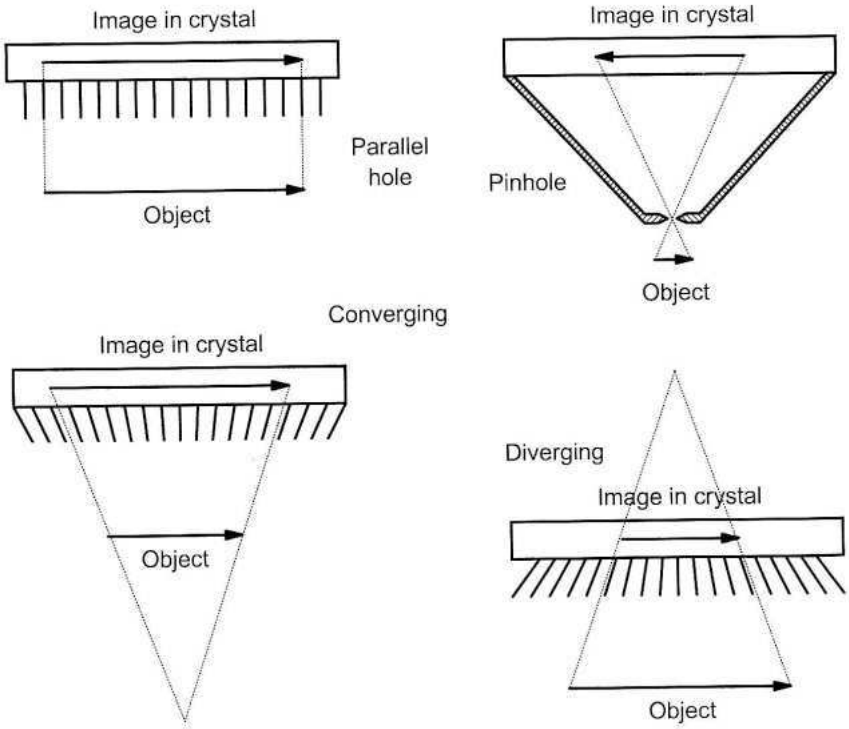

figure 6-1: Diagram of different types of collimators used for gamma camera in nuclear medicine. Figure from (Bushberg et al. 2003).

6.2.2 Description of the simulation set-up

For our multi-collimator and multi-detector prompt γ-camera we chose to adopt a parallel-slit collimator design as it is illustrated in figure 6-2. Indeed the main purpose of the camera is to detect the longitudinal position of the Bragg-peak which is by definition, point-like in the case of a single pencil beam or parallel to a given longitudinal position in the case we consider a slice of tumour treated by iso-energy C-ions. Therefore, in both cases, parallel-slit collimators, and not parallel-hole collimators will be sufficient to extract the longitudinal position of the Bragg-peak. Nevertheless, to be rigorous, both the above mentioned assumptions have to be considered in some more detail. Indeed a single C-ion pencil beam is not exactly point-like but more properly of the same dimensions of the beam focus in the axial plane and of the longitudinal spread due to range straggling or any device like a ripple filter (U. Weber & G. Kraft 1999) in the beam direction. Moreover a slice of tumour treated with iso-energy C-ions in a water equivalent reference keeps being perpendicular to the same longitudinal position in the laboratory reference only if the axial inhomogeneities encountered by the C-ions before their stopping points are negligible. Otherwise any iso-energy slice in the water reference will turn out to be tilted or deformed in the laboratory reference. This last point has not been yet investigated in the current study but to mitigate both the above mentioned effects, as already introduced in section 4.2.1, a hodoscope could provide the information on the transverse position of the beam which can therefore be in principle correlated with the possible axial inhomogeneities encountered by the C-ions.

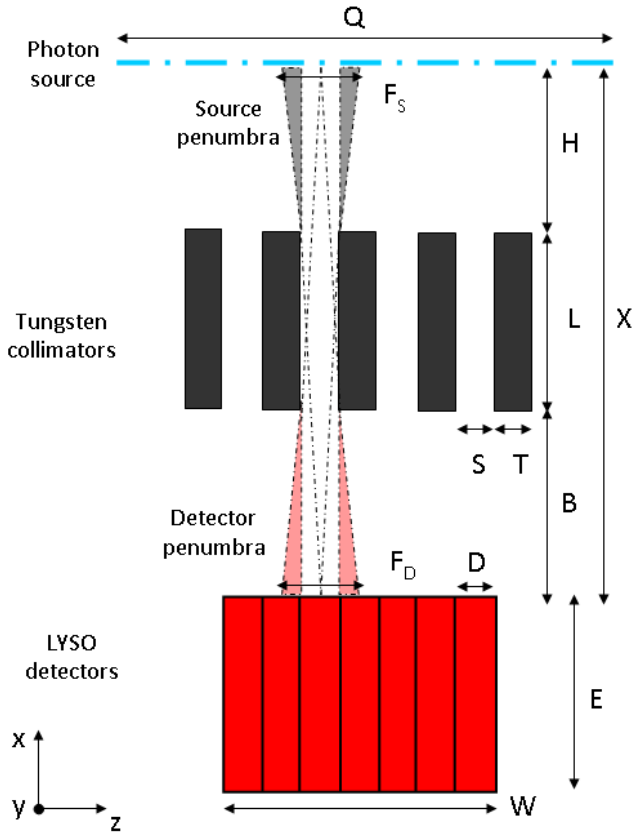

figure 6-2: Diagram of the multi-collimator and multi-detector simulation set-up. F_S and F_D represent respectively the source and detection field of view including the source and detection penumbra marked as gray and pink shadowed area.

As can be seen from figure 6-3, a simplified set-up in which a linear source of photons replaced the prompt γ-rays produced by fragment de-excitation was reproduced in the simulations along with the multi-collimator and the stack of LYSO detectors. As already mentioned, in order to assess the influence of each of the main design parameters on the efficiency and spatial resolution achievable with our Prompt Gamma Camera we performed a systematic study making vary mainly all the geometrical parameters presented in figure 6-2. Nevertheless some physical constraints had to be taken into account to wisely impose the variation range of the parameters under investigation. The minimum distance between the linear source of photons and the stacked of scintillators *(X)* has to be about ~60 cm to allow, in real condition, the TOF discrimination between prompt photons and background neutrons. At the same time *X* must be lower than <~100 cm to keep an acceptable counting statistics. The collimator must be made of high density and high Z-materials to allow for the largest possible photon absorption. Therefore we chose tungsten W (Z=74, ρ=19.25 g/cm^3) as collimator material. The collimator has at the same time not to be excessively heavy although allowing good photon absorption so we made *L* varying between 10 and 50 cm. The thickness of both collimator tiles *(T)* and detector crystals *(D)* has to be in reasonable accordance with commercially available products (so we chose $0.5\ mm<T<4\ mm$ and $1\ mm<D<6\ mm$). The

scintillating crystal must have an intrinsic high photon detection efficiency and good time resolution so LYSO detectors have been chosen. Finally, since the computational time depends also on the size of simulated set-up, a reduced scale camera of 20 cm length *(W)* and 5 cm height *(Y)* has been simulated.

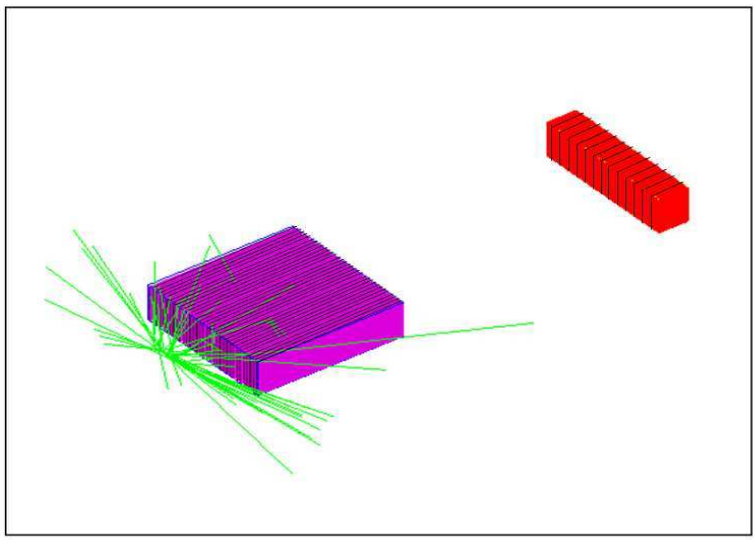

figure 6-3: Screenshot of the graphical representation of the simulation detection set-up. From left to right are shown the isotropic linear source of photons (green), the multi-collimator (purple) and the stack of LYSO detectors (red).

The main difference between Anger camera used in traditional nuclear medicine imaging and our prompt gamma camera rests on the energy of the incident radiation. Indeed, while for traditional gamma camera the photon energy is precisely known (fixed by the radioisotope contained in the pharmaceutical tracer) and mainly never exceeds 511 keV, in our case the prompt γ-rays energy spectrum is extremely broad rising up to energies higher than 10 MeV as can be seen from the energy spectrum presented in figure 6-4. Here it is reported the simulated energy spectrum of prompt γ-rays produced in 4π steradians by fragment de-excitation created during the interaction of 310 MeV/u ^{12}C-ions fully stopped in a water target (Le Foulher 2010). The two characteristics emission peaks at 4.44 MeV from ^{12}C and at 6.13 MeV from ^{16}O (Polf, Peterson, McCleskey et al. 2009) are clearly visible. This energy spectrum has been fitted with the exponential fit reported in the inset of figure 6-4 and which has therefore been used in our simulation as generator of the energy distribution of the γ-rays emitted by the linear photon source. As it is shown in more details in (Le Foulher 2010), it can be noted that the energy spectrum of prompt γ-rays produced by C-ion fragment de-excitation is rather independent from the primary carbon beam energy and therefore the choice of using in our simulation the energy spectrum of photon produced by a single C-ion energy (310MeV/u) seems justified.

The main consequence of such a wide energy spectrum of prompt gamma rays is that the most probable interaction is Compton scattering. That is why our Prompt Gamma Camera is designed with a multi-crystal detector (as presented

in figure 6-2) instead of a scintillator block as used in gamma camera of nuclear medicine. This allows us to get rid of multiple interactions of gamma rays with the camera leading to the triggering of several crystals.

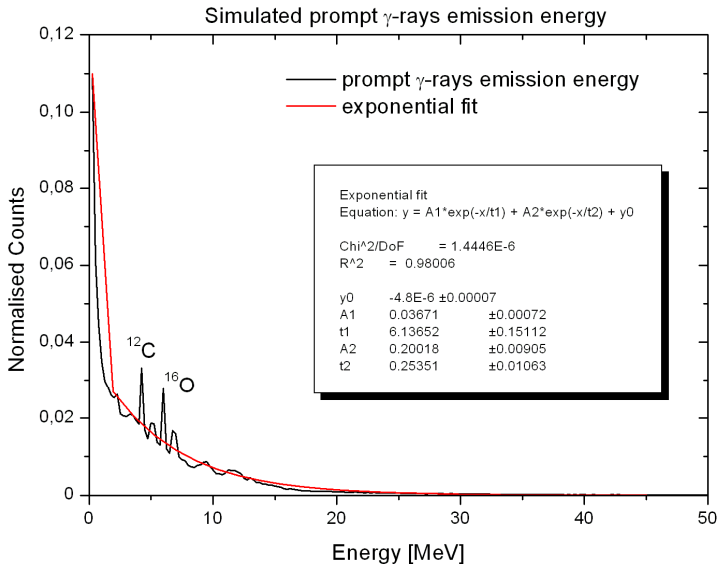

figure 6-4: Energy spectrum (black line) obtained by Geant4 simulations of prompt γ-rays emitted in 4π steradians and produced from the fragmentation of 310 MeV/u ^{12}C-ions fully stopped in a water target (Geant4 9.2 with the binary cascade model). The red line represents the exponential fit of the simulated data. Figure adapted from (Le Foulher 2010).

The LYSO detection efficiency to photons depositing more than 300 keV in the detectors has been briefly investigated for different crystal thicknesses *(E)* by simulating the interaction of a pencil beam of photons oriented parallel to the thick dimension of the crystal (E) and hitting the center of the face oriented toward the source as represented in figure 6-2. The results of these simulations are reported in figure 6-5. It can be noticed that the efficiency decreases in the photon energy range from 0.5 to 4 MeV (mainly due to the decrease of photoelectric and Compton cross sections) and it slightly increases for E > 8MeV due to the increase of pair production cross sections. Still in figure 6-5, the dot symbols represent the efficiencies calculated with monochromatic photons while the star symbols show the efficiency for photons with the energy spectrum presented in figure 6-4 which has a median energy of 2.5 MeV. In all the simulations the width of all crystals was set to 3 mm and their heights was fixed to 5 cm. As expected the thicker the crystal the higher is its detection efficiency and therefore it could be of some interest to choose the thickest possible detectors. Nevertheless some intrinsic limitation due to the internal radioactivity of LYSO crystals (which is not taken into account in these simulations) must be considered and therefore a trade-off has to be adopted between detection efficiency and background noise due to Lu decay as already presented in section 5.1.1. In any case all the simulations presented in the following are obtained with a crystal thickness *(E)* of 4 cm to allow for an easier comparison (although still not presented in this work) of the experimental

results obtained with the multi-detector experiment shown in the previous chapter and the Geant4 simulations presented here.

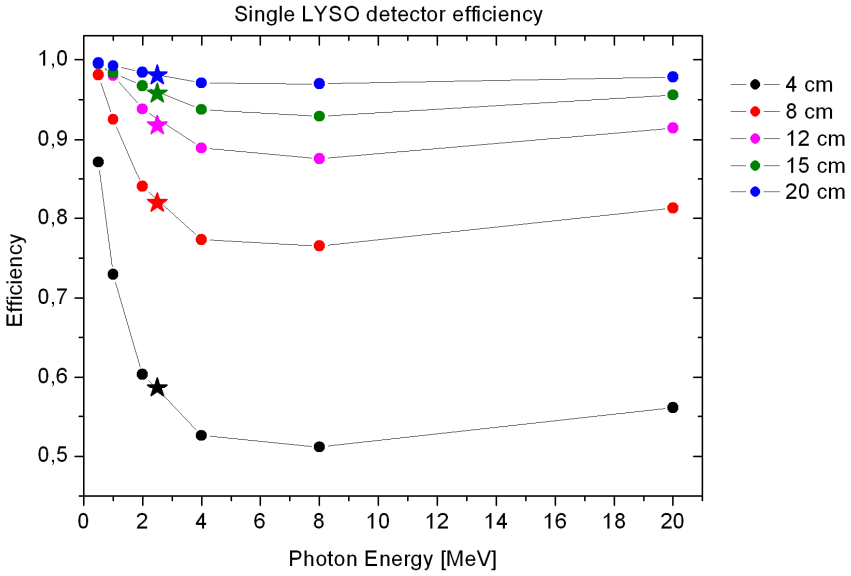

figure 6-5: Simulated detection efficiency for a single LYSO detector with different thicknesses (E). Circle points represent the efficiency for monochromatic photons and star symbols the efficiency for the photon with the energy spectrum presented in figure 6-4 with a median energy of 2.5 MeV. In all the simulation the width of the LYSO crystal was fixed to 3 mm (D) and a pencil beam of photons hit the center of the face oriented toward the source as represented in figure 6-2. The notation used to indicate the geometrical dimensions follows the one introduced in figure 6-2.

6.2.3 Basic description of collimator imaging properties

Two series of simulations have been performed with the specific aim of investigating the influence of the collimator and detector geometrical parameters on the camera efficiency and spatial resolution. Indeed it is commonly assumed that the collimator not only plays a major role in determining the spatial resolution of the camera, but it represents also the major limitation on the number of counts detected.

If we denote the average collimator efficiency as

$$\langle \$(\mathbf{r}) \rangle = \frac{[\textit{Number of counts detected from a source located in } \mathbf{r}]}{[\textit{Number of counts emitted from a source located in } \mathbf{r}]} \qquad \textbf{6-1}$$

the relationship between sensitivity and resolution can be written as

$$\langle \$ \rangle \propto R_{Cam}; \qquad R_{Cam} = fu(R_{Coll}, R_{Det}) \qquad \textbf{6-2}$$

where R_{Cam} is the total resolution of the camera provided by a function taking into account the collimator resolution R_{Coll} and the intrinsic spatial resolution of the scintillating detectors R_{Det}. At least in the ideal case in which photons are completely absorbed when they interact with a collimator wall, the source field of view F_S (as illustrated in figure 6-2) represents a good estimation of the collimator resolution R_{Coll} (Gunter 2004). In commercially available Anger camera R_{Det} is generally known and it is given, at first glance, by the pixel size

of the detectors which ranges between 2 and 5 mm. Following the same logic, in the case of our multi-slit collimator prompt γ-camera, R_{Det} can be given by the width of any single LYSO crystal *(D)* therefore, in this case, the equation 6-2 can be reduced to

$$\langle \$ \rangle \propto R_{Coll} \approx F_S \qquad \textbf{6-3}$$

It is therefore assumed that we can increase the efficiency by degrading the collimator resolution. Conversely, the camera resolution can be improved only if the efficiency is decreased. Indeed it can be understood intuitively that the efficiency can only be increased if the collimator accepts γ-rays that enter at larger angles with respect to the slit axis and thus with larger F_S.

This trade-off between <$> and R_{Coll}, obtained for the case of an ideal collimator, is generally true even for real collimators. Nevertheless, for some particular geometrical configurations which will be presented in more details in the next paragraph a more complex relationship between the efficiency and spatial resolution has been shown and it required, to be understood, to take into account not only the source field of view F_S but also the detector field of view F_D. Nevertheless it has to be reminded that all the equations presented so far do not account for the possibility for a photon to be scattered inside the collimator and further interacting with the detector. Only photons transmitted through the collimator without any interaction are counted.

A first series of simulation has been performed with a block of LYSO detector allowing an ideal infinite spatial resolution on the photon interaction points with the scintillator. Then to fully take into account the interplay effect between collimator array and detector lattice we performed more realistic simulations in which the LYSO detector has been segmented in several 'tile-shaped' small detectors stacked side by side as represented in figure 6-2. This last configuration allowed as well taking into account the photon cross-talk (scattering from one detector to the neighbouring ones) between the LYSO crystals although these results are not yet presented in this work.

6.3 Simulations results and discussion

Although we showed in the previous paragraph that detection efficiency and spatial resolution of a gamma camera are intrinsically correlated we will try to present a preliminary overview of our simulation results presenting the analysis on the influence of the main geometrical parameters of both collimators and stack of detectors separately on the efficiency and spatial resolution.

6.3.1 Influence of the collimator design on the detection efficiency

6.3.1.1 Influence of the collimator thickness and position on the visibility of the collimator slit-pattern

One of the first parameters which has to be taken into account in the design of a gamma camera is the position of the collimator with respect to the photon source, that corresponds, in the case of a real clinical case, to the distance between the irradiated region of the patient and the collimator itself. Since the patient is usually immobilized during the irradiation, we can reasonably assume that the collimator can be placed almost in contact with his skin and therefore in our simulation we made varying the gap H (see figure 6-2) between the linear source and the collimator from H = 1 cm (collimator almost in contact with the source) to $H = X\text{-}L$ (collimator toward the detector side). The results of these simulations for a 25 cm thick (L) tungsten collimator are presented in figure 6-6 for three different collimator positions. In the case where the collimator is placed toward the source it can be noticed that when a selection is applied over the photons emitted between -0.5 mm and 0.5 mm longitudinal position (black line of figure 6-6a) on the corresponding photon detection position (red line of figure 6-6a) the collimator slit-pattern becomes clearly visible. This means that, on average, in this configuration about ~50% of the photons detected between -0.5 mm and +0.5 mm were also emitted at this same longitudinal position. The remaining ~50%of photons were emitted in front of the first two neighbouring collimator slits. Indeed with such a reduced gap between collimator and γ-source (H=1 cm) the collimator slit-pattern is clearly visible on the emission position of detected photons. In other words, with the collimator placed toward the source side, a photon emitted exactly in front of one of the collimator tiles has a high probability of being absorbed and never reaching the detector provided the collimator is thick enough to not result transparent to our relatively high energy photons. On the other hand, as it is shown in figure 6-6b, if we perform a selection over the photons emitted between -0.5 mm and +0.5 mm and which will reach the detector (red curve) we noticed that the distribution of their detection position (black line) is quite broad (about ~6 mm) and it corresponds to a photon angular acceptance of ± 0.17 degree.

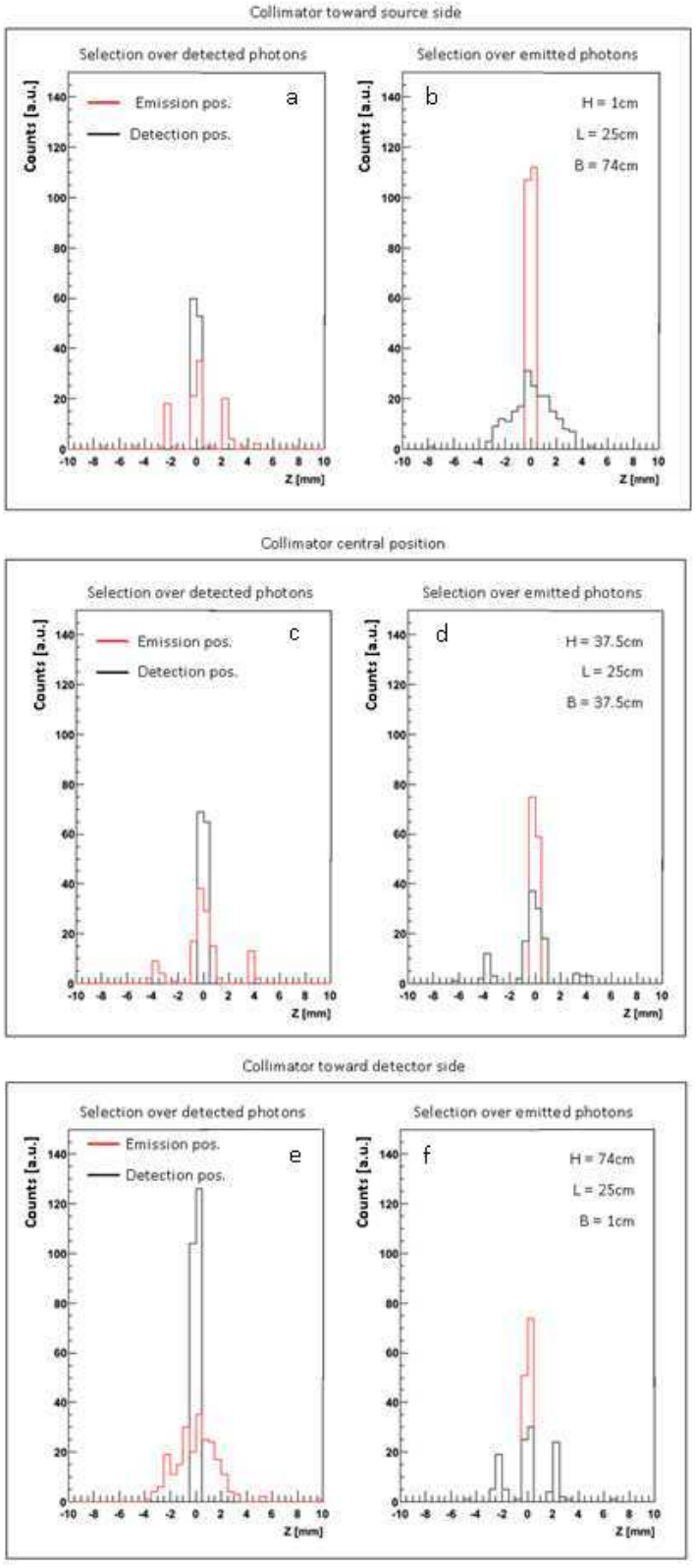

figure 6-6: Photons detection (black lines) and emission (red lines) positions obtained with a 25 cm thick collimator placed toward the linear photon source (top), at the central point between the linear photon source and the LYSO detection block (center) and toward the LYSO detection block (bottom). On the left part of the figure a selection is made over the photons detected between -0.5 mm and + 0.5 mm (black line) and their corresponding emission position is given by the red curve. On the right part of the figure a selection is made over the photons emitted between -0.5 mm and +

0.5 mm (red line) and their corresponding detection position is given by the black curve. The notation used to indicate the geometrical dimensions follow the one introduced in figure 6-2. For all the simulation S=T=1 mm. The origin of the zaxis corresponds to the central longitudinal position of the camera.

As it is shown in figure 6-7, by expanding the gap *(H)* between the source plane and the collimator, the overlapping of radiation from the adjacent slits will start shifting from the detector plane to the source plane (see figure 6-7c). Therefore the penumbral regions that in the case where *H=0* were overlapping on the detector plane (see figure 6-7a), in the case where *B=0* will overlap on the source plane (see figure 6-7c). The mirror image is found for the completely umbral region which are found on the detector plane (for *B=0*) and on the source plane (for *H=0*) and which are respectively responsible for the visibility of detector slit-pattern on the detected signal of figure 6-6f and on the emitted signal on figure 6-6a. More generally we can say that figure 6-6e-f is the mirror image of figure 6-6a-b with detected and emitted signals respectively inverted. Indeed, as the gap *(H)* increases, the slit-pattern visibility gradually decreases to a minimum and then begins to increase again.

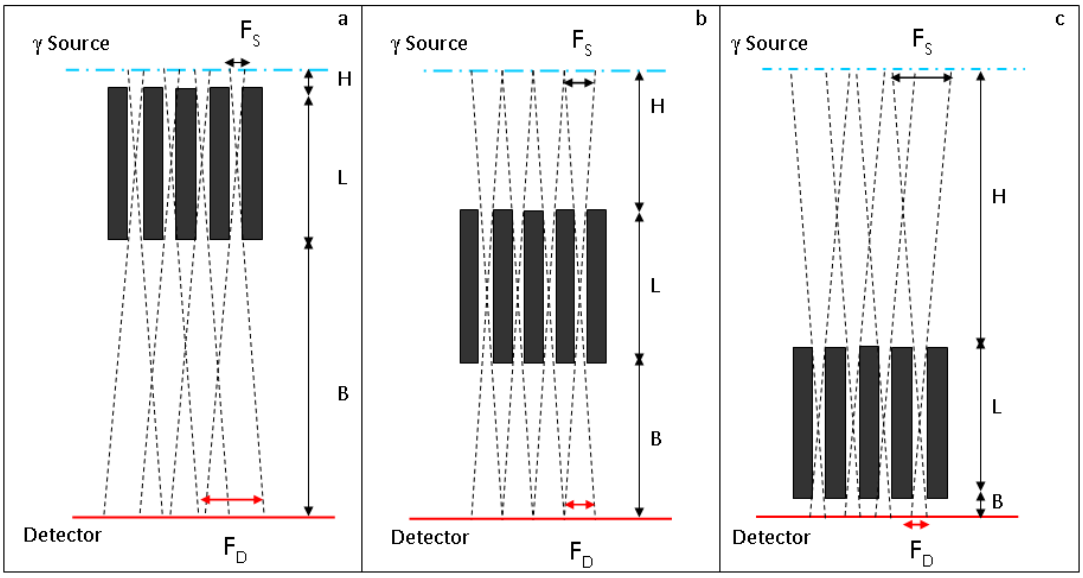

figure 6-7: Diagram showing the purely geometrical source field of view (F_S) and detector field of view (F_D) as function of the collimator position (a: Source, H≈0; b: Center, H=B=(X-L)/2; c: Detector, B≈0). The symbols used to indicate the geometrical dimensions follow the notation introduced in figure 6-2. For all the simulations X=100 cm.

Therefore, as can be seen from figure 6-6c-d and figure 6-7b the configuration where the collimator is placed in between the source and the detector plane is the less affected by the visibility of the slit-pattern. Indeed, conceptually, the slit pattern visibility is minimized if the penumbras from adjacent holes mesh exactly. To give an example based on pure geometrical calculation, in a configuration where slits and tiles are both 1 mm wide (*S*=*T*=1 mm) and in which the collimator is placed centrally in between the detectors and the source which are separated by a distance of 1 m (*X*), a tile thickness of 50 cm (*L*) is

required to satisfy the condition of perfect meshing of detector and source fields of view including their penumbras (F_D=F_S=2 mm, see figure 6-2). This last geometrical configuration has been simulated and the results are presented in figure 6-8 where it is clearly visible that no traces of slit-pattern visibility are noticeable neither on the detection nor on the emission curves. Nevertheless a collimator thickness of about 50 cm will probably be unacceptably heavy for a real clinical device, therefore it can be reasonably imagined that the overlapping of the source and detector fields of view will be an unavoidable characteristic or real collimators and therefore their influence on the achievable efficiency and spatial resolution will be investigated in more detail further in this chapter.

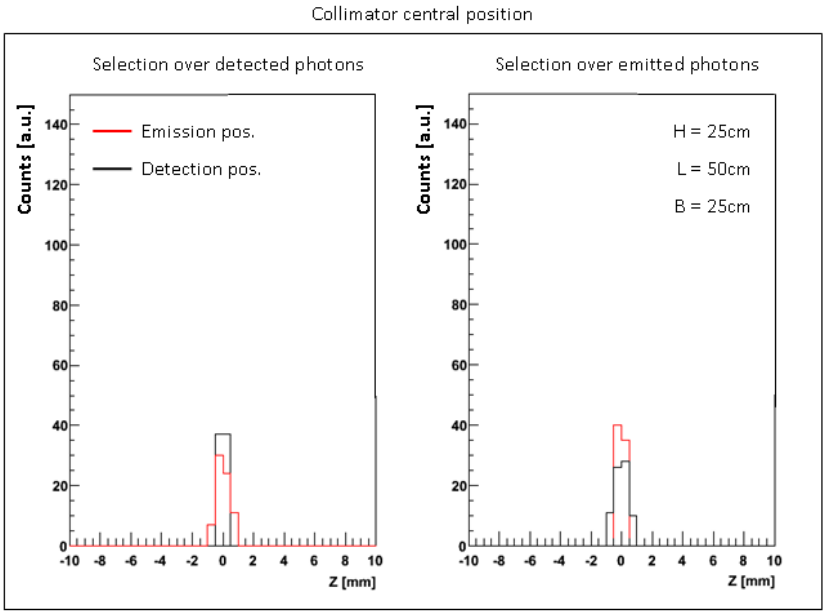

figure 6-8: Photons emission (black lines) and detection (red lines) positions obtained with a 50 cm thick collimator placed at the central point between the linear photon source and the LYSO detection block (F_D=F_S=2 mm). On the left part of the figure a selection is made over the photons detected between -0.5 mm and + 0.5 mm (black line) and their corresponding emission position is given by the red curve. On the right part of the figure a selection is made over the photons emitted between -0.5 mm and + 0.5 mm (red line) and their corresponding detection position is given by the black curve. The notation used to indicate the geometrical dimensions follow the one introduced in figure 6-2. The same number of photons is emitted as in the simulations of figure 6-6.

6.3.1.2 Influence of the collimator thickness and position on the detection efficiency

Another critical parameter for the assessment of the prompt γ-camera performances is represented by the collimator thickness which, again, has a large influence on the total efficiency of the camera.

A general formula derived from parallel-hole collimator efficiency used in conventional nuclear imaging gamma camera (Gunter 2004) can be extrapolated for our parallel-slit collimator and can be written as:

$$\langle \$ \rangle \propto \frac{S^4}{L^2(S+T)^2} \qquad \textbf{6-4}$$

where, again, <$> represents the average efficiency and *S,T* and *L* are the geometrical parameters defined as in figure 6-2. Equation 6-4 is pretty intuitive and implies the inverse proportionality between the efficiency and both the collimator thickness and the tile width. This relation has been verified by the simulations results reported in figure 6-9, where the detection efficiency is plotted as function of the collimator thickness for the case where *S*=*T*. Thus for this configuration the equation of the efficiency becomes simply proportional to the inverse of the collimator thickness <$>~$1/L^2$ and the results of the simulations follow this expression as can be seen from the fit of the data presented in the plot.

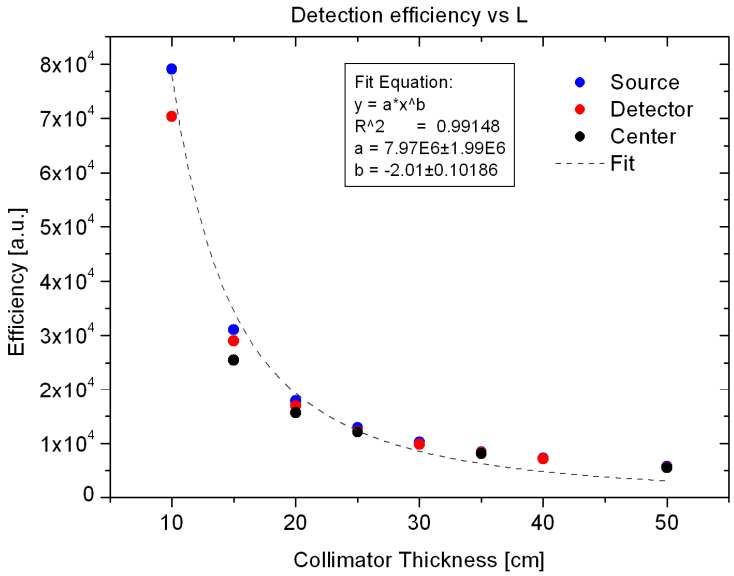

figure 6-9: Detection efficiency as function of the collimator thickness (L). Three series of simulations are plotted according to the position of the collimator with respect to the linear source of photons. The blue dots represent a collimator position next to the photon source (H=0), the red dots represent a collimator position next to the LYSO detectors (B=0) and the black dots represent a collimator position in between the photon source and the LYSO detectors (H=B=(X-L)/2). The dash line represents the fit of the data presented in the plot according to the fit equation reported in the inset. The notation used to indicate the geometrical dimensions follows the one introduced in figure 6-2. For all the simulations X=100 cm, S=T=1 mm.

Always from figure 6-9 it emerges that the collimator position has a certain influence on the overall efficiency. This characteristic is better highlighted in figure 6-10 where the efficiency is plotted as function of three detector positions for several collimator thicknesses. For all these simulations results the statistical errors are below 2%. It can be noticed that when the detector is placed centrally, in between the photon source and the detector plane, the overall efficiency is lower than the configurations where the detector is place either toward the source or toward the detectors. This behavior cannot be explained by the geometrical considerations introduced so far. Indeed equation 6-3 would predict a monotone increase of the efficiency for the increasing gap *(H)* between the collimator and photon source due to the consequent increase of the source field of view F_S. Therefore it becomes clear that also the detector penumbra F_D must be taken into account for the evaluation of the efficiency.

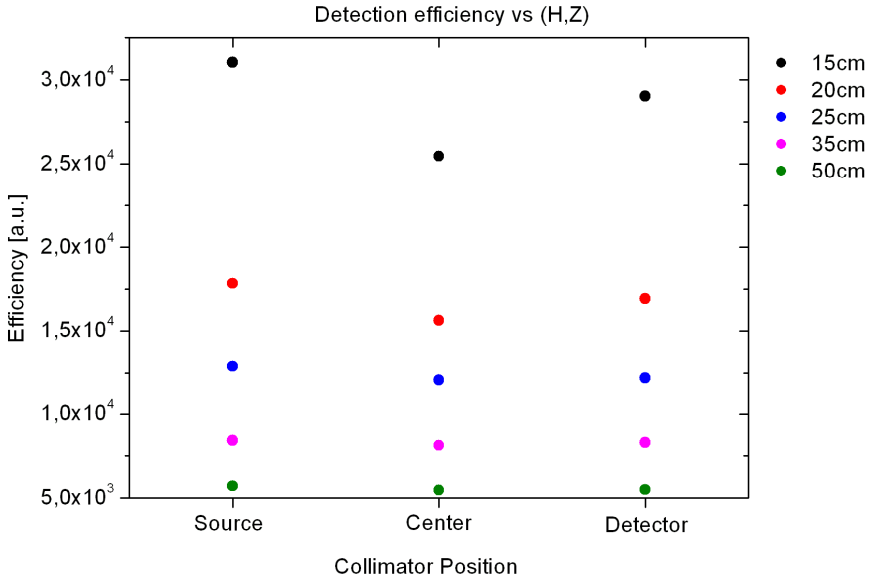

figure 6-10: Histogram of detection efficiency as function of the collimator position for different collimator depths. Collimator position Source, Center and Detector follows the same notation introduced in figure 6-9. For all the simulations X=100 cm, S=1mm, T=1mm.

One possible explanation to interpret the decrease of efficiency for collimator positions placed between the photon source and the detector plane comes from a simplified geometrical model for which, in analogy with the normalization calculation presented in section 5.2.1.1, the detection efficiency can be considered proportional to the product of the detection solid angle Ω_D and the source field of view F_S. Therefore the expression of the average detection efficiency can be written as follow

$$\langle \$ \rangle = \Omega_D \times F_S \qquad \Omega_D = \frac{F_D \times Y}{X^2} \qquad \textbf{6-5}$$

where F_S and F_D are respectively the source and detector field of view as represented in figure 6-11 and Y is the detector height which, as already mentioned, is fixed to 5cm.

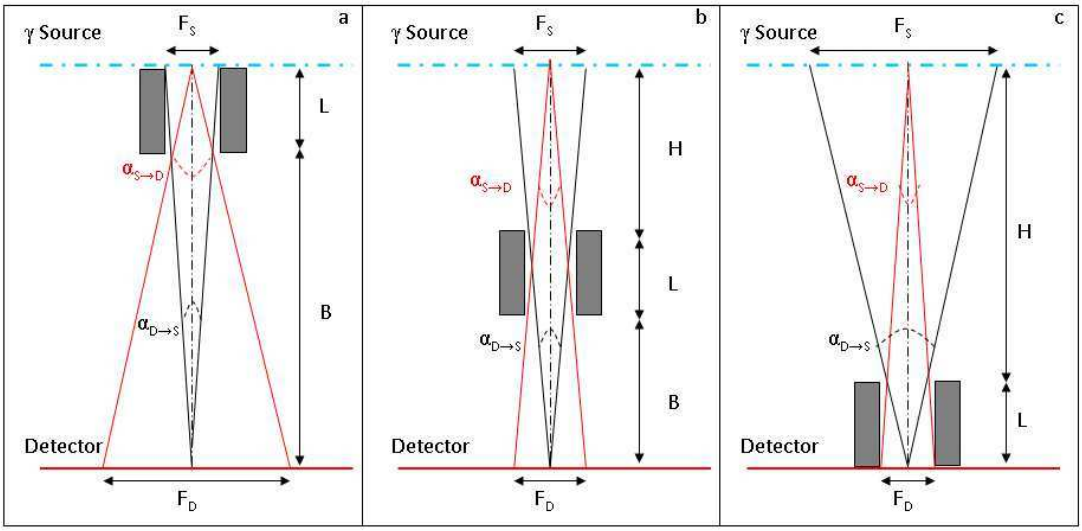

figure 6-11: Diagram showing the purely field of view for source toward detector plane (F_D) and detector toward source plane (F_S) as function of the collimator position (a: Source, H≈0; b: Center, H=B=(X-L)/2; c: Detector, B≈0). F_S and F_D arise respectively from the angles $\alpha_{D\to S}$ and $\alpha_{S\to D}$. The symbols used to indicate the geometrical dimensions follow the notation introduced in figure 6-2.

In fact, as it is shown by the dashed curves presented in figure 6-12, the product of the detection solid angle Ω_D and the source field of view F_S intrinsically depends on the collimator position and the qualitative shape of this function reproduces the concavity obtained in the distribution of the simulated efficiency as function of the collimator placement. However, this simplified geometrical efficiency (<$> = Ω_D x F_S) overestimates the decrease in the simulated efficiency as it can be seen from the u-shape of the function which is more pronounced than the distribution of the simulation values. Moreover the slight asymmetric behavior between the simulated efficiency for the detector positions toward the source and toward the detector could not be reproduced by the geometric efficiency. Therefore, although the function <$> = Ω_D x F_S can qualitatively be considered correct to explain the phenomenon of the diminished efficiency for central placed collimator, a more precise evaluation of the both detection solid angle and source field of view is necessary to allow for the quantitative reproduction of the simulated results.

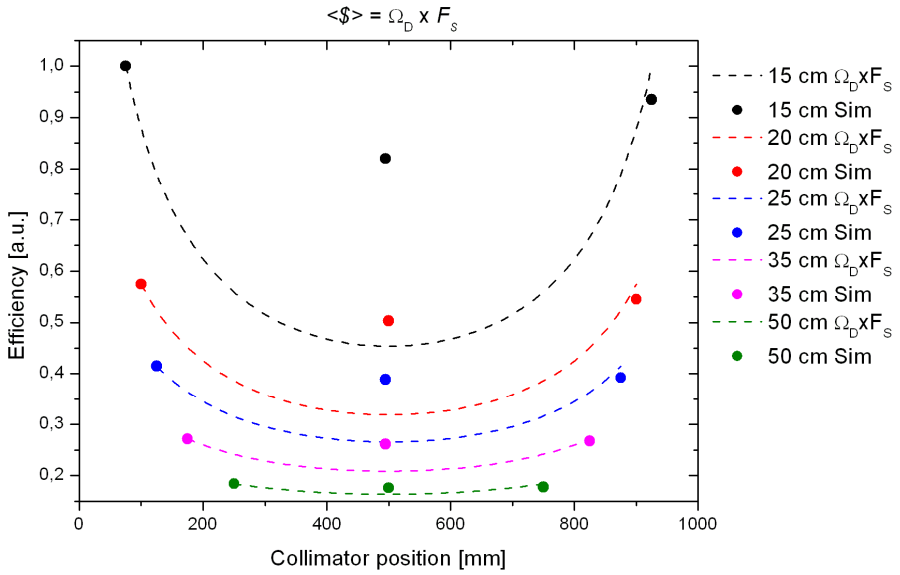

figure 6-12: Estimation of the detection efficiency as product of the detection solid angle Ω_D and the source field of view F_S. Dashed lines: geometrical calculation of the detection efficiency <$> = Ω_D x F_S. The collimator position reported on the x-axis is calculated as H+L/2. Dot symbols represent the simulated values of detection efficiency as reported in figure 6-10 and normalized to the geometrical value of Ω_D x F_S. The notation used to indicate the geometrical dimensions follows the one introduced in figure 6-2. For all the simulations and calculations X=100 cm, S=1mm, T=1mm.

6.3.1.3 Influence of collimator tiles and slits dimensions on the detection efficiency

The last geometrical parameters we investigated are the dimensions of the collimator slit and tile widths (*S,T*). Although in all the simulations we chose to adopt the same width for slits and tiles (*S=T*), we found, as can be seen from figure 6-13, that the detection efficiency is largely affected by their dimensions. More specifically the lower *S* and *T* the lower the detection efficiency (provided *L* is fixed). Furthermore, as it has already been reported in figure 6-9 the efficiency decreases with the increase of the collimator thickness. It has to be noted that in the case where the photons from the source are all emitted with a direction parallel to the collimator tiles (therefore parallel to the x-axis represented in figure 6-2) the detection efficiency remains unchanged even tough *S* and *T* vary, providing the ratio *S/T* is constant and *L* is thick enough to absorb the photons. But in the case where photons are emitted with an isotropic direction, the efficiency becomes proportional to the angular acceptance of the collimator which is as its time proportional to the ratio *S/L* (making the assumption that *S*<<*L*). Therefore, for a given collimator thickness, the detection efficiency will linearly depend on *S* (providing the ratio *S/T* is constant) as it is shown in figure 6-13. Finally, the invariance of the efficiency when a scaling factor is applied to all the collimator dimensions, which is a property usually reported in the literature (Gunter 2004), has been verified by our simulations. Indeed, we should note that if all the collimator dimensions (*S,T,L*) are multiplied by a scaling factor, the average efficiency <$>=*fu(S,T,L)* remains unchanged as can be noted from the results reported in figure 6-13 where,for example, <$>*(S=2mm,T=2mm,L=25cm)*=<$>*(S=4mm,T=4mm,L=50cm)*.

Thus, rescaling a collimator has no influence on the average efficiency provided L is thick enough to completely absorb photons. However, the same rescaling, can have a large influence on the spatial resolution as will be presented in more detail in the next paragraph.

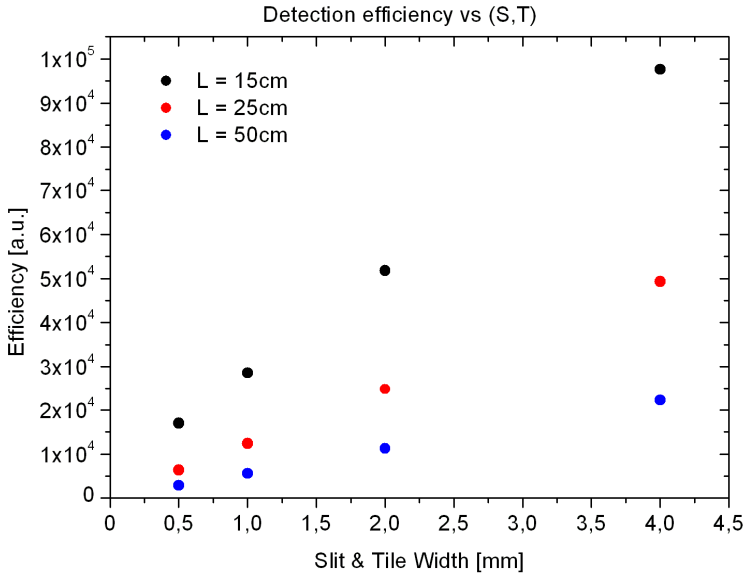

figure 6-13: Detection efficiency as function of the collimator slit and tile width (S,T). For all the simulations S=T. Three series of simulations are reported for different collimator depths (L). The notation used to indicate the geometrical dimensions follows the one introduced in figure 6-2. For all the simulations X=100 cm, H=0.

6.3.2 Influence of the collimator design on the spatial resolution

As already mentioned, to fully take into account the interplay effect between collimator array and detector lattice on the achievable spatial resolution we performed more realistic simulations in which the LYSO detector has been segmented in several 'tile-shaped' small detectors stacked side by side as represented in figure 6-2. Moreover the linear source length (Q, see figure 6-2) has been made varying from 40 mm to 60 mm by steps of 2 mm. Since the source is symmetric with respect to the center of the camera, the length variation mentioned just above leads to the translation of each edge of the source by 10 mm with steps of 1 mm.

The photon detection profiles have been recorded and fitted by a sigmoid shape error function whose equation is given by $y=a+b\,erf(c(x-d))$. Indeed the error function seems particularly adapted to fit the photon detection profiles which in the case of an ideal collimator, with no source or detector penumbra and no transversal photon tile crossing, would assume the shape of a rectangular step function with its leading and falling edges respectively placed at longitudinal position $z=\pm Q/2$. Among the four free fit parameters (a,b,c,d) d is the one which provides the position of the inflection point of the error function. Therefore we can assume that d represents a good estimation of the source edge position, or in other words, in the case of an ideal fit of a photon detection profile obtained with an ideal collimator $d=Q/2$. Nevertheless, to be rigorous, an error function

can only fit one edge at the time of a rectangular function and therefore two erf functions will be necessary to fit the photon profile. However, given the symmetry of the detection profiles, one fit is sufficient to estimate the position of the source edges.

The number of emitted photons from the linear source and by consequence, the number of the detected counts, is a critical parameter which has a large influence on both the fit convergence and the absolute errors of the free parameters. It is therefore mandatory to simulate a photon source activity which has to be reasonably comparable to the prompt photon emission rate in the case of an irradiation of a water or PMMA target with carbon ions at typical clinical doses. As already mentioned in the previous chapter, if we consider as an example a patient treatment plan in which 7×10^8 carbon ions are required to deliver an absorbed dose of 1 GyE to a tumour volume of 120 cm^3, divided in 39 iso-energy slices (M. Krämer et al. 2000), there are on average 1.8×10^7 C-ions per slice. In the simulations performed by our group (Le Foulher et al. 2010) it has been shown that on average and mainly independently on the C-ion energy, 7×10^{-3} prompt photons are emitted in 4π steradians per each millimetre of the C-ion path and per C-ion. Nevertheless, this same study demonstrated that the simulated prompt photon detection was overestimated by a factor of about ~12 as compared with the experimental measurements. Therefore, we can estimate in 6×10^{-4} γ/(mm×C-ion) the real amount of prompt photons emitted per millimetre of the C-ion path and per C-ion. Finally we can thus assume that 1.1×10^4 prompt photons are emitted in 4π steradians per each mm of C-ion range for a typical dose delivered to any tumour slice (~26 mGyE) or, in other words, each iso-energy C-ions spill of 1.8×10^7 C-ions delivers on average 26 mGyE and produces 1.1×10^4 γ/(mm). As already mentioned, considering that each iso-energy spill, contains the same number of ions is somehow a gross but in our case conservative approximation since for some delivery techniques, about 90% of the delivered spots have a weight of ≤ 10% of the maximum weight in any individual field (Lomax et al. 2004). Nevertheless, we set the activity of our linear source of photons to the value of 5.05×10^3 γ/(mm) emitted only in the 2π steradians including the collimated camera.

The reduced dimensions of the simulated camera (a detector height of 5 cm positioned at 60 cm from the source covers only 1.3% of the total azimuth) and the relative low linear intensity of the photon source lead however to very low detected statistics. Therefore the first series of simulations have been performed with a photon source one hundred times more intense (5.05×10^5 γ/(mm)), thus, to give an example 2.53×10^7 photons have been emitted in 2π sr in the case where *Q=50 mm*. As a first approximation we can consider that increasing the source activity by a factor of one hundred is equivalent to let the linear source activity unchanged but multiplying by the same factor (100) the number of collimated detectors which would ideally be placed on a ring around the linear source.

6.3.2.1 Influence of the collimator position on the spatial resolution

In figure 6-14 are shown the detection profiles for three different source lengths (44 mm, 50 mm and 56 mm) obtained with a collimator whose slits and tiles are 2 mm wide. Each bin of the photon profile represents the counts detected by a single LYSO detectors, moreover the bin width corresponds to the width of the LYSO crystal *(D=2mm)* and the bin position is centered on the longitudinal position of each tile shaped detector. The reported photon counts have been detected with a configuration equivalent to a ring of 100 collimated detectors. For sake of simplicity the fit has been performed only on the right edge of the detection profile. On the left part of the spectrum, the leading edges of the photon profiles, which should be separated by 3 mm, are reasonably distinguishable. Moreover, for the three cases, the position of the fit inflection points estimates the real source edge positions with a maximum error of ~10%.

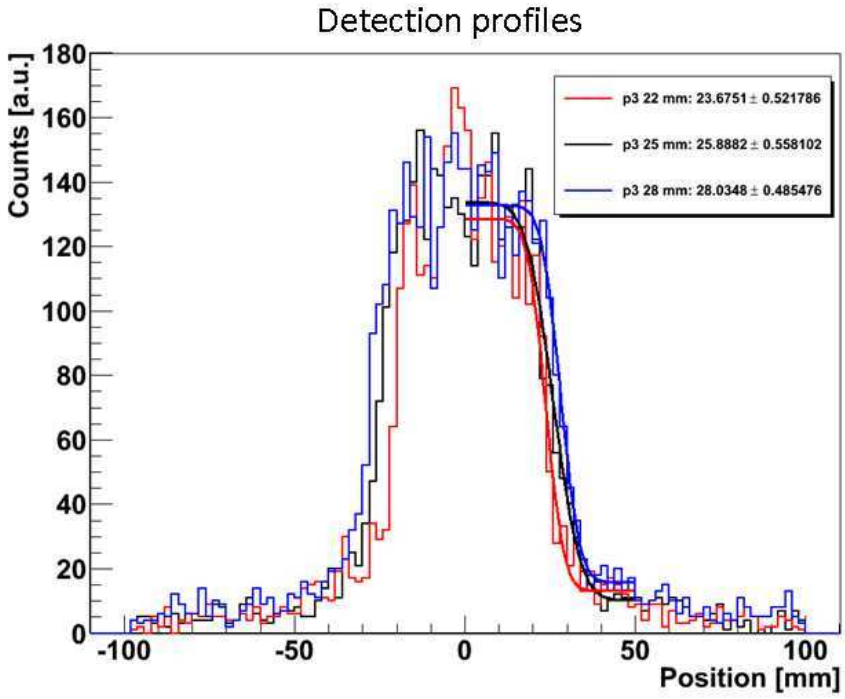

figure 6-14: Detection profiles for three different linear source lengths (Q) 44 mm (red line), 50 mm (black line) and 56 mm (blue line). The fit curves are performed with the function y=a+b·erf(c(x-d)). In the inset are respectively reported the position of the source edge (Q/2) and the value of the fit parameter d with its absolute error. For all the simulations S=T=2 mm, D=2 mm, H=5 cm, L=20 cm, B=35 cm. The reported photon counts have been detected with a configuration equivalent to a ring of 100 collimated detectors. The notation used to indicate the geometrical dimensions follows the one introduced in figure 6-2.

In figure 6-16 are displayed the curves of the fit inflection points plotted against the real source edge position for the linear source length *(Q)* varying from 40 mm to 60 mm by steps of 2 mm (which means that each source edge translates by 10 mm by steps of 1 mm with respect to the center of the camera). Moreover, to investigate the influence of the collimator position on the spatial resolution, three different configurations with the collimator *(L=20 cm)* placed respectively

toward the source, in central position between source and detectors, and toward the detectors have been systematically simulated.

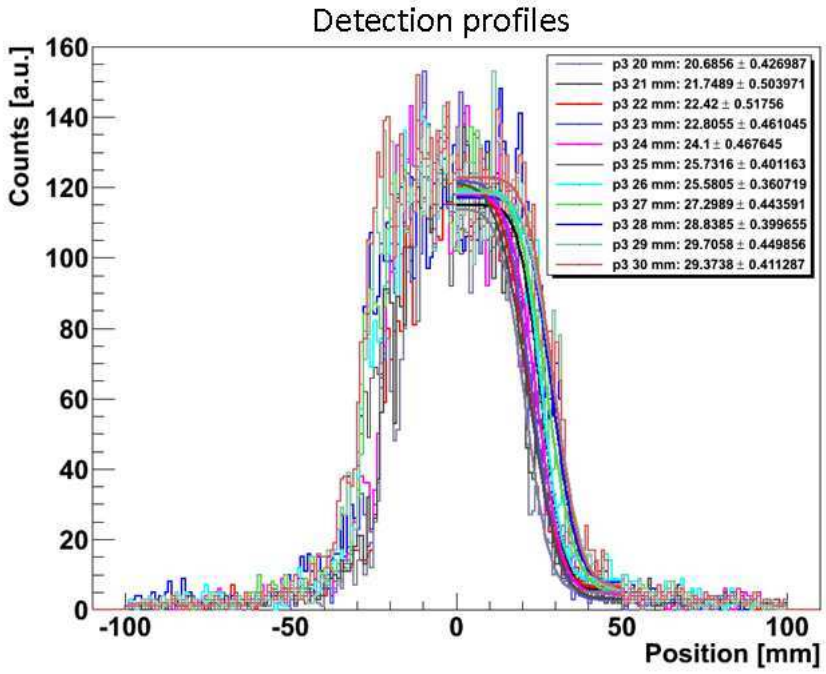

figure 6-15: Detection profiles for linear source length (Q) varying from 40 mm to 60 mm by steps of 2 mm. The fit curves on the right edge are performed with the function y=a+b·erf(c(x-d)). In the inset are respectively reported the position of the source edge (Q/2) and the value of the fit parameter d with its absolute error. For all the simulations S=T=3 mm, D=1 mm, H=5 cm, L=20 cm, B=35 cm. The reported photon counts have been detected with a configuration equivalent to a ring of 100 collimated detectors. The notation used to indicate the geometrical dimensions follows the one introduced in figure 6-2.

The fit inflection points reported on the ordinate axis of the graphs presented in figure 6-16 correspond to the value of the parameter *d* obtained from the error function fit performed on the photon detection profiles for each linear source length as shown, to give an example, in figure 6-15. As already mentioned, an ideal fit performed on a photon detection profile obtained with an ideal collimator with no source or detector penumbra and no transversal photon tile crossing, would provide the position of the fit inflection point exactly matching with the position of the source edge. Therefore in the graphs presented in figure 6-16 all the points would be perfectly aligned on the bisection line *(y=x)*. Nevertheless, although neither the collimator nor the error function fit could be considered ideal, the linear fits performed over the detection profiles for the configurations of the collimator placed in central position and toward the detectors (figure 6-16b and c), show that the slope of the fit is very close to ~1 and that the dispersion of the points around the bisection line is very low *($R^2 \approx 0.97$)*.

We can define an empiric criterion to characterize the spatial resolution *(R_{Cam})* as the minimum distance from two different source points, for which it could be clearly stated which is the one that has a longitudinal position lower than the second one. In other words R_{Cam} could be defined as the minimum distance between two successive source lengths for which the fit inflection position of the second point is always higher than the one of the first point for any given source length. Although we do not pretend that this definition could provide rigorous and absolute estimations of the spatial resolution it would at least supply a tool to compare our simulations results with each other and to offer a first estimation of the spatial resolution for the different configurations under investigation.

Following the definition introduced just above we can say that for both configurations presented in figure 6-16 b and c, the achievable spatial resolution *(R_{Cam})* is 2 mm. This means that, at least in principle, the minimal spatial resolution of the camera can be inferior to both the slit and tile dimensions since in the case of figure 6-16, $S=T=3\ mm$, and also inferior to a single detector width which was 3 mm *(D)*. This represents a positive result not only because thicker tiles and detector crystals are usually easier to be manufactured and assembled but also because, as reported in figure 6-13, the detection efficiency decreases linearly with the collimator tile width *(T)*.

Always on figure 6-16 it can be noted that the collimator position has anyhow a large influence on the achievable spatial resolution especially in the case where it is placed very close to the photon source. Indeed, in this case the collimator slit pattern completely hides the extension of the source edge when the edge translation occurs exactly in front of one of the collimator tiles. For this reason the achievable spatial resolution is greatly worsen and can be estimated, following the above mentioned empiric criteria, to $R_{Cam}=4\ mm$.

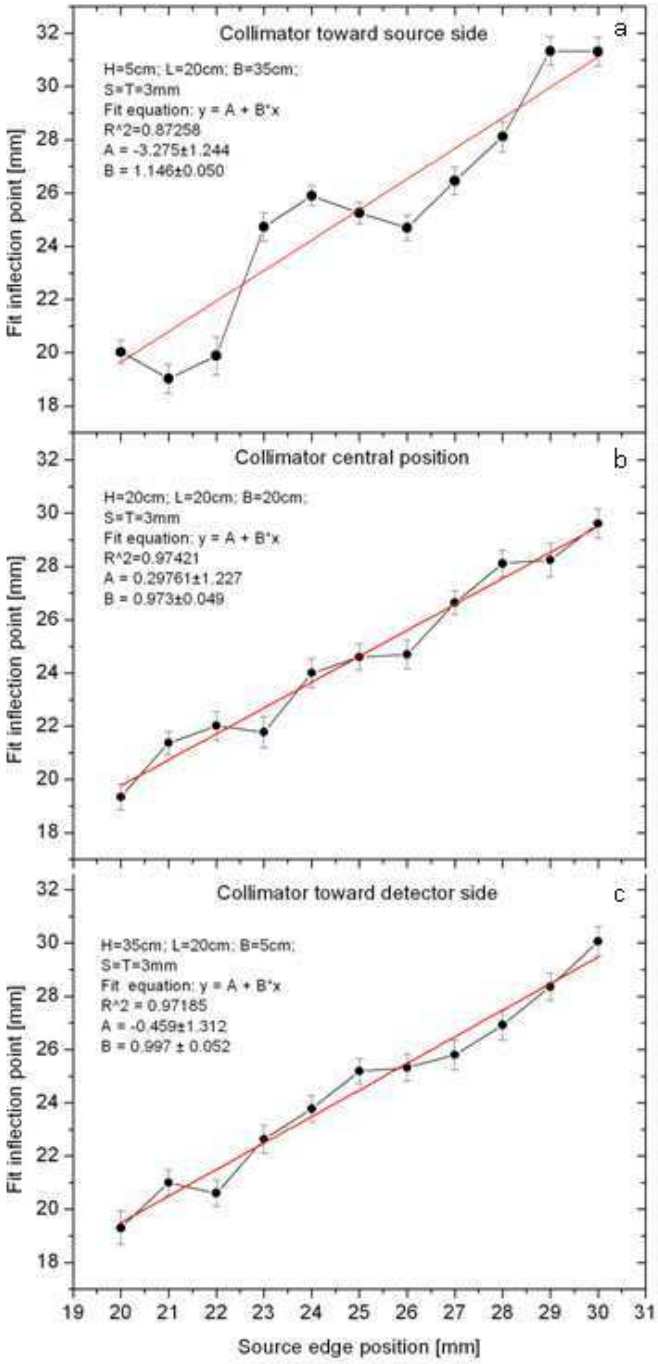

figure 6-16: Curves of fit inflection point vs. source edge position for three collimator positions: toward the source side (top), central position (middle) and toward the detector side (bottom). The fit inflection point corresponds to the parameter d of the error function fit presented, for example, in figure 6-15. The reported fit points have been performed on photon detection profiles which have been acquired with a configuration equivalent to a ring of 100 collimated detectors. In the inset is reported the equation of the linear fit (red line) weighted on the error bars of the simulation results. There are also reported all the geometrical parameters of each configuration according to the notation introduced in figure 6-2. For all the simulations D=3 mm, X=60 cm.

On the contrary, for the configuration in which the collimator is placed close to the detectors (figure 6-16c), although the collimator slit pattern is clearly visible on the photon detection profiles (as can be seen for example in figure 6-17) the

positions of the inflection points provided by the error function fit are all the same well correlated with the real source edge positions. Indeed, as already mentioned, the configuration presented in figure 6-16 b and c, with the collimator placed respectively in the central position and toward the detectors, have almost the same spatial resolution. But on the other hand, as shown in figure 6-10, the configuration with the collimator toward the detectors leads to an increase of the detection efficiency of about ~14% (for *L= 20 cm*) over the configuration where the collimator is placed centrally. Therefore, there could be some advantage in placing the collimator toward the detectors although this result must be validated by further investigations.

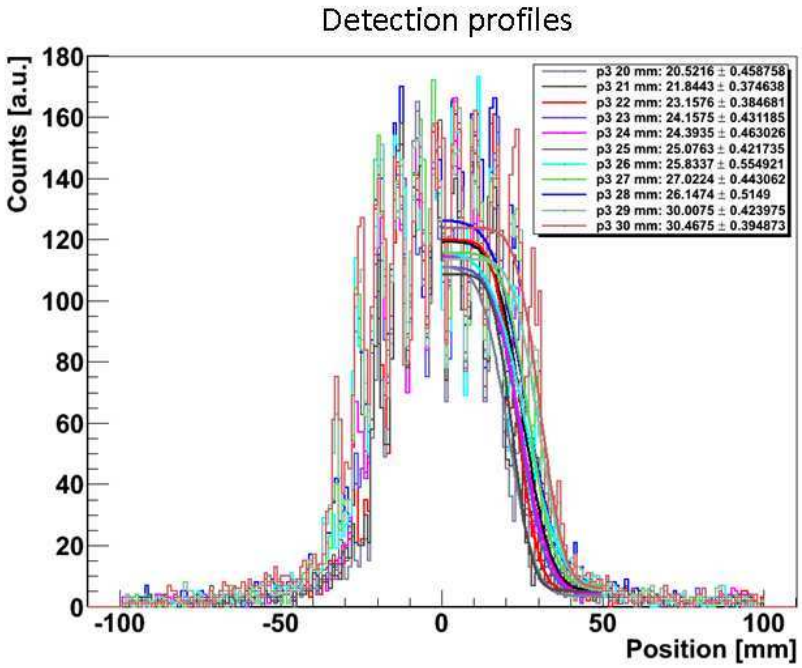

figure 6-17: Detection profiles for linear source length (Q) varying from 40 mm to 60 mm by steps of 2 mm. The fit curves on the right edge are performed with the function y=a+b·erf(c(x-d)). In the inset are respectively reported the position of the source edge (Q/2) and the value of the fit parameter d with its absolute error. For all the simulations S=T=3 mm, D=1 mm, H=35 cm, L=20 cm, B=5 cm. The reported photon counts have been detected with a configuration equivalent to a ring of 100 collimated detectors. The notation used to indicate the geometrical dimensions follows the one introduced in figure 6-2.

6.3.2.2 Influence of crystal detector width on the spatial resolution

As reported in equation 6-2, the total spatial resolution of the camera *(R_{Cam})* is a function of both the collimator *(R_{Coll})* and the detector resolution *(R_{Det})*. As already mentioned, as first approximation, R_{Det} can be assumed to be equal to the width of a single LYSO crystal *(D)*. In this series of simulations we performed a preliminary investigation on the influence of the detector width *(D)* on the total spatial resolution of the camera. Therefore, the same configuration presented in figure 6-16b *(S=T=D=3 mm; L=20 cm)* has been reproduced letting all the collimator parameters unchanged but reducing the single LYSO detector width *(D)* to 1 mm. The results of these simulations are reported in figure 6-18 where it can be noticed that a good linear correlation is

found between the fit inflection point and the source edge position but also that this correlation is not any better than the one presented in figure 6-16b for crystals three times larger. Indeed, although the detectors width has been reduced by a factor of 3, these two configurations seem essentially to lead to the same spatial resolution *(R=2 mm)* and the same dispersion of the points around the linear fit *($R^2 \approx 0.97$)*. Although these results have to be further verified by a larger systematic study we can reasonably assume that the collimator resolution plays a predominant role on the determination of the total resolution of the camera. For the global design of the camera this represents a positive result since it means that there is probably no need of choosing extremely thin detectors that would be, on the other side, very numerous to allow covering the entire C-ion range. Indeed the higher the number of detectors the higher the number of electronics signals which have to be recorded and processed leading to an increasingly complex device.

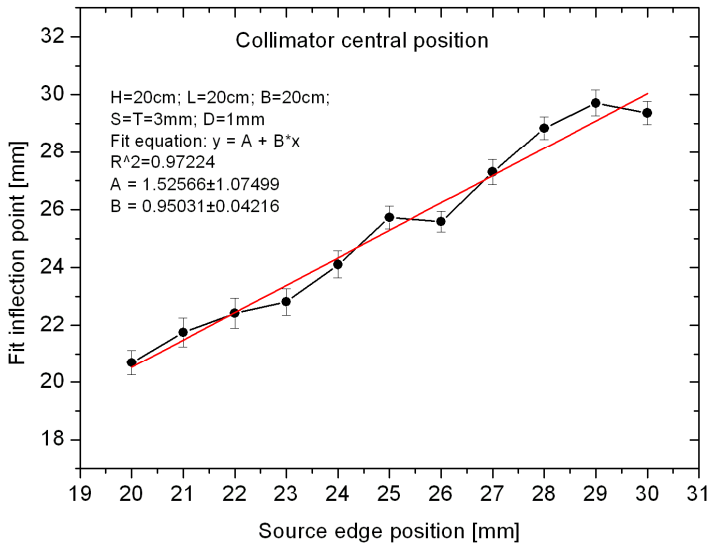

figure 6-18: Curve of fit inflection point vs. source edge position for the collimator placed in central position. The reported fit points have been performed on a photon detection profile which has been acquired with a configuration equivalent to a ring of 100 collimated detectors. In the inset is reported the equation of the linear fit (red line) weighted on the error bars of the simulation results. They are also reported all the geometrical parameter of each configuration according to the notation introduced in figure 6-2. For all the simulations X=60 cm.

6.3.2.3 Influence of the detection statistics on the spatial resolution

As already mentioned the number of emitted photons from the linear source and by consequence, the number of the detected counts, is a critical parameter which has a large influence on both the fit convergence and the absolute errors of the fit parameters. All the simulations performed to investigate the influence of the collimator design on the spatial resolution which have been presented so far have been obtained with a linear source activity of 5.05×10^5 γ/(mm) which is 100 times more intense than the linear density of prompt photons emitted per millimeter of C-ion path (5.05×10^3 γ/(mm)) for a typical dose of one iso-energy C-ion spill (26 mGyE).

As already mentioned increasing the linear source activity by a factor one hundred is equivalent to consider a ring of 100 collimated scintillators detecting the photons emitted from the original source activity. Nevertheless this represents only a hypothetic configuration, since in practice the maximum number of detectors, each 5 cm high *(Y)*, which can be physically placed on a ring with a radius of 60 cm *(X)* is about ~75. Moreover, for any future clinical application of the prompt gamma camera, it would not be reasonably imaginable to install a full ring of detectors around the patient. Therefore we performed a series of simulations to investigate the influence of the number of detectors, and by consequence the amount of detected statistics, on the achievable spatial resolution. These results are presented in figure 6-19 where the same configuration of the simulations presented in figure 6-16c (collimator placed toward the detector side and $S=T=D=3mm$) has been re-analyzed considering this time only the counting statistics acquired by 10, 20 and 50 detectors. As expected, both the slope of the linear fit and the dispersion of the points around the fit (R^2) worsen with the diminishing equivalent number of detectors on the ring. Nevertheless a still acceptable correlation of the fit inflection point and the real source edge position is observed even with only 10 equivalent detectors and moreover a spatial resolution R_{Cam} of about ~4-5 mm is still reachable. Anyhow it has to be mentioned that for such a reduced detected statistics the convergence of the error function fit on the photon detection profiles largely depends on the initialization values of free parameters of the fit function.

6.3.3 Conclusions and perspectives

A preliminary series of simulations has been performed in order to assess the influence of the main geometrical parameters of a multi-collimated and multi-detector gamma camera on its detection efficiency and special resolution. Although both these endpoints are intrinsically correlated we tried to decouple our analysis in order to investigate how the variations of each individual geometrical dimension of both collimators and stack of detectors would affect, respectively, the efficiency and spatial resolution of the camera.

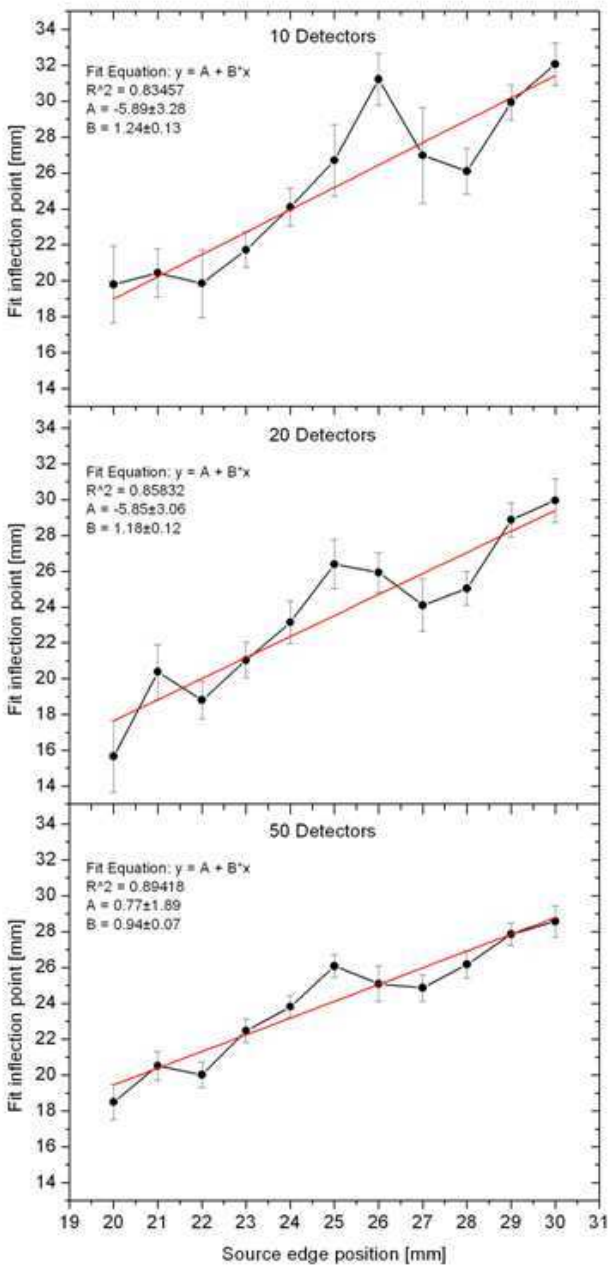

figure 6-19: Curves of fit inflection point vs. source edge position for three different linear activities of the photon source. The reported fit points have been performed on photon detection profiles which have been acquired with a configuration equivalent to 10 (top), 20 (middle) and 50 (bottom) collimated detectors. In the inset is reported the equation of the linear fit (red line) weighted on the error bars of the simulation results. They geometrical parameters of the simulated camera are the same as in figure 6-16

Several properties of the influence of collimator design on the detection efficiency which can be found in the literature have been verified by our Geant4 simulations. More specifically, it has been shown that the detection efficiency, as expected, decreases exponentially with the increase of the collimator thickness but it also depends, on a lower grade, on the collimator position with respect to the photon source. Indeed lower detection efficiencies, ranging from

about ~20% for a collimator thickness *L=15 cm* to ~5% for *L= 50 cm*, have been found for the configuration in which the collimator is centrally placed in between the source and the detectors. This behaviour could be qualitatively explained by considering the average detection efficiency *(<$>)* as the product of the geometrical detection solid angle *(Ω_D)* and the source field of view *(F_S)*. Nevertheless a more precise evaluation of both Ω_D and F_S, not only based on pure geometry, is necessary to allow for the quantitative reproduction of the simulated results. It has been also shown that in the case where the ratio between the slit aperture *(S)* and the tile width *(T)* is constant, the detection efficiency linearly depends on *S* (providing the collimator thickness is unchanged). Moreover the invariance of the efficiency when a scaling factor is applied to all the collimator dimensions *(S, T, L)*, which is a property usually reported in the literature (Gunter 2004), has been verified.

For a configuration equivalent to a ring of 100 collimated detectors, it has been found that, at least in principle, the minimal spatial resolution *(R_{Cam})* can be inferior to both the slit and tile dimensions *(S=T)*, and also inferior to a single detector width *(D)*. This represents a positive result not only because thicker tiles and detector crystals are usually easier to be manufactured and assembled but also because, as mentioned just above, the detection efficiency decreases linearly with the collimator tile width *(T)*. Moreover, we showed that although the total spatial resolution of the camera *(R_{Cam})* is a function of both the collimator *(R_{Coll})* and the detector resolution *(R_{Det})*, R_{Coll} plays a predominant role on the determination of R_{Cam}. For the global design of the camera this represents a positive result since it means that there is probably no need of choosing extremely thin detectors that would be, on the other side, very numerous to allow covering the entire C-ion range. Indeed the higher the number of detectors the higher the number of electronics signals which have to be recorded and processed leading to an increasingly complex device.

We showed as well that the collimator position has a large influence on the achievable spatial resolution especially in the case where it is placed very close to the photon source. Indeed, in this case, the collimator slit pattern completely hides the extension of the source edge when the edge translation occurs exactly in front of one of the collimator tiles leading hence to a large degradation of the spatial resolution. On the contrary, for the configuration in which the collimator is placed close to the detectors, although the collimator slit pattern is clearly visible on the photon detection profiles, the positions of the inflection points provided by the error function fit are all the same well correlated with the real source edge positions. As a consequence the configurations where the collimator is placed respectively in the central position (which in principle should bring to the best spatial resolution) and close to the detectors have almost the same spatial resolution. But on the other hand, as mentioned just above, the configuration with the collimator toward the detectors leads to an increase of the detection efficiency of about ~14% (for *L= 20 cm*) over the configuration where the collimator is placed centrally and therefore, there could be some advantage in placing the collimator toward the detectors.

At last we investigated the influence of the detection statistics on the achievable spatial resolution by making vary the equivalent number of collimated detectors placed on an ideal ring around the linear source of photons. As expected the spatial resolution worsen with the diminishing equivalent number of detectors placed on the ring. Nevertheless a still acceptable correlation of the fit inflection point and the real source edge position is observed even for the configurations with 10 and 20 equivalent detectors which would respectively cover only 0.83 rad and 1.67 rad of the 2π rad of the full azimuth. Since each detector has a height of 5 cm *(Y)*, such a configuration would correspond to a maximum circular extension of collimators and detectors of 1 m which could therefore reasonably be applied in a particle therapy treatment room. Moreover, one possible configuration to still increase the detection efficiency, and thus by consequence also the spatial resolution, would be to design a converging collimator (see figure 6-1) focusing on the Bragg-peak region. In this case the camera would not image the entire ion path but only the region of the distal part of ion range. Nevertheless, based on the actual result, with a converging collimator it would not be unreasonable to expect achieving for a focused region extending few centimeters around the Bragg-peak a spatial resolution of about ~2-3 mm at typical doses used in clinical therapy.

Another way to improve the detection efficiency would be to increase the detector thickness although some intrinsic limitation due to the internal radioactivity of LYSO crystals (which is not taken into account in the simulations presented so far) must be considered and therefore a trade-off has to be adopted between detection efficiency and background noise due to Lu decay. Nevertheless, although all the simulations have been performed with a crystal thickness *(E)* of 4 cm to allow for an easier comparison (still not presented in this work) of the experimental results obtained with the multi-detector experiment shown in the previous chapter, there is still some margin to increase the crystal thickness.

At last, these preliminary simulations will have to be pursued by new simulations in which the influence of all the geometrical parameters presented here would be investigated with a larger systematic study. Moreover the influence of the real mixed particle field emerging from a phantom irradiated with C-ions has to be taken into account since neutrons can be expected to blur the achievable spatial resolution. Furthermore, more realistic linear photon profiles have to be used instead of the actual linear source for which the photon emission abruptly drops to zero outside the source edges. Indeed during real C-ion irradiations several prompt photons are emitted from secondary particles even beyond the Bragg-peak and the contrast factor between the number of photons emitted before and beyond the Bragg-peak has large influence on the determination of the particle range.

7 Summary and outlook

In charged particle therapy in order to fully take advantage of the assets of the ion irradiation, the position of the Bragg-peak has to be monitored accurately. Indeed in contrast to conventional photon irradiation, ions exhibit a well defined range which determines the position of the maximum dose delivery in the tumor target. Therefore a monitoring technique allowing the determination of the ion range with a millimeter precision and possibly performed in *real time* with the irradiation would be highly desirable.

At present positron emission tomography (PET) is the only clinical method for *in vivo* and *in situ* monitoring in charged particle therapy (Enghardt et al. 1992). PET has been successfully employed in a pilot project at GSI facility (Darmstadt, Germany), to validate the whole chain from the planning to the application of the treatment and to detect unpredictable deviations in the maximum ion range (Parodi et al. 2008). Nevertheless, due to the very low induced positron activity and to the radioisotopes half-lives, which are much longer than the characteristic time (of the order of a second) in which an iso-energy slice of tumour is irradiated, any *real-time* range monitoring would be very unlikely to be done with PET.

Therefore in this thesis we presented a technique based on prompt photon detection which in principle would allow a *real-time* verification of the correctness of the application of treatment plan in the meanwhile of the irradiation itself. This would hence allow interrupting the irradiation in case an unpredicted mismatch between the planned and actual ion range or integral dose occurs.

In a first experiment performed at the GANIL facility (Caen, France) with 73 MeV/u $^{13}C^{6+}$ ions impinging on a PMMA target we demonstrated that the measurement of prompt γ-rays could be directly correlated with the ion range (E. Testa et al. 2008). Moreover, the discrimination between prompt photons (which are correlated with the C-ion range) and background radiation (uncorrelated with the C-ion range) made with time-of-flight (TOF) represents the main characteristic of our experimental set-up and it avoids the use of bulky neutron absorbers. This feature is of particular importance since it permits to significantly reduce the size of the shielding material (E. Testa et al. 2009) allowing a stacked multi-detector set-up that, in principle, can be employed clinically for *real-time in-situ* ion range monitoring. In a new series of experiment performed at the GANIL and GSI facilities with 95 MeV/u and 305 MeV/u $^{12}C^{6+}$ ion beams stopped in PMMA and water phantoms (M. Testa et al. 2010) we showed, as main results, that *i)* the correlation between prompt photon scan profile and C-ion range is maintained for those high energies typically used for ion therapy, *ii)* our technique may be applicable both to cyclotrons pulsed beam time structures if the pulse time-length is about 1 ns, and to synchrotrons continuous beam time structures if a detector is available that allows to trig the acquisition at particle intensities of about ~10^8 ion/s

typically used in C-ion therapy, *iii)* the detected prompt photon count rates provide sufficiently high statistics to encouragingly assume that real-time control of the longitudinal position of the Bragg-peak under clinical conditions is feasible, *iv)* by the combination of PSD and TOF technique for photon and neutron discrimination it can be stated that no evidence for a prompt neutron component correlated with the primary ion range exists and therefore fast neutrons detected at 90° cannot be considered to provide useful information on the dose profile. Moreover the preliminary results with the multi-detector experiment recently performed at GANIL with 75 MeV/u $^{13}C^{6+}$ ions showed that a clear correlation is observed between the ion path and the photon production yield for each of the stacked LYSO detectors, paving therefore the way for a future experiment with a larger multi-detector prototype to be performed with high energy C-ions.

In order to assess which will be the main constraints on the future prototype of multi-collimated and multi-detector gamma camera which is planned to be built by our group, we performed a preliminary series of Geant4 Monte Carlo simulations to assess the influence of the main geometrical parameters of camera on its detection efficiency and special resolution. Although we simulated a simplified camera set-up in which a linear source of photons replaced the prompt γ-rays produced by fragment de-excitation, we obtained the encouraging result that, with a detector ring containing about 10 or 20 scintillators of the same type of the ones used in the multi-detector experiment at GANIL, a spatial resolution of about ~2-3 mm at typical doses used in clinical therapy seems reasonably achievable. Nevertheless this simulation study has to be pursued taking into account the influence of real longitudinal prompt photon profiles arising from a phantom irradiated with C-ions along with the real mixed particle field emerging from the target since neutrons can be expected to blur the achievable spatial resolution.

As already mentioned the positive results presented in this thesis will lead to the development of a reduced scale prototype of multi-collimated and multi-detector camera which will be tested with high energy carbon ions and protons. Indeed the application of our prompt gamma camera to protontherapy is not only interesting because the number of protontherapy facilities in the world is much higher than the carbon therapy centres, but especially because we can expect a significant increase of the range monitoring performances with protons compared to carbon ions. In fact, although the number of prompt photons emitted per incident particle is 7.5 times lower with protons than with carbon (Le Foulher 2010), on average, to deliver the same tumour dose it is required a 40 times higher number of protons than carbons (G. Kraft 2000). Therefore a net increase in the prompt photon production of about a factor of ~5 is expected to be achieved with protons compared to C-ions for the same irradiation dose. Moreover the lack of proton projectile fragmentation and therefore the lack of secondary fragmentation beyond the Bragg-peak, will lead to sharper distal fall-off of the longitudinal prompt photon profiles which will still increase the resolution in the determination of the Bragg-peak position.

At last, in parallel to the experimental measurements presented in this thesis, an extensive simulation work has been performed by our group to study the emission of secondary prompt gamma-rays produced by nuclear reactions during carbon ion-beam therapy in order to validate the physics models handling the prompt de-excitation of nuclear fragments in Geant4 (Le Foulher et al. 2010). Moreover a series of simulation studies are currently ongoing with the aim of assessing the design guidelines for a Compton camera for prompt γ-imaging during ion beam therapy (M.-H. Richard et al. 2010). These simulation studies have been performed in the framework of a diversified research program for *real-time* control of the dose deposition in ion therapy which is currently being undertaken by our group and that includes a variety of systems like the collimated prompt-gamma camera, Compton camera and Interaction Vertex Imaging (Dauvergne et al. 2009) and which foresees to develop a clinical prototype of both a collimated and Compton prompt γ-camera.

8 Appendix

8.1 NaI(Tl) calibration for beam intensity monitoring

In all the experiments performed at GANIL facility the beam intensity was monitored by a NaI(Tl) scintillator (3 inches in diameter and length) placed at a large distance from the target, in order to obtain a counting rate proportional to the beam intensity but nearly independent of target position and collimation. This NaI(Tl) detector was calibrated with a Faraday cup (CF44) which is part of the standard beam monitor system of G4 experimental cave at GANIL and which could be remotely inserted and extracted from the beam line. As an example, in Table 8-1 are reported, for the case of the multi-detector experiment, the count rates for the NaI(Tl) scintillator and the reference beam current values provided by the Faraday cup (CF44). We remind that for C^{6+}-ions a beam current of 1nA corresponds to 1.04×10^9 ions/s.

Nal Monitor [Hz]	CF44 [nA]	Ions/s
20	0,0 ± 0,5	0,00E+00 ± 5,2E+08
330	0,3 ± 0,5	3,13E+08 ± 5,2E+08
910	1,0 ± 0,5	1,04E+09 ± 5,2E+08
650	0,8 ± 0,5	8,33E+08 ± 5,2E+08
1600	2,0 ± 0,5	2,08E+09 ± 5,2E+08
2400	3,0 ± 0,5	3,13E+09 ± 5,2E+08
2900	3,8 ± 0,5	3,96E+09 ± 5,2E+08
3600	4,2 ± 0,5	4,38E+09 ± 5,2E+08
1430	1,9 ± 0,5	1,98E+09 ± 5,2E+08
2200	2,7 ± 0,5	2,81E+09 ± 5,2E+08

Table 8-1: Detected count rates for the NaI(Tl) detector used to monitor the beam intensity. Reference beam current values are given by the Faraday cup (CF44) (for C^{6+} 1 nA ≈ 10^9 ions/s).

As can be noted in figure 8-1, the fit of data presented in Table 8-1 shows a good linearity between the beam intensity and the count rates detected by the NaI(Tl) scintillator up to beam currents of 5nA. During the experiments the beam current was set to about 1 nA, in order to optimize the detector counting rates while avoiding pile-up effects and minimizing the dead-time.

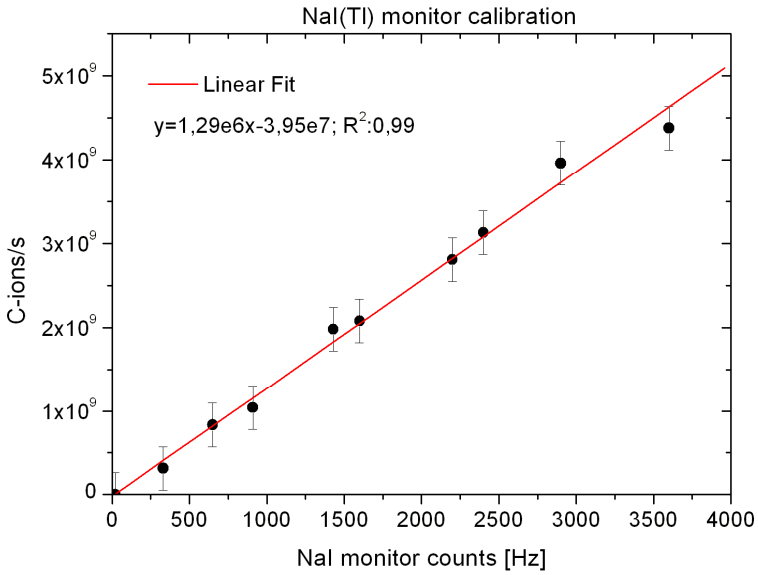

figure 8-1: Beam intensity as function of the count rates detected by NaI(Tl) monitor detector. A good linearity is observed up to beam intensities of ~5 nA. The error bars are due to the sensitivity of the Faraday cup (0.5 nA).

8.2 Electronics and acquisition set-up

For all experiments, the detectors readout (time and energy distributions) was performed with conventional NIM electronics and a VME data acquisition system. In the following are presented the block diagrams of the signal processing schematics.

8.2.1 GANIL single-detector experiment

In GANIL single-detector experiment, three scintillators (BaF_2, BC501 and NaI(Tl)) triggered the data acquisition performed through both a peak sensing analog to digital converter (ADC) and a charge integrating analog to digital converter (QDC). The block diagram of the signals processing schematic is presented in figure 8-2. As described in the previous paragraph, the NaI(Tl) scintillator was used to monitor the beam intensity detecting background events with a counting rate proportional to the beam current. The choice of using the NaI(Tl) scintillator as one of the triggering detectors was done to record not only the rate (through a VME scaler module) but also the energy spectrum of the background events. This provided a redundant but almost independent information which can potentially avoid normalisation problems if the threshold of the NaI discriminator (Discri) slightly varies during the experiment. Nevertheless, to minimize acquisition dead-time, we employed a divisor module (Divisor) which allowed seizing only one tenth of the triggered signals. To be rigorous, the count rate values reported as an example in Table 8-1 are undivided values, which means that in reality, for a beam current of 1 nA only 91 events/s were recorded by the acquisition chain.

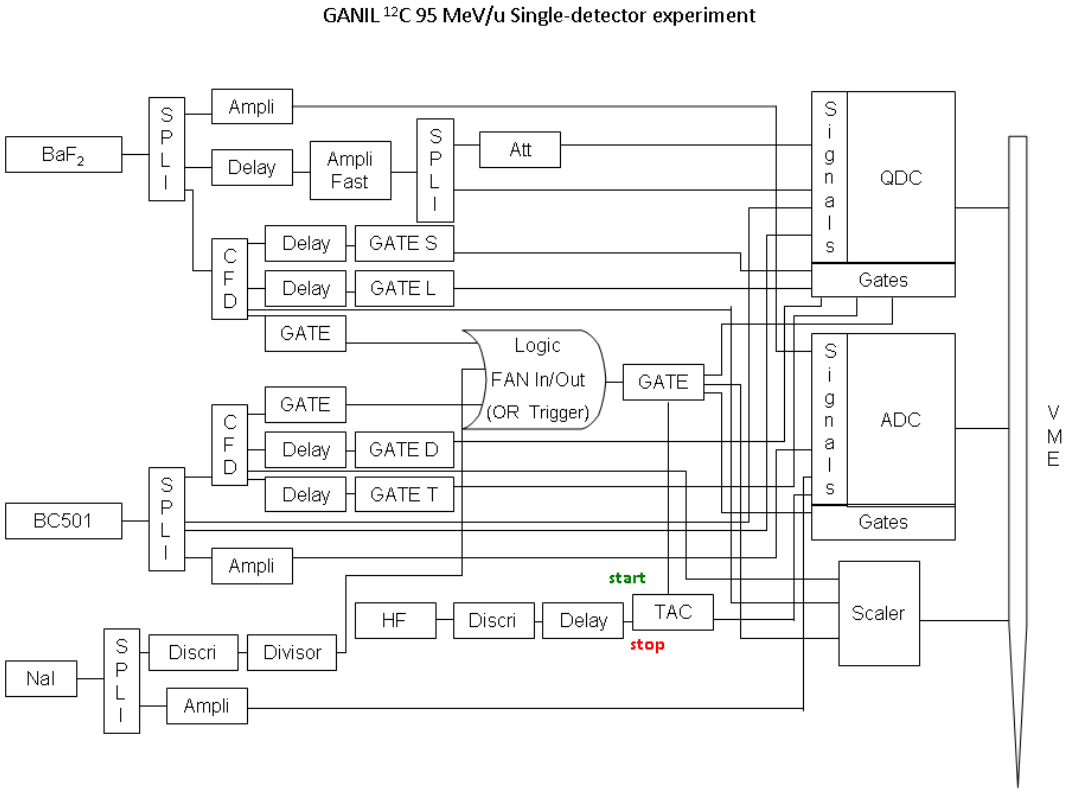

figure 8-2: Block diagram of the signals processing schematic for GANIL single -detector experiment.

The TOF measurements have been performed by means of a time to amplitude converter (TAC) whose start signal was provided either by BC501 or BaF_2 detectors both triggered by a constant fraction discriminator (CFD). The time walk was set to optimize the triggering on the signals having pulse heights of interest for the present study (photons between 1-10 MeV). The TOF stop signal was provided by the cyclotron high frequency (HF) signal (beam pulse of ~1 ns every 80 ns) suitably delayed.

Both BaF_2 and BC501 anode signals were split (SPLI) and processed to allow for amplitude and charge coding. In both cases the radiation energy measurement has been simply performed by linear amplification (Ampli) of the detectors signals successively fed in the ADC. The signal processing for charge coding was more complicated. Since for PSD the same anode signal has to be integrated over two different gates, in the case of BC501, a delayed and total gate (GATE D, T) of 300 ns and shifted by 35 ns (see figure 5-5) have been created to integrate the untreated anode signal. On the other hand, in the case of BaF_2 we generated a short (50 ns) and long (500 ns) gate (GATE S, L) and the anode signal was firstly amplified with a fast amplifier (Ampli Fast) which did not affect the pulse shape and then re-split. The signal integrated over the long gate was then attenuated (Att) while no further process was performed to the signal integrated over the short gate. This particular signal processing was adopted to achieve better PSD performances.

8.2.2 GSI single-detector experiment

The block diagram of the signals processing schematic for GSI single-detector experiment presented in figure 8-3 is almost identical to that used at GANIL and presented above except for the TOF stop signal which in this case was provided by two plastic scintillators (PL 1,2) intercepting the beam. These scintillators were also used to measure the integrated number of ions hitting the target and therefore their count rate was directly coded by a VME scaler module. The plastic scintillators efficiency was checked by comparing single and coincidence detection modes and found to be ~100% up to a few 10^5 ions/s.

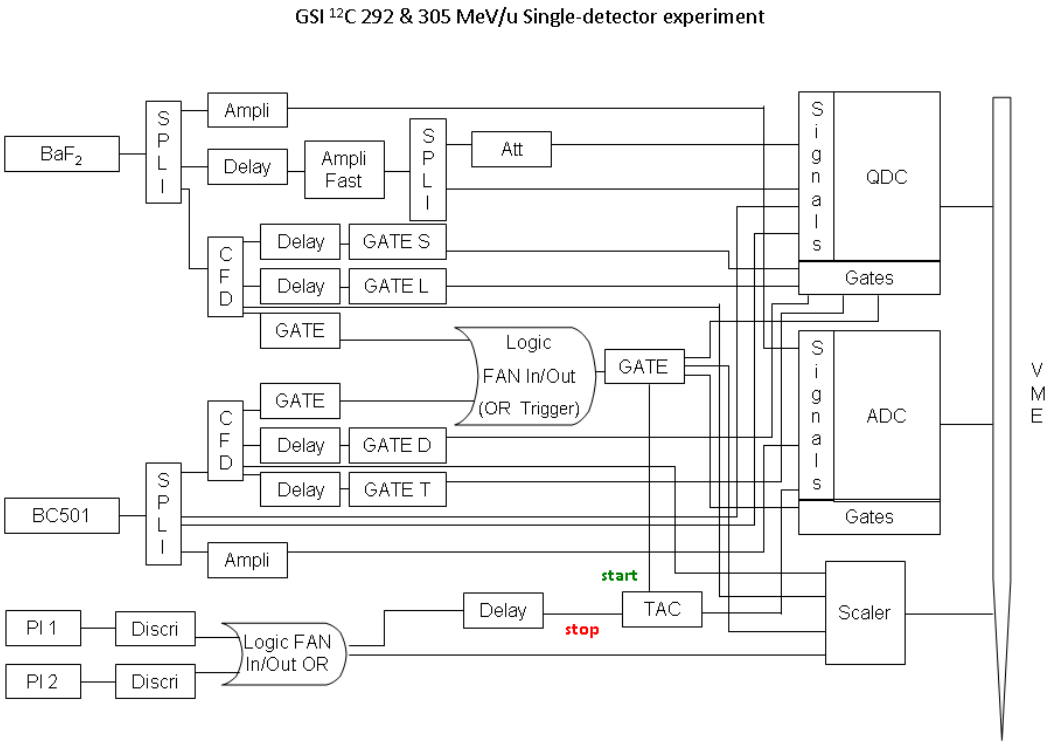

figure 8-3: Block diagram of the signals processing schematic for GSI single-detector experiment.

8.2.3 GANIL multi-detector experiment

In GANIL multi-detector experiment, five LYSO scintillators (LYSO 1-5) and one NaI(Tl) detector (NaI dose) triggered the data acquisition performed through a peak sensing analog to digital converter (ADC). The block diagram of the signals processing schematic is presented in figure 8-4. As for the single-detector experiment the NaI(Tl) was used to monitor the beam intensity and its signal processing was identical to that presented in section 0.

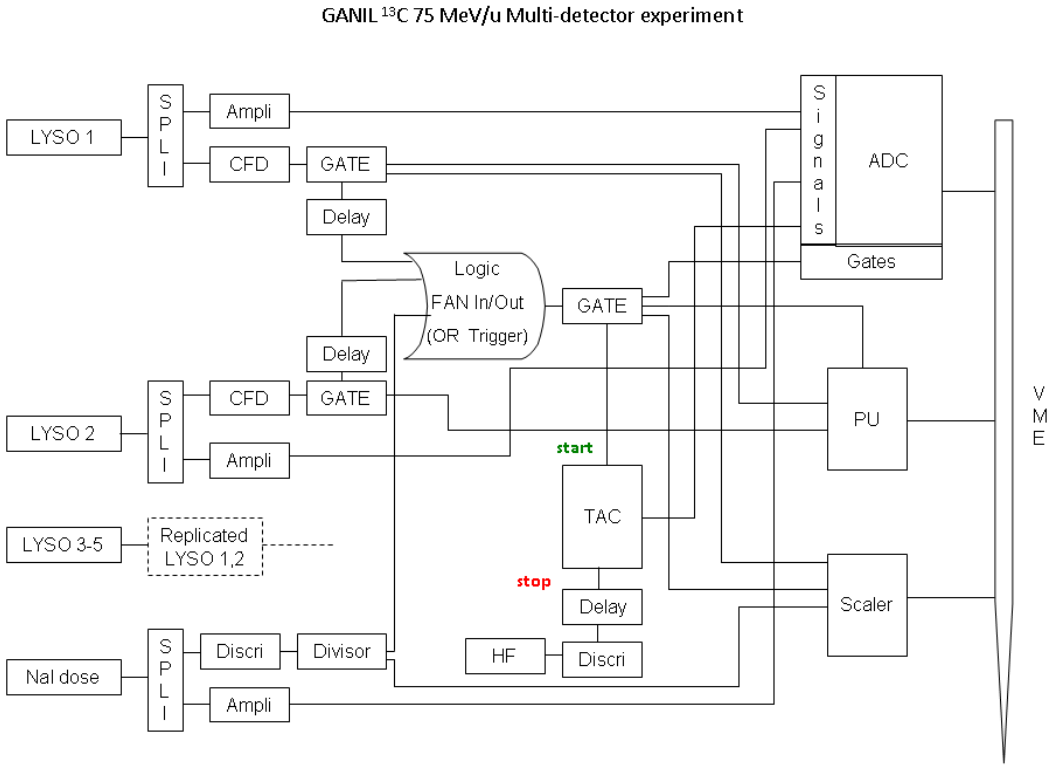

figure 8-4: Block diagram of the signals processing schematic for GANIL multi-detector experiment.

Again, the TOF measurements have been performed by means of a time to amplitude converter (TAC) whose start signal was provided by any one of the five LYSO detectors all triggered by a constant fraction discriminator (CFD). The TOF stop signal was provided by the cyclotron high frequency (HF) signal (beam pulse of ~1 ns every 80 ns) suitably delayed. In the on-line and off-line data analysis a pattern unit VME module (PU) was used to identify which LYSO scintillator triggered the acquisition event.

Bibliography

Achenbach, P. et al., 2008. In-beam tests of scintillating fibre detectors at MAMI and at GSI. *Nuclear Instruments and Methods in Physics Research Section A: Accelerators, Spectrometers, Detectors and Associated Equipment*, 593(3), 353–360.

Adler Jr, J.R. et al., 1997. The Cyberknife: a frameless robotic system for radiosurgery. *Stereotactic and functional neurosurgery*, 69(1-4 Pt 2), 124.

Agostinelli, S. et al., 2003. Geant4-a simulation toolkit. *Nuclear Instruments and Methods in Physics Research-Section A*, 506(3), 250–303.

Amaldi, U. & Kraft, G., 2007. European developments in radiotherapy with beams of large radiobiological effectiveness. *Journal of Radiation Research*, 48(Suppl. A), 27–41.

Ammerlaan, C.A.J., Rumphorst, R.F. & Koerts, L.A., 1963. Particle identification by pulse shape discrimination in the pin type semiconductor detector. *Nuclear Instruments and Methods*, 22, 189–200.

Anger, H.O., 1964. Scintillation camera with multichannel collimators. *Journal of Nuclear Medicine*, 5(7), 515.

Barkas, W.H. & Evans, D.A., 1963. *Nuclear research emulsions*, Academic Press New York.

Barnabà, O. et al., 1998. A Full–Integrated Pulse Shape Discriminator for Liquid Scintillator Counters. *Nuclear Instruments and Methods in Physics Research Section A: Accelerators, Spectrometers, Detectors and Associated Equipment*, 410(2), 220–228.

Baro, J. et al., 1995. PENELOPE: an algorithm for Monte Carlo simulation of the penetration and energy loss of electrons and positrons in matter. *Nuclear Instruments and Methods in Physics Research Section B: Beam Interactions with Materials and Atoms*, 100(1), 31–46.

Barth, R.F., Soloway, A.H. & Fairchild, R.G., 1990. Boron Neutron Capture Therapy of Cancer1. *Cancer Research*, 50, 1061–1070.

Battistoni, G. et al., 2007. The FLUKA code: Description and benchmarking. Dans *AIP Conference Proceedings*. p. 31.

Beddoe, A.H., 1997. Boron neutron capture therapy. *British Journal of Radiology*, 70, 665–667.

Berger, M.J. et al., 1998. XCOM: photon cross sections database. *NIST Standard*

Reference Database, 8, 87–3597.

Bergonzo, P. et al., 2001. CVD diamond for radiation detection devices. *Diamond and Related Materials*, 10(3-7), 631–638.

Bert, C., Grozinger, S.O. & Rietzel, E., 2008. Quantification of interplay effects of scanned particle beams and moving targets. *Physics in medicine and biology*, 53(9), 2253–2266.

Bethe, H., 1930. Zur theorie des durchgangs schneller korpuskularstrahlen durch materie. *Annalen der Physik*, 397(3), 325–400.

Beuve, M. et al., 2009. Statistical effects of dose deposition in track-structure modelling of radiobiology efficiency. *Nuclear Instruments and Methods in Physics Research Section B: Beam Interactions with Materials and Atoms*, 267(6), 983–988.

Bielajew, A. et al., 1994. History, Overview and Recent Improvement of EGS4. *Technical report PIRS-0436*.

Birks, J.B., 1951. Scintillations from organic crystals: specific fluorescence and relative response to different radiations. *Proceedings of the Physical Society. Section A*, 64, 874–877.

Blakely, E.A. et al., 1979. Inactivation of human kidney cells by high-energy monoenergetic heavy-ion beams. *Radiat. Res*, 80(1), 122–160.

Bloch, F., 1933. Bremsvermögen von Atomen mit mehreren Elektronen. *Zeitschrift für Physik A Hadrons and Nuclei*, 81(5), 363–376.

Bloser, P. et al., 2003. Development of silicon strip detectors for a medium energy gamma-ray telescope. *Nuclear Instruments and Methods in Physics Research Section A: Accelerators, Spectrometers, Detectors and Associated Equipment*, 512(1-2), 220–228.

Bortfeld, T., 2009. The number of beams in IMRT-theoretical investigations and implications for single-arc IMRT. *Arxiv preprint arXiv:0909.3332*.

Bortfeld, T. & Webb, S., 2009. Single-arc IMRT? *Physics in Medicine and Biology*, 54, N9–N20.

Bragg, W.H. & Kleeman, R., 1905. On the alpha particles of radium and their loss of range in passing through various atoms and molecules. *Philos. Mag*, 10, 318.

Brahme, A. et al., 2001. Design of a centre for biologically optimised light ion therapy in Stockholm. *Nuclear Inst. and Methods in Physics Research, B*, 184(4), 569–588.

Braunn, B. et al., 2010. 12C nuclear reaction measurements for hadrontherapy. *12th international conference on nuclear reaction mechanisms*.

Brower, V., 2009. European boost for particle therapy. *Nature*, 457(7226), 139.

Bushberg, J.T. et al., 2003. The essential physics of medical imaging. *Medical Physics*, 30, 1936.

Carminati, F. & al., 1991. GEANT Users Guide. *CERN program Library*.

Chatterjee, A. et al., 1981. High energy beams of radioactive nuclei and their biomedical applications. *Int. J. Radiat. Oncol. Biol. Phys*, 7, 503–7.

Chu, W.T., Ludewigt, B.A. & Renner, T.R., 1993. Instrumentation for treatment of cancer using proton and light-ion beams. *Review of Scientific Instruments*, 64, 2055.

Cirrone, G.A.P. et al., 2010. Validation of the Geant4 electromagnetic photon cross-sections for elements and compounds. *Nuclear Instruments and Methods in Physics Research Section A: Accelerators, Spectrometers, Detectors and Associated Equipment*.

Constanzo, J., 2010. Etude et mise au point d'un détecteur pour le monitorage en ligne de l'hadronthérapie à l'aide des gamma prompts. *M.S. Thesis, Institut de physique nucléaire de Lyon Université Claude Bernard Lyon1*.

Crespo, P., Shakirin, G. & Enghardt, W., 2006. On the detector arrangement for in-beam PET for hadron therapy monitoring. *Physics in Medicine and Biology*, 51, 2143–2163.

Crespo, P. et al., 2007. Direct time-of-flight for quantitative, real-time in-beam PET: a concept and feasibility study. *Physics in Medicine and Biology*, 52(23), 6795–6811.

Crespo, P., 2006. Optimization of in-beam positron emission tomography for monitoring heavy ion tumor therapy. *PhD Thesis, Technische Universität Darmstadt Germany*.

Crittin, M., Kern, J. & Schenker, J.L., 2000. The new prompt gamma-ray activation facility at the Paul Scherrer Institute, Switzerland. *Nuclear Instruments and Methods in Physics Research Section A: Accelerators, Spectrometers, Detectors and Associated Equipment*, 449(1-2), 221–236.

Dale, R.G., 1986. The application of the linear-quadratic model to fractionated radiotherapy when there is incomplete normal tissue recovery between fractions, and possible implications for treatments involving multiple fractions per day. *British Journal of Radiology*, 59(705), 919.

Dauvergne, D. et al., 2009. New methods of real-time control imaging for ion therapy. *NIRS-ETOILE Joint Symposium on Carbon Ion Therapy, Lyon France*. Available at: hal.in2p3.fr/docs/00/36/33/82/PDF/NIRS-ETOILE_Dauvergne.pdf.

Davisson, C.M. & Evans, R.D., 1952. Gamma-ray absorption coefficients. *Reviews of Modern Physics*, 24(2), 79–107.

d'Enterria, D.G. et al., 2001. Evidence for thermal equilibration in multifragmentation reactions probed with bremsstrahlung photons. *Physical Review Letters*, 87(2), 22701.

Dilmanian, F.A. et al., 1998. Improvement of the prompt-gamma neutron activation facility at Brookhaven National Laboratory. *Physics in Medicine and Biology*, 43, 339–349.

Durante, M. & Loeffler, J.S., 2009. Charged particles in radiation oncology. *Nature Reviews Clinical Oncology*.

Elsässer, T., Krämer, M. & Scholz, M., 2008. Accuracy of the local effect model for the prediction of biologic effects of carbon ion beams in vitro and in vivo. *International Journal of Radiation Oncology, Biology, Physics*.

Elsässer, T. & Scholz, M., 2007. Cluster effects within the local effect model. *Radiation research*, 167(3), 319–329.

Enghardt, W. et al., 2004. Charged hadron tumour therapy monitoring by means of PET. *Nuclear Inst. and Methods in Physics Research, A*, 525(1-2), 284–288.

Enghardt, W. et al., 1992. The spatial distribution of positron-emitting nuclei generated by relativistic light ion beams in organic matter. *Physics in Medicine and Biology*, 37, 2127–2131.

Enghardt, W. et al., 2004. Dose quantification from in-beam positron emission tomography. *Radiotherapy and Oncology*, 73, 96–98.

Enghardt, W. et al., 2000. Positron emission tomography (PET) for ion therapy quality assurance. *GSI Scientific Report*, 2001–1.

Fano, U., 1963. Penetration of protons, alpha particles, and mesons. *Annual Review of Nuclear Science*, 13(1), 1–66.

Fiedler, F. et al., 2010. On the effectiveness of ion range determination from in-beam PET data. *Physics in medicine and biology*, 55(7), 1989.

Firestone, R.B. et al., 1996. *Table of isotopes*, Wiley New York.

Fuchs, R. et al., 2008. Assembly of the carbon beam gantry at the Heidelberg Ion Therapy (HIT) accelerator.

Furusawa, Y. et al., 2000. Inactivation of Aerobic and Hypoxic Cells from Three Different Cell Lines by Accelerated 3He,12C and 20Ne Ion Beams. *Radiation research*, 154(5), 485–496.

Geiger, K.W. & Van der Zwan, L., 1975. Radioactive neutron source spectra from 9Be (alpha, n) cross section data. *Nuclear Instruments and Methods*, 131(2), 315–321.

Gottschalk, B., 2006. Neutron dose in scattered and scanned proton beams: In regard to Eric J. Hall (Int J Radiat Oncol Biol Phys 2006; 65: 1-7). *International Journal of Radiation Oncology* Biology* Physics*, 66(5), 1594.

Gudowska, I. et al., 2004. Ion beam transport in tissue-like media using the Monte Carlo code SHIELD-HIT. *Physics in medicine and biology*, 49, 1933.

Gunter, D.L., 2004. Collimator design for nuclear medicine. *Emission tomography: the fundamentals of PET and SPECT. San Diego, London: Elsevier Academic*, 153–68.

Gunzert-Marx, K., 2004. Nachweis leichter Fragmente aus Schwerionenreaktionen mit einem BaF2-Teleskop-Detektor. *PhD Thesis, Technische Universität Darmstadt Germany*.

Gunzert-Marx, K. et al., 2008. Secondary beam fragments produced by ions 200 MeV/u 12C in water and their dose contributions in carbon ion radiotherapy. *New Journal of Physics*, 10, 075003.

Gunzert-Marx, K. et al., 2005. Response of a BaF2 scintillation detector to quasi-monoenergetic fast neutrons in the range of 45 to 198MeV. *Nuclear Inst. and Methods in Physics Research, A*, 536(1-2), 146–153.

Haberer, T. et al., 1993. Magnetic scanning system for heavy ion therapy. *Nuclear Instruments and Methods in Physics Research Section A: Accelerators, Spectrometers, Detectors and Associated Equipment*, 330(1-2), 296–305.

Haberer, T. et al., 2004. The Heidelberg ion therapy center. *Radiotherapy and Oncology*, 73, 186–190.

Haettner, E., 2006. Experimental study on carbon ion fragmentation in water using GSI theraphy beams. *M.S. Thesis Kungliga tekniska hogskolan Stockholm*.

Haettner, E., Iwase, H. & Schardt, D., 2006. Experimental fragmentation studies with 12C therapy beams. *Radiation protection dosimetry*, 122(1-4), 485.

Harrison, R.L. et al., 2002. Acceleration of SimSET photon history generation. Dans *2002 IEEE Nuclear Science Symposium Conference Record*.

Henriquet, P., 2010. Etude de l'emission de particules chragées secondaires dans l'optique d'une dosimetrie en ligne en hadrontherapie. *PhD Thesis, Institut de physique nucléaire de Lyon Université Claude Bernard Lyon1*.

Highland, V.L., 1975. Some practical remarks on multiple scattering. *Nuclear Instruments and Methods*, 129(2), 497–499.

Hüfner, J., 1985. Heavy fragments produced in proton-nucleus and nucleus-nucleus collisions at relativistic energies. *Physics Reports*, 125(4), 129–185.

Iseki, Y. et al., 2004. Range verification system using positron emitting beams for heavy-ion radiotherapy. *Physics in Medicine and Biology*, 49(14), 3179–3195.

Iwase, H. et al., 2005. Comparison between calculation and measured data on secondary neutron energy spectra by heavy ion reactions from different thick targets. *Radiation protection dosimetry*, 116(1-4), 640.

Jackson, J.D., 1975. *Classical Electrodynamics* 2nd ed., John Wiley & Sons New York.

Jäkel, O. et al., 2007. On the cost-effectiveness of Carbon ion radiation therapy for skull base chordoma. *Radiotherapy and Oncology*, 83(2), 133–138.

Jan, S. et al., 2004. GATE: a simulation toolkit for PET and SPECT. *Physics in Medicine and Biology*, 49, 4543.

Johns, H.E. & Cunningham, J.R., 1983. *The physics of radiology* 4th ed., Thomas Springfield, Illinois.

Jones, L.T. & Woollam, P.B., 1975. Resolution improvement in CdTe gamma detectors using pulse-shape discrimination. *Nuclear Instruments and Methods*, 124(2), 591–595.

K. Weyrather, S.R., 1999. RBE for carbon track-segment irradiation in cell lines of differing repair capacity. *International Journal of Radiation Biology*, 75(11), 1357–1364.

Kanai, T. et al., 1999. Biophysical characteristics of HIMAC clinical irradiation system for heavy-ion radiation therapy. *International Journal of Radiation Oncology Biology Physics*, 44(1), 201–210.

Kato, I. et al., 2004. Effectiveness of BNCT for recurrent head and neck malignancies. *Applied Radiation and Isotopes*, 61(5), 1069–1073.

Kitagawa, A. et al., 2006. Medical application of radioactive nuclear beams at HIMAC. *Review of Scientific Instruments*, 77, 03C105.

Kligerman, M.M. et al., 1979. Experience with pion radiotherapy. *CA A Cancer Journal for Clinicians*, 43(3), 1043–1051.

Knoll, G.F., 1989. *Radiation detection and measurement*, Wiley New York.

Kobayashi, T., Sakurai, Y. & Ishikawa, M., 2000. A noninvasive dose estimation system for clinical BNCT based on PG-SPECT—Conceptual study and fundamental experiments using HPGe and CdTe semiconductor detectors. *Medical Physics*, 27, 2124.

Kooy, H.M. et al., 2010. A Case Study in Proton Pencil-Beam Scanning Delivery.

International Journal of Radiation Oncology Biology Physics, 76(2), 624–630.

Kox, S. et al., 1987. Trends of total reaction cross sections for heavy ion collisions in the intermediate energy range. *Physical Review C*, 35(5), 1678–1691.

Kraft, G., 2000. Tumor therapy with heavy charged particles. *Progress in Particle and Nuclear Physics*, 45, 473–544.

Kraft, G. & Kraft, S.D., 2009. Research needed for improving heavy-ion therapy. *New Journal of Physics*, 11, 025001.

Krämer, K.W. et al., 2006. Development and characterization of highly efficient new cerium doped rare earth halide scintillator materials. *Journal of Materials Chemistry*, 16(27), 2773–2780.

Krämer, M. et al., 2000. Treatment planning for heavy-ion radiotherapy: physical beam model and dose optimization. *Physics in Medicine and Biology*, 45(11), 3299–3318.

Krämer, M. & Scholz, M., 2000. Treatment planning for heavy-ion radiotherapy: calculation and optimization of biologically effective dose. *Physics in medicine and biology*, 45(11), 3319–3330.

Le Foulher, F., 2010. Simulations Monte Carlo et mesures de l'emission de gamma prompts appliquées au contrôle en ligne en hadronthérapie. *PhD Thesis, Institut de physique nucléaire de Lyon Université Claude Bernard Lyon1*.

Le Foulher, F. et al., 2010. Monte Carlo simulations of prompt-gamma emission during carbon ion irradiation. *Accepted for publication in IEEE TNS*.

Lechner, A., Ivanchenko, V.N. & Knobloch, J., 2010. Validation of recent Geant4 physics models for application in carbon ion therapy. *Nuclear Instruments and Methods in Physics Research Section B: Beam Interactions with Materials and Atoms*. 268, 2343-2354

Lempicki, A., Wojtowicz, A.J. & Berman, E., 1993. Fundamental limits of scintillator performance. *Nuclear Instruments and Methods in Physics Research Section A: Accelerators, Spectrometers, Detectors and Associated Equipment*, 333(2-3), 304–311.

Leo, W.R., 1994. *Techniques for nuclear and particle physics experiments: a how-to approach*, Springer Verlag.

Li, Q. et al., 2007. Heavy-ion conformal irradiation in the shallow-seated tumor therapy terminal at HIRFL. *Medical and Biological Engineering and Computing*, 45(11), 1037–1043.

Llacer, J., Schmidt, J.B. & Tobias, C.A., 1990. Characterization of fragmented heavy-ion beams using a three-stage telescope detector: Measurements of 670-MeV/amu Ne beams. *Medical physics*, 17, 151.

Lomax, A.J. et al., 2004. Treatment planning and verification of proton therapy using spot scanning: initial experiences. *Medical physics*, 31, 3150.

Lorch, E.A., 1973. Neutron spectra of 241Am-B, 241Am-Be, 241Am-F, 242Cm-Be, 238Pu-13C and 252Cf isotopic neutron sources. *The International journal of applied radiation and isotopes*, 24(10), 585.

Mackie, T.R. et al., 1999. Tomotherapy. Dans *Seminars in Radiation Oncology*. p. 108–117.

Marrone, S. et al., 2006. Pulse shape analysis of signals from BaF2 and CeF3 scintillators for neutron capture experiments. *Nuclear Instruments and Methods in Physics Research Section A: Accelerators, Spectrometers, Detectors and Associated Equipment*, 568(2), 904–911.

Maughan, R.L. & Burmeister, J., 2007. Intensity modulated neutron therapy for the treatment of adenocarcinoma of the prostate. *Int. J. Radiation Oncology Biol. Phys*, 68(5), 1546–1556.

Meier, D. et al., 2002. Silicon detector for a Compton camera in nuclear medical imaging. *IEEE Transactions on Nuclear Science*, 49(3), 812–816.

Min, C.H. et al., 2006. Prompt gamma measurements for locating the dose falloff region in the proton therapy. *Applied physics letters*, 89, 183517.

Mollenauer, J.F., 1962. Gamma-Ray Emission from Compound Nucleus Reactions of Helium and Carbon Ions. *Physical Review*, 127(3), 867–879.

Mowlavi, A.A. & Koohi-Fayegh, R., 2004. Determination of 4.438 MeV gamma-ray to neutron emission ratio from a 241Am-9Be neutron source. *Applied Radiation and Isotopes*, 60(6), 959–962.

Newhauser, W.D. et al., 2009. The risk of developing a second cancer after receiving craniospinal proton irradiation. *Physics in Medicine and Biology*, 54, 2277–2291.

Nifenecker, H. et al., 1972. Gamma-neutron competition in the de-excitation mechanism of the fission fragments of 252Cf. *Nuclear Physics A*, 189(2), 285–304.

Niita, K. et al., 2006. PHITS–a particle and heavy ion transport code system. *Radiation measurements*, 41(9-10), 1080–1090.

Normand, S. et al., 2002. Discrimination methods between neutron and gamma rays for boron loaded plastic scintillators. *Nuclear Instruments and Methods in Physics Research Section A: Accelerators, Spectrometers, Detectors and Associated Equipment*, 484(1-3), 342–350.

Oliveira, L.F., Donangelo, R. & Rasmussen, J.O., 1979. Abrasion-ablation calculations

of large fragment yields from relativistic heavy ion reactions. *Physical Review C*, 19(3), 826–833.

Paganetti, H., Bortfeld, T. & Delaney, T.F., 2006. Neutron dose in proton radiation therapy: in regard to Eric J. Hall (Int J Radiat Oncol Biol Phys 2006; 65: 1-7). *International Journal of Radiation Oncology* Biology* Physics*, 66(5), 1594–1595.

Paganetti, H. et al., 2002. Relative biological effectiveness (RBE) values for proton beam therapy 1. *International Journal of Radiation Oncology Biology Physics*, 53(2), 407–421.

Park, S.T., 2003. Neutron energy spectra of 252 Cf, Am-Be source and of the D (d, n) 3 He reaction. *Journal of Radioanalytical and Nuclear Chemistry*, 256(1), 163–166.

Parodi, K., 2004. On the feasibility of dose quantification with in-beam PET data in radiotherapy with 12C and proton beams. *PhD Thesis, Technische Universität Dresden Germany*.

Parodi, K. et al., 2008. PET imaging for treatment verification of ion therapy: Implementation and experience at GSI Darmstadt and MGH Boston. *Nuclear Inst. and Methods in Physics Research, A*, 591(1), 282–286.

Parodi, K. et al., 2005. Random coincidences during in-beam PET measurements at microbunched therapeutic ion beams. *Nuclear Instruments and Methods in Physics Research Section A: Accelerators, Spectrometers, Detectors and Associated Equipment*, 545(1-2), 446–458.

Parodi, K., Enghardt, W. & Haberer, T., 2002. In-beam PET measurements of b+ radioactivity. *Physics in Medicine and Biology*, 47, 21–36.

Peters, A. et al., 2008. Spill Structure Measurements at the Heidelberg Ion Therapy Centre. *European Particle Accelerator Conference*, TUPP127.

Pijls-Johannesma, M., Pommier, P. & Lievens, Y., 2008. Cost-effectiveness of particle therapy: Current evidence and future needs. *Radiotherapy and oncology*, 89(2), 127–134.

Polf, J.C., Peterson, S., Ciangaru, G. et al., 2009. Prompt gamma-ray emission from biological tissues during proton irradiation: a preliminary study. *Physics in medicine and biology*, 54, 731.

Polf, J.C., Peterson, S., McCleskey, M. et al., 2009. Measurement and calculation of prompt gamma spectra emitted during proton irradiation. *Physics in Medicine and Biology*, 54, N519–N527.

Pshenichnov, I. et al., 2010. Nuclear fragmentation reactions in extended media studied with Geant4 toolkit. *Nuclear Instruments and Methods in Physics Research Section B: Beam Interactions with Materials and Atoms*.

Pshenichnov, I. et al., 2007. PET monitoring of cancer therapy with 3He and 12C beams: a study with the GEANT4 toolkit. *Physics in Medicine and Biology*, 52, 7295.

Rebisz, M. et al., 2006. Synthetic diamonds for heavy-ion therapy dosimetry. *Diamond and Related Materials*, 15(4-8), 822–826.

Richard, M. et al., 2010. Design guidelines for a double scattering Compton camera for prompt-gamma imaging during ion beam therapy: a Monte Carlo simulation study. *Accepted for publication in IEEE TNS*.

Richard, M., 2009. Design of a Compton camera for 3D prompt-gamma imaging during ion beam therapy. *M.S. Thesis CNDRI INSA Lyon*.

Riess, S., 1989. Exclusive photon yields from peripheral collisions of 40Ar+ 158Gd at 44 MeV/u. *Nuclear Physics, Section A*, 495(1-2), 49–55.

Rietzel, E. & Bert, C., 2010. Respiratory motion management in particle therapy. *Medical Physics*, 37, 449.

Rivaton, A. & Arnold, J., 2008. Structural modifications of polymers under the impact of fast neutrons. *Polymer Degradation and Stability*, 93(10), 1864–1868.

Rosenschöld, P.M. et al., 2001. Toward clinical application of prompt gamma spectroscopy for in vivo monitoring of boron uptake in boron neutron capture therapy. *Medical Physics*, 28, 787.

Saha, G.B., 2006. *Physics and radiobiology of nuclear medicine*, Springer Verlag.

Schall, I. et al., 1996. Charge-changing nuclear reactions of relativistic light-ion beams (5 less-than-or-equals, slant Z less-than-or-equals, slant 10) passing through thick absorbers. *Nucl. Instr. and Meth. B*, 117, 221.

Schardt, D., Elsässer, T. & Schulz-Ertner, D., 2010. Heavy-ion tumor therapy: Physical and radiobiological benefits. *Reviews of Modern Physics*, 82, 383–425.

Schardt, D. et al., 1996. Nuclear fragmentation of high-energy heavy-ion beams in water. *Advances in Space Research*, 17(2), 87–94.

Schardt, D. et al., 2007. Precision bragg-curve measurements for light-ion beams in water. *GSI Scientific Report*.

Schneider, U. et al., 2002. Secondary neutron dose during proton therapy using spot scanning. *International Journal of Radiation Oncology* Biology* Physics*, 53(1), 244–251.

Scholz, M. & Elsässer, T., 2007. Biophysical models in ion beam radiotherapy. *Advances in Space Research*, 40(9), 1381–1391.

Scholz, M. & Kraft, G., 1994. Calculation of heavy ion inactivation probabilities based on track structure, x ray sensitivity and target size. *Radiation Protection Dosimetry*, 52(1), 29–38.

Schulz-Ertner, D. & Tsujii, H., 2007. Particle radiation therapy using proton and heavier ion beams. *Journal of Clinical Oncology*, 25(8), 953.

Sihver, L. et al., 2008. Dose calculations at high altitudes and in deep space with GEANT4 using BIC and JQMD models for nucleus–nucleus reactions. *New Journal of Physics*, 10, 105019.

Sisterson, J., 2005. Ion beam therapy in 2004. *Nuclear Inst. and Methods in Physics Research, B*, 241(1-4), 713–716.

Solevi P., 2007. Stydy of in beam PET system for CNAO, the National Centre for Oncological Hadrontherapy. *PhD Thesis Università degli Studi di Milano Italy*.

Styczynski, J. et al., 2009. Can Prompt Gamma Emission During Proton Therapy Provide in Situ Range Verification? *Medical Physics*, 36, 2425.

Testa, E. et al., 2008. Monitoring the Bragg peak location of 73 MeV/ u carbon ions by means of prompt gamma-ray measurements. *Applied Physics Letters*, 93, 093506.

Testa, E. et al., 2009. Dose profile monitoring with carbon ions by means of prompt-gamma measurements. *Nuclear Instruments and Methods in Physics Research Section B: Beam Interactions with Materials and Atoms*, 267(6), 993–996.

Testa, M. et al., 2010. Real-time monitoring of the Bragg-peak position in ion therapy by means of single photon detection. *Radiation and Environmental Biophysics*, 49, 337–343.

Tobias, C.A. et al., 1958. Pituitary Irradiation with High-Energy Proton Beams A Preliminary Report. *Cancer Research*, 18(2), 121.

Tsuji, H. et al., 2005. Hypofractionated radiotherapy with carbon ion beams for prostate cancer. *International Journal of Radiation Oncology Biology Physics*, 63(4), 1153–1160.

Tsujii, H. et al., 2007. Clinical results of carbon ion radiotherapy at NIRS. *Journal of radiation research*, 48(Suppl. A), 1–13.

Valentine, T.E., 2001. Evaluation of prompt fission gamma rays for use in simulating nuclear safeguard measurements. *Annals of Nuclear Energy*, 28(3), 191–201.

Van Eijk, C.W., 2001. Inorganic-scintillator development. *Nuclear Inst. and Methods in Physics Research, A*, 460(1), 1–14.

Walenta, A.H. et al., 2005. Vertex detection in a stack of Si-drift detectors for high resolution gamma-ray imaging. *IEEE Transactions on Nuclear Science*, 52(5

Part 1), 1434–1438.

Wang, C. et al., 2008. Arc-modulated radiation therapy. *Physics in medicine and biology*, 53, 6291–6303.

Waters, L.S. et al., 2007. The MCNPX Monte Carlo radiation transport code. Dans *AIP Conference Proceedings*. p. 81.

Webb, S., 2003. The physical basis of IMRT and inverse planning. *British Journal of Radiology*, 76(910), 678.

Weber, U. & Kraft, G., 1999. Design and construction of a ripple filter for a smoothed depth dose distribution in conformal particle therapy. *Physics in Medicine and Biology*, 44, 2765–2775.

Weyrather, W.K. & Kraft, G., 2004. RBE of carbon ions: experimental data and the strategy of RBE calculation for treatment planning. *Radiotherapy and Oncology*, 73, 161–169.

Wilson, R.R. & others, 1946. Radiological use of fast protons. *Radiology*, 47(5), 487–491.

Winyard, R.A., Lutkin, J.E. & McBeth, G.W., 1971. Pulse shape discrimination in inorganic and organic scintillators. *Nuclear Instruments and Methods*, 95(1), 141–153.

Wisshak, K. & Käppeler, F., 1984. Large barium fluoride detectors. *Nuclear Instruments and Methods in Physics Research Section A: Accelerators, Spectrometers, Detectors and Associated Equipment*, 227(1), 91–96.

Wolski, D. et al., 1995. Comparison of n-gamma discrimination by zero-crossing and digital charge comparison methods. *Nuclear Instruments and Methods in Physics Research A*, 360, 584–592.

Ziegler, J.F., 2004. SRIM-2003. *Nuclear Instruments and Methods in Physics Research Section B: Beam Interactions with Materials and Atoms*, 219, 1027–1036.